Experimental study on rheology of deep mantle minerals

Fang Xu

The graduate school of natural science and technology

Okayama University

February, 2017

Contents

Abstract

Although the majority of deep mantle, i.e. from deep upper mantle (~200 km) to the deep lower mantle (~2700 km), was considered to be seismically isotropic, strong seismic anisotropy was observed in the mantle transition zone and D″ layer. Furthermore, various scales of heterogeneities were detected by seismology in the lower mantle, from tens of km (seismic scatters and reflectors) to hundreds of km (large velocity anomalies). Subducted slab which is comprised of former oceanic crust, underlying harzburgite and depleted peridotite layers is the most dominant source of chemical heterogeneities in the mantle. Global seismic tomography suggested the stagnation of subducted slabs at lower mantle transition zone, D″ layer and top of lower mantle. The subducted oceanic crust, including sediment and mid-ocean ridge basalt (MORB) layers, is SiO_2-rich compared with the surrounding peridotite and/or pyrolite and hence they could cause seismic anisotropy and anomaly in the deep mantle. Therefore, understanding the rheology of SiO_2 phase, predominant phase in SiO_2-rich rock, at high pressure and high temperature provides us important information on mantle dynamics. Furthermore, the mechanism of slab stagnation at mid-mantle depth is still unclear to us. Viscosity of the dominant phases of lower mantle, bridgmanite and ferropericlase, plays an important role in slab stagnation. In this study, we investigated the viscosity and lattice preferred orientation (LPO) of SiO_2 phase and ferropericlase and bridgmanite two-phase aggregate by high pressure and high temperature experimental methods.

Some of the subducted SiO_2-rich components were thought to be deformed and stagnated in the mantle transition zone indicated by seismic tomography. The lower mantle

transition zone, therefore, was proposed to be the fate of subducted SiO_2 phase with forming SiO_2-rich layer at bottom of mantle transition zone. Another possibility for accumulation of SiO_2-rich component is indicated by the observation of seismic anomalies at the bottom of lower mantle, suggesting that the stagnation of subducted slab in the D″ layer. Seismic anisotropies were reported in both the mantle transition zone and D″ layer, which would be caused by the LPO of constituting minerals if they are elastically anisotropic. With understanding the mechanism by which LPO is formed, we can infer the flow pattern of SiO_2-rich components and subducted slab. SiO_2 will be stable as rutile structure (stishovite) and α-PbO_2 structure (seifertite) in the mantle transition zone and D″ layer, respectively, both showing significant anisotropy in elasticity. We conducted deformation experiments on pre-sintered stishovite and α-PbO_2 as an analogue of seifertite using deformation-DIA apparatus at high pressure and high temperature. As a result, the most dominant slip system in stishovite and α-PbO_2 was suggested to be [001] {110} and [100] (010), respectively. The present results suggest that the polarization anisotropy with faster vertically polarized S-wave observed in the lower mantle transition zone can be explained by vertical mantle flow with LPO of stishovite. This may indicate the penetration of subducted SiO_2-rich components into the lower mantle. On the other hand, our result of LPO of α-PbO_2 suggests the considered horizontal flow in the D″ layer will result in a faster vertically polarized S-wave under circum Pacific region, which is inconsistent the seismic observation of faster horizontally polarized S-wave. This indicates an absence of large accumulation of seifertite in the D″ layer, the subducted SiO_2-rich components may be trapped in the lower mantle which were observed as seismic reflectors and scatters.

In the mid-mantle, seismologically observed reflectors were considered to be the preserved subducted SiO_2-rich fragments which penetrated through the mantle transition zone. However, it is still a mystery up to date how the platy shaped seismic reflectors be preserved for a geologic time scale without mixing up with surroundings in the vigorous convecting mantle. High viscosity may play an important role in preservation of seismic reflectors from convective stirring. Because the viscosity is closely related to diffusivity, Si and O self-diffusion in stishovite, which is one of dominant phase of SiO_2-rich fragments, was studied simultaneously up to 21.5 GPa and 2073 K by means of the isotopic tracer method adopting single crystals. Self-diffusion coefficients of Si (D_{Si}) and O (D_O) were determined as D_{Si} [m^2/s]=2.4 $\times 10^{-12}$ exp{-(237 [kJ/mol]+6.0 [cm^3/mol]$\times P$)/RT} and D_O [m^2/s]=7.2 $\times 10^{-11}$ exp{-(263 [kJ/mol]+4.8 [cm^3/mol]$\times P$)/RT}, respectively, where P is pressure (in GPa), T is absolute temperature (in K) and R is the ideal gas constant. Present experiments demonstrated that Si diffusion in stishovite is distinctly slower than those in other mantle minerals. Assuming the inverse relationship between viscosity and diffusivity of Si, it is likely that stishovite is ~4 orders of magnitude harder than bridgmanite at 1000 km depth. Therefore, we anticipated that the high viscosity of SiO_2-rich components is the key to prevent the seismic reflectors from mixing up with the bridgmanite-dominated surrounding mantle.

Seismic tomography imaged slab stagnation and seismic reflectors at mid-mantle depth. The depth of slab stagnation in the lower mantle is coincident with the observed viscosity change inferred from geophysical observation. Subducted slab may temporarily or permanently stagnate in mid-mantle once encounter viscous barrier during subduction.

However, there is no unique mechanism to be responsible for the viscosity change due to the lack of experimental data on rheology of main phases of the lower mantle, bridgmanite and ferropericlase, because of experimental difficulty. Compared with the proposed perovskitic lower mantle, subducted harzburgite layer consists of ~20 vol.% ferropericlase, which is significantly softer than bridgmanite. Chemical difference between the subducted harzburgite layer and underlying perovskitic lower mantle may cause the viscosity jump once ferropericlase dominated the bulk viscosity of harzburgite. To identify the viscosity contrast between the subducting slab and perovskitic lower mantle, deformation experiments on ferropericlase and bridgmanite aggregate were designed. For the deformation experiment under lower mantle conditions, we developed Kawai-type cell assembly (6–8 type) because of sufficient pressure generation. In-situ deformation experiments were conducted using deformation-DIA apparatus. After more than 20 trials with modification, we obtained little strain less than 0.03 at maximum. Alternatively, the newly developed DT-Cup apparatus was used because of the advantage of inducing strain with sample column aligned with the moving direction of differential anvils. We succeed to extend pressure range up to 25 GPa at 1500 ℃ from 19 GPa at room temperature. The experimental setup was applied to uniaxial deformation of post-spinel and bridgmanite two-layer sample up to strain of ~0.2. The virtually identical strain of post-spinel and bridgmanite was observed, suggesting comparable viscosity of post-spinel to bridgmanite and that bridgmanite controls the bulk viscosity of post-spinel. This indicates harzburgite unable to be responsible for the viscosity jump in the lower mantle, or because the strain is not large enough to induce the interconnectivity of ferropericlase. Present development demonstrates an approach of using DT-Cup to study the

rheology of lower mantle minerals. More detailed study on post-spinel and bridgmanite deformation is planned.

Chapter 1. General introduction and background

Heterogeneity and anisotropy in the deep mantle

In a one-dimentional Earth model such as PREM (the preliminary Reference Earth Model) (Dziewonski and Anderson, 1981), a vertical transverse isotropic Earth was assumed. However, mantle is under severe convection, which indicates chemical or temperature deviations from the homogeneous model. The lateral variation can be detected by seismic probing as seismic heterogeneities. During the mantle flow, elastically anisotropic minerals tend to align in certain directions. Seismic velocity observation on this region will turn out to be direction dependent which referred to as seismic anisotropies.

Seismic tomography is the most commonly used technique to infer velocity heterogeneity in the deep mantle. Over the last three decades of work, seismic tomography has produced long-wavelength features and also many detailed structures (e.g. Masters et al., 2000; Romanowicz, 2003; Trampert and Van der Hilst, 2005). The most prominent features of tomographic images in the transition zone is the presence of high-velocity anomalies in the broad regions associated with the subducted slabs (e.g. Fukao et al., 2009, 2013; Romanowicz, 2003; Zhao, 2004). However, corresponding to the subduction region, high-velocity region was also observed in the bottom of the lower mantle, which may suggest that the stagnated slabs ultimately sink to the bottom of the mantle (e.g. Grand, 1994; van der Hilst et al., 1997). In addition, stagnation and broadening of subducting slab in the shallow lower mantle was also observed under South America and Indonesia (Fukao et al., 2013; Li et al., 2008). Two large low shear wave velocity provinces (LLSVP) corresponding to the location of surface hotspots were found at the bottom of lower mantle, one beneath the south Pacific and another beneath Africa (e.g. Garnero, 2000; McNutt, 1998). It is considered that

LLSVP is the origin of upwelling plumes. In addition to the large scaled heterogeneities, a number of seismic reflectors have been discovered beneath the circum-Pacific region in the mid-mantle from 800 to 1800 km depths (e.g. Kaneshima and Helffrich, 1999, 2003; Castle and Creager, 1999; Niu et al., 2003) (recently reviewed by Kaneshima, 2016).

Very little is known about the nature of seismic anisotropy in the deep mantle before as the limitation of seismology. As the improvement of resolution using overtones of surface waves or free oscillations, both polarization anisotropy and azimuthal anisotropy in the mantle transition zone was observed (Montagner and Kennett, 1966; Panning and Romanowicz, 2006; Visser et al., 2008). The S-wave tomography of the whole mantle showed the high association of seismic anisotropy with subducted slabs (Panning and Romanowicz, 2006). The majority of the lower mantle is devoid of anisotropy (Mead et al., 1995) except significant anisotropy observed in the lower most mantle (D″ layer) (e.g. Vinnik et al., 1995; Garnero et al., 2004). The presence of seismic anisotropy in mantle transition zone and D″ layer is because they are boundary layers. Collision of subducted slabs may lead to deformation with higher stress and strain (McNamara et al., 2002). However, Panning and Romanowicz (2004) reported highly variable anisotropy in the D″ layer below the circum Pacific region and central Pacific region.

The heterogeneity in seismic wave velocities should due to the variation of the physical environment (mainly temperature) and/or chemical composition. As the most important dynamic process which recycles oceanic crust into the Earth, slab subduction brings both thermal and compositional anomalies into the mantle. Therefore, subducted slabs are the most potential source of observed heterogeneities. By considering the effect of temperature

and composition, origin of the seismic heterogeneity can be understood. Vice versa, origin of the anomalies is critical for us to better understanding of the evolution of the Earth.

Seismic anisotropy can be caused by layered structure of elastically distinct materials (shape preferred orientation, SPO), or lattice preferred orientation (LPO) of elastically anisotropic minerals. In both cases, the nature of anisotropy is highly dependent on the geometry of deformation, combining with the property of minerals. Therefore, we can infer the deformation geometry in the Earth from the deformation mechanism of constituting minerals and observed seismic anisotropy. In the recent years, important progress has been made by experimental studies (e.g. Jung and Karato, 2001; Ohuchi et al., 2015; Tsujino et al., 2016) and numerical modeling (e.g. Wenk and Van Houtte, 2004; Mainprice et al., 2008) on the variation of LPO under mantle conditions.

Theoretical background of plastic deformation

At the high pressure and high temperature in the Earth's mantle, deformation of minerals are dominated by plastic deformation including dislocation creep and diffusion creep. The plastic properties of a mineral are expressed in terms of relationship between stress (σ) and strain (ε) or strain rate ($\dot{\varepsilon}$) known as "flow low":

$$\dot{\varepsilon} = \frac{\mathrm{d}\varepsilon}{\mathrm{d}t} = A\frac{\sigma^n}{d^m}\exp(-\frac{H}{RT}) \qquad (1.1)$$

where t is time, A is a constant dependent on the material and the particular creep mechanism, d is the grain size, n and m are the stress and grain size exponents dependent on the creep mechanism, H is the activation energy, R is the ideal gas constant, and T is the absolute temperature.

Dislocation creep is plastic deformation occurred by a collective motion of line defects

as crystal dislocations with n=~3-6 and m=0 in Eq. 1.1. The rate of deformation is controlled by dislocation density and the velocity of dislocation motion. Deformation occurs by motions of dislocations including dislocation glide on a given glide plane and dislocation climb out of its glide plane. Theoretical model proposed by Weertman (1968) was widely used in which plastic strain is produced mostly by dislocation glide whereas the rate-controlling process is dislocation climb (e.g. Kohlstedt, 2006). The slowest diffusing species in minerals controls the rate of plastic deformation involving the climb-controlled dislocation creep (e.g., Kirby and Raleigh, 1973), so the creep rate is described as Weertman model (Weertman, 1968):

$$\dot{\varepsilon} = 2\pi \frac{\mu\Omega}{RT} \left(\frac{\sigma}{\mu}\right)^3 \frac{D}{b^2} \frac{1}{\ln(\mu/\sigma)} \frac{l_g}{l_c} \qquad (1.2)$$

where μ is the shear modulus, σ is the stress, D is the diffusion coefficient, Ω is the molar volume, and b is the burgers vector, l_g is the glide distance, and l_c is the climb distance. The ratio of lg/lc is one of the important parameters to describe the dislocation creep in the Weertman model.

In dislocation creep region, non-random distribution of crystallographic orientation of grains, LPO, develops during deformation. LPO of elastically anisotropic minerals leads to the seismic anisotropy by seismological observations. Based on the distribution of anisotropic microstructures in the Earth, dislocation creep was demonstrated dominates in certain regions in the mantle under relatively high stress and/or large grain size conditions as in the boundary layers (Karato, 1998; Karato and Wu, 1993). On the other hand, with experimental understanding the mechanism of forming LPO, we can infer the dynamic process in Earth based on geophysical observations of anisotropic properties.

In diffusion creep region, deformation occurs by transportation of individual atoms due

to thermally activated process. Different from dislocation creep, plastic deformation in diffusion creep is inversely proportional to grain size and weakly dependent on applied stress with n=1 and m=~2-3 in Eq. 1.1. The rate of deformation due to diffusive mass transport is sensitive to diffusion coefficient. Strain rate is described as follows (Nabarro, 1948; Herring, 1950; Coble, 1963; Frost and Ashby, 1982):

$$\dot{\varepsilon} = A\sigma \frac{D^{eff}}{d^2} \frac{\Omega}{RT} \qquad (1.3)$$

Where D^{eff} is the effective diffusion coefficient. Diffusion creep is considered to play an important role when stress is low with small grain size. Different from dislocation creep, diffusional mass transport does not have a rotational component, and no LPO will develop consequently in the diffusion creep region. Diffusion creep will be dominant in the large parts of mantle (e.g. Elliott, 1973; Karato and Li, 1992). One important evidence for inference of diffusion creep in the mantle is the absence of strong LPO despite large strain (Karato et al., 1995).

Experimental approach to mantle rheology

Experimental determination of the rheological properties is important for understanding the deformation process of the Earth's interior. There are mainly two experimental approaches to obtain the rheological properties: one is deformation experiments and the other is diffusion experiments. Because plastic deformation occurs via a thermally activated motion of defects, it is very sensitive to temperature, pressure and chemical environment (such as water fugacity, oxgen fugacity) and grain size (Karato, 2008a). For example, LPO in olivine was revealed to vary in pressure, temperature, and water content (e.g. Raterron et al. 2007; Katayama and Karato, 2006; Jung and Karato, 2001). Therefore laboratory

experiments corresponding to the real mantle conditions are critical to application to the Earth. Rheological properties that we need to know for geodynamical applications include the relationship between the creep strength (flow law), microstructures and physical and chemical conditions.

By deformation experiments, the flow law (Eq. 1.1) can be obtained with measuring the strain rate and stress (Karato, 2008a). Microstructures including grain size, grain shape and LPO provide us remarkable information. But for deformation experiments, extending the pressure range of deformation apparatus and precisely determination of the deviatoric stress are the biggest challenging to assess the whole mantle rheology. Appropriate high-pressure deformation apparatus must meet several conditions: 1) high strength of differential rams to support the high differential stress; 2) stress and strain need to be applied with a controlled fashion so that we can determine the steady-state rheological properties; 3) uniform and stable thermal chemical conditions such as temperature, pressure, water fugacity etc.; 4) large sample value allows evaluation of effects of grain size on flow properties (e.g. Karato, 2008b; Wang et al., 2010).

Many pioneering works have been done with Griggs apparatus (Heard et al., 1972) which was modified after piston-cylinder type high pressure apparatus. But the applicability of this apparatus is limited because the stress was measured outside the pressure vessel with large uncertainties. Later, a gas-medium high pressure deformation apparatus was designed by Paterson (Paterson, 1990) with high resolution in stress measurement (e.g. Mei and Kohlstedt, 2000). Because of the gas pressure medium, the confining pressure was limited to ~0.5 GPa. Diamond anvil cell (DAC) was used attempts at extending the pressure range for

deformation experiments (Kinsland and Bassett, 1977; Sung et al., 1977). This approach has recently been expanded to higher pressures exceeds 200 GPa and widely used for deformation of deep mantle minerals (e.g. Mao et al., 1998; Wenk et al., 2004). However, most of the DAC experiments were conducted at low temperatures and high stresses where deformation mechanisms are likely different from those operating in Earth. The better approach is to use large-volume high pressure apparatus. Recently, three types of deformation apparatus have been designed, i.e. rotational Drickmer apparatus (RDA) (Yamazaki and Karato, 2001), deformation-DIA (Wang et al., 2003) and recently developed DT-Cup apparatus (Hunt et al., 2014). The available pressure and temperature conditions of RDA and DT-Cup reached lower mantle depth recently (Girard et al., 2016; Chapter 4, current thesis). These apparatus were utilized combining with synchrotron, with which stress and strain can be obtained to build up the flow law (Li et al., 2004; Chen et al., 2006).

The other independent method to study the rheology of mantle minerals is diffusion experiments. In diffusion creep and climb controlled dislocation creep region, deformation rate is controlled by atomic diffusion of the slowest diffusion species (Eq. 1.2-4) (e.g. Jaoul et al., 1981). If the diffusion coefficient of the slowest diffusion species are determined, the creep rates of diffusion creep and climb controlled dislocation creep can be estimated. The experimental measurement of diffusion coefficients can be performed using isotopic tracer method over a wide pressure and temperature range. High differential stress in the deformation experiment can be avoid as the hydrostatic pressure condition in diffusion experiments. Up to date, diffusion coefficients of constituting elements in dominant mantle minerals have been determined (e.g. Dohmen et al., 2002; Shimojuku et al., 2009; Xu et al.,

2011; Fei et al., 2013).

In this study, we conducted deformation experiments on stishovite in the dislocation creep regime to observe LPO by means of high pressure experiments. The results can be applied to the interpretation of seismic observation as described in "*Heterogeneity and anisotropy in the deep mantle*" section to understand the flow pattern in the mantle transition zone. We also conducted deformation experiments on the analogue of seifertite, α-PbO_2, to clarify the contribution of SiO_2 phase to the observed seismic anisotropy in the D″ layer (Chapter 2). For the estimation of the viscosity of seismic reflector, we determined the diffusivities of constituting species of stishovite because diffusivity controls viscosity in both of diffusion creep and climb dominated dislocation creep as mentioned in "*Theoretical background of plastic deformation*" section. Based on the estimation of viscosity, we discussed the preservation of seismic reflector which may be dominant with SiO_2 component (Chapter 3). Finally, we technically developed deformation experiment at high pressure more than 25 GPa to study the rheology of lower mantle minerals. After developing we apply this technique to deform post-spinel and bridgmanite two-layer sample to understand the mechanism of slab stagnation at mid-mantle depths (Chapter 4).

Reference

Chen, J., Li, L., Yu, T., Long, H., Weidner, D., Wang, L. and Vaughan, M., 2006. Do Reuss and Voigt bounds really bound in high-pressure rheology experiments? J. Phys., 18, pp. S1049- S1059.

Coble, R.L., 1963. A model for boundary diffusion controlled creep in polycrystalline materials. J. App. Phys., 34, pp. 1679-1682.

Dziewonski, A.M. and Anderson, D.L., 1981. Preliminary reference Earth model. Phys. Earth Planet. Int., 25, pp. 297-356.

Elliott, D., 1973. Diffusion flow laws in metamorphic rocks. Geol. Soci. Amer. Bulletin, 84, pp. 2645-2664.

Fei, H., Wiedenbeck, M., Yamazaki, D. and Katsura, T., 2013. Small effect of water on upper-mantle rheology based on silicon self-diffusion coefficients. Nature, 498, pp. 213-215.

Frost, H. J., Ashby, M. F., 1982. Deformation mechanism maps: the plasticity and creep of metals and ceramics. Pergamon Press, Oxford, UK.

Fukao, Y., Obayashi, M. and Nakakuki, T., 2009. Stagnant slab: a review. Annual Rev. Earth Planet. Sci., 37, pp.19-46.

Fukao, Y. and Obayashi, M., 2013. Subducted slabs stagnant above, penetrating through, and trapped below the 660 km discontinuity. J. Geophy. Res., 118, pp. 5920-5938.

Garnero, E.J. and Jeanloz, R., 2000. Fuzzy patches on the Earth's core-mantle boundary?. Geophy. Res. Lett., 27, pp. 2777-2780.

Garnero, E.J., 2004. A new paradigm for Earth's core-mantle boundary. Science, 304, pp.834-836.

Girard, J., Amulele, G., Farla, R., Mohiuddin, A. and Karato, S.I., 2016. Shear deformation of bridgmanite and magnesiowüstite aggregates at lower mantle conditions. Science, 351, pp. 144-147.

Grand, S.P., 1994. Mantle shear structure beneath the Americas and surrounding oceans. J. Geophy. Res., 99, pp.11591-11621.

Heard, H.C., 1972. Flow and fracture of rocks (Vol. 16). AGU, Washingto DC, pp. 352.

Herring, C., 1950. Diffusional viscosity of a polycrystalline solid. J. App. Phys., 21, pp. 437-445.

Hunt, S.A., Weidner, D.J., McCormack, R.J., Whitaker, M.L., Bailey, E., Li, L., Vaughan, M.T., Dobson, D.P., 2014. Deformation T-Cup: A new multi-anvil apparatus for controlled strain-rate deformation experiments at pressures above 18 GPa. Rev. Sci. Inst., 85, pp. 085-103.

Jaoul, O., Poumellec, M., Froidevaux, C., Havette, A., 1981. Silicon diffusion in forsterite: a new constraint for understanding mantle deformation. Anelasticity in the Earth, pp.95-100.

Jung, H. and Karato, S.I., 2001. Water-induced fabric transitions in olivine. Science, 293, pp. 1460-1463.

Kaneshima. S, 2016. Seismic scatterers in the mid-lower mantle. Phys. Earth Planet. Inter., 257, pp. 105–114.

Kaneshima, S., Helffrich, G., 1999. Dipping low-velocity layer in the mid-lower mantle: evidence for geochemical heterogeneity. Science, 283, 1888-1892.

Kaneshima, S., Helffrich, G., 2003. Subparallel dipping heterogeneities in the mid‐lower mantle. J. Geophys. Res., 108, 2272.

Karato, S.I., 1998. Some remarks on the origin of seismic anisotropy in the D″ layer. Earth Planets. Space, 50, pp. 1019-1028.

Karato, S.I., 2008a. Deformation of earth materials: an introduction to the rheology of solid

earth. Cambridge University Press.

Karato, S.I., 2008b. Recent progress in the experimental studies on the kinetic properties in minerals. Phys. Earth Planet. Int., 170, pp. 152-155.

Karato, S.I. and Li, P., 1992. Diffusion creep in perovskite: implications for the rheology of the lower mantle. Science, 255, pp. 1238.

Karato, S.I. and Wu, P., 1993. Rheology of the upper mantle: A synthesis. Science, 260, pp. 771-778.

Karato, S.I., Zhang, S. and Wenk, H.R., 1995. Superplasticity in Earth's lower mantle: evidence from seismic anisotropy and rock physics. Science, 270, pp. 458.

Katayama I, Karato S. 2006. Effects of temperature on the B- to C-type fabric transition in olivine. Phys. Earth Planet. Inter. 157, pp. 33-45.

Kinsland, G. L., Bassett, W., 1977. Strength of MgO and NaCl polycrystals to confining pressures of 250K bar at 25°C. J. Appl. Phys., 48, pp. 978-985.

Kirby, S.H., Raleigh, C.B., 1973. Mechanisms of high-temperature, solid-state flow in minerals and ceramics and their bearing on the creep behavior of the mantle. Tectonophysics 19, pp. 165-194.

Kohlstedt, D.L., 2006. The role of water in high-temperature rock deformation. In: Keppler, H., Smyth, J.R. (Eds.), Water in nominally anhydrous minerals. Rev. Min. Geochem. vol. 62, pp. 377-396.

Li, C., van der Hilst, R.D., Engdahl, E.R. and Burdick, S., 2008. A new global model for P wave speed variations in Earth's mantle. Geochem. Geophys. Geosys. 9, Q05018.

Li L, Weidner D, Raterron P, Chen J, and Vaughan M, 2004. Stress measurements of

deforming olivine at high pressure. Phys. Earth Planet. Int., 143-144, pp. 357-367.

Masters, G., Laske, G., Bolton, H. and Dziewonski, A., 2000. The relative behavior of shear velocity, bulk sound speed, and compressional velocity in the mantle: implications for chemical and thermal structure. Earth's deep interior: mineral physics and tomography from the atomic to the global scale, pp.63-87.

McNamara, A.K., Van Keken, P.E., Karato, S.I., 2002. Development of anisotropic structure in the Earth's lower mantle by solid-state convection. Nature, 416, pp. 310-314.

Meade, C., Silver, P.G. and Kaneshima, S., 1995. Laboratory and seismological observations of lower mantle isotropy. Geophy. Res. Lett., 22, pp. 1293-1296.

Mei, S., and Kohlstedt, D. L., 2000. Influence of water on plastic deformation of olivine aggregates: 2. Dislocation creep regime, J. Geophys. Res., 105, pp. 21471-21481.

Montagner J P, Kennett B L N., 1996. How to reconcile body-wave and normal-mode reference Earth models. Geophys. J. Int., 125, pp. 229-248.

Nabarro, F.R.N., 1948. Deformation of crystals by the motion of single ions. In Report of a Conference on Strength of Solids (pp. 75-90).

Niu, F., Kawakatsu, H., Fukao, Y., 2003. Seismic evidence for a chemical heterogeneity in the midmantle: a strong and slightly dipping seismic reflector beneath the Mariana subduction zone. J. Geophys. Res., 108, 2419.

Tsujino, N., Nishihara, Y., Yamazaki, D., Seto, Y., Higo, Y., Takahashi, E., 2016. Mantle dynamics inferred from the crystallographic preferred orientation of bridgmanite. Nature, 539, pp. 81-84.

Ohuchi T, Fujino K, Kawazoe T, et al., 2014. Crystallographic preferred orientation of

wadsleyite and ringwoodite: Effects of phase transformation and water on seismic anisotropy in the mantle transition zone. Earth Planet. Sci. Lett., 397, pp. 133-144.

Panning, M. and Romanowicz, B., 2004. Inferences on flow at the base of Earth's mantle based on seismic anisotropy. Science, 303, pp.351-353.

Panning M, Romanowicz B., 2006. A three-dimensional radially anisotropic model of shear velocity in the whole mantle. Geophys. J. Int., 167, pp. 361-379.

Paterson, M.S., 1990. Rock deformation experimentation. The brittle-ductile transition in rocks, pp. 187-194.

Raterron P, Chen J, Li L,Weidner DJ, Cordier P. 2007. Pressure-induced slip system transition in forsterite: single-crystal rheological properties at mantle pressure and temperature. Am. Mineral. 92, pp. 1436-45

Ringwood, A.E., Hibberson, W., 1991. Solubilities of mantle oxides in molten iron at high pressures and temperatures: implications for the composition and formation of Earth's core. Earth Planet. Sci. Lett., 102, pp.235-251.

Romanowicz, B., 2003. Global mantle tomography: progress status in the past 10 years. Annual Rev. Earth Planet. Sci., 31, pp. 303-328.

Shimojuku, A., Kubo, T., Ohtani, E., Nakamura, T., Okazaki, R., Dohmen, R., Chakraborty, S., 2009. Si and O diffusion in $(Mg, Fe)_2 SiO_4$ wadsleyite and ringwoodite and its implications for the rheology of the mantle transition zone. Earth Planet. Sci. Lett., 284, pp. 103-112.

Shimojuku, A., Kubo, T., Kato, T., Yoshino, T., Nishi, M., Nakamura, T., Okazaki, R. and Kakazu, Y., 2014. Effects of pressure and temperature on the silicon diffusivity of

pyrope-rich garnet. Phys. Earth Planet. Int., 226, pp. 28-38.

Sung, C.M., Goetze, C. and Mao, H.K., 1977. Pressure distribution in the diamond anvil press and the shear strenght of fayalite. Rev. Sci. Instru., 48, pp. 1386-1391.

Mainprice, D., Tommasi, A., Ferré, D., Carrez, P. and Cordier, P., 2008. Predicted glide systems and crystal preferred orientations of polycrystalline silicate Mg-Perovskite at high pressure: Implications for the seismic anisotropy in the lower mantle. Earth Planet. Sci. Lett., 271, pp. 135-144.

Mao, H.K., Shu, J., Shen, G., Hemley, R.J., Li, B. and Singh, A.K., 1998. Elasticity and rheology of iron above 220 GPa and the nature of the Earth's inner core. Nature, 396, pp. 741-743.

McNutt, M.K., 1998. Superswells. Rev. Geophys., 36, pp. 211-244

Trampert, J. and Van Der Hilst, R.D., 2005. Towards a quantitative interpretation of global seismic tomography. Earth's Deep Mantle: Structure, Composition, and Evolution, pp. 47-62.

Van der Hilst, R.D., Widiyantoro, S. and Engdahl, E.R., 1997. Evidence for deep mantle circulation from global tomography. Nature, 386, pp. 578-584.

Vinnik, L., Romanowicz, B., Le Stunff, Y. and Makeyeva, L., 1995. Seismic anisotropy in the D″ layer. Geophy. Res. Lett., 22, pp. 1657-1660.

Visser K, Trampert J, Lebedev S, et al., 2008. Probability of radial anisotropy in the deep mantle. Earth Planet. Sci. Lett., 270, pp. 241-250.

Wang, Y., Durham, W.B., Getting, I.C. and Weidner, D.J., 2003. The deformation-DIA: A new apparatus for high temperature triaxial deformation to pressures up to 15 GPa. Rev.

Sci. Instr., 74, pp. 3002-3011.

Wang, Y., Hilairet, N. and Dera, P., 2010. Recent advances in high pressure and temperature rheological studies. J. Earth Sci., 21, pp. 495-516.

Weertman, J., 1968. Dislocation climb theory of steady-state creep. Transactions of the Am. Soci. Metals, 61, 681-694.

Weertman, J., 1999. Microstructural mechanisms of creep. Mechanics and materials: Fundamentals and linkages, pp. 451-488.

Wenk, H.R. and Van Houtte, P., 2004. Texture and anisotropy. Reports on Progress in Physics, 67, pp. 1367.

Wenk HR, Lonardelli I, Pehl J, et al., 2004. *In situ* observation of texture development in olivine, ringwoodite, magnesiowustite and silicate perovskite at high pressure. Earth Planet. Sci. Lett., 226, pp. 507-519.

Xu, J., Yamazaki, D., Katsura, T., Wu, X., Remmert, P., Yurimoto, H. and Chakraborty, S., 2011. Silicon and magnesium diffusion in a single crystal of $MgSiO_3$ perovskite. J Geophy. Res., 116.

Yamazaki, D. and Karato, S.I., 2001. High-pressure rotational deformation apparatus to 15 GPa. Rev. Sci. Instru., 72, pp. 4207-4211.

Zhao, D., 2004. Global tomographic images of mantle plumes and subducting slabs: insight into deep Earth dynamics. Phys. Earth Planet. Int., 146, pp. 3-34.

Chapter 2. Lattice preferred orientation of high-pressure polymorphs of silica deformed at high pressure and high temperature

Abstract

Although the majority of deep mantle is seismically isotropic, strong seismic anisotropy was observed in the boundary layers, i.e. mantle transition zone and the lowermost mantle (D″ layer), which could be caused by the lattice preferred orientation (LPO) of constituting minerals. Whole mantle S-wave tomography showed the high association of seismic anisotropy with subducted slabs. The subducted sediment, MORB layers and possible entrained primordial continents are SiO_2-rich, which will be stable as rutile (stishovite) and α-PbO_2 structure (seifertite) in the mantle transition zone and D″ layer, respectively. Stishovite and seifertite show significant anisotropic elasticity and they would contribute to the observed seismic anisotropy once SiO_2-rich components accumulated in the layers. With understanding the mechanism by which LPO was formed, we can infer the flow pattern of SiO_2-rich components in mantle. However, the knowledge of LPO of stishovite and seifertite developed at high pressure and high temperature is not enough to understand the observed seismic anisotropy.

In this study, deformation experiments were conducted on pre-sintered stishovite and analogue of seifertite (α-PbO_2) using deformation-DIA apparatus at high pressure and high temperature. LPOs were identified by electron backscatter diffraction measurement and two-dimensional X-ray diffraction. The most dominant slip system in stishovite and seifertite was suggested to be [001] {110} and [100] (010), respectively. The polarization anisotropy with faster vertically polarized S-wave observed in the lower mantle transition zone indicated the vertical flow related with the subducted SiO_2-rich components. It may suggest the stagnation of stishovite layer with horizontal flow in the lower mantle transition zone is not favored. our

result of LPO of α-PbO_2 suggests the horizontal flow in the D″ layer, which was considered as dominant flow in the circum Pacific region, will result in a faster vertically polarized S-wave. This is inconsistent with the seismic observation of faster horizontally polarized S-wave. This indicates an absence of large accumulation of seifertite in the D″ layer, the subducted SiO_2-rich components may be trapped in the lower mantle which were observed as seismic reflectors and scatters.

2.1. Introduction

Although the majority of deep mantle is devoid of anisotropy, strong seismic anisotropy was observed in the boundary layers, i.e. mantle transition zone and the lowermost mantle (D″ layer) (e.g. Panning and Romanowicz, 2004, 2006; Visser et al., 2008). The observed seismic anisotropy could be caused by the LPO of constituting minerals if they are elastically anisotropic, and the LPO can be formed by deformation during the dynamic mantle flow. The presence of seismic anisotropy in the boundary layers partially reflects the strong dynamic process at the layer boundary (McNamara et al., 2002), but the elastic anisotropy of constituent materials also plays a significant role. The S-wave tomography of the whole mantle showed the high association of seismic anisotropy with subducted slabs (Panning and Romanowicz, 2006). The subducted slab transports chemically heterogeneous sediment and basalt (MORB, mid-ocean ridge basalt) layers as far as 660 km depth discontinuity and even deep into the lower mantle based on both seismic observation (e.g. Fukao and Obayashi, 2013) and also mineralogical density estimation (e.g. Hirose et al., 2005; Komobayashi et al., 2009). They could significantly contribute to the observed seismic anisotropy once they are more elastically anisotropic compared with surrounding mantle.

Compared with the pyrolytic surrounding mantle, sediment and MORB layers are enriched in SiO_2, i.e. ~10-20 vol.% in MORB and ~30-40 vol.% in sediment (Irifune and Ringwood, 1993; Irifune et al., 1994). The SiO_2 composition will be stable as rutile-type polymorph as stishovite in the mantle transition zone (Stishov and Popova, 1961), and α-PbO_2 like structure known as seifertite in the D″ layer (Grocholski et al., 2013; El Goresy et al., 2008). Kawai et al. (2009) proposed that the Archean “granite”, tonalite-trondhjemite-

granodiorite (TTG), had been stagnated in the lower transition zone, in which silica dominates more than 75 vol.%. The bottom of the D″ layer could be more enriched in silica due to the chemical reaction with the liquid iron of the outer core (Knittle and Jeanloz, 1991).

By first principle calculation, Karki et al. (1997) obtained the pressure dependence of elasticity of high-pressure polymorphs of silica. Although decrease with pressure, silica under deep mantle condition shows strong elastic anisotropy and may significantly contribute to the observed seismic anisotropy. In particular, acoustic velocity measurement on a single crystal of stishovite revealed S-wave polarization anisotropy as much as ~60 % in the wave propagating along the <110> direction (Yoneda et al., 2012). Therefore, the LPO of stishovite and seifertite accumulate in the lower transition zone and D″ layer has a high potential to contribute to the observed seismic anisotropy. With understanding the mechanism by which LPO is formed, we can infer the flow pattern of SiO_2 components and subducted slab.

Probably the most practical and effective way to investigate the fabric of the stishovite and seifertite is direct observation of microstructure and crystallographic orientation on samples recovered from large strain deformation experiment. There are several attempts to investigate the LPO of stishovite, Cordier et al. (2004) and Texier and Cordier (2006) conducted the stress relaxiation experiments using the Kawai-type multianvil apparatus at 13 GPa and 1300 °C. The transmission electron microscopy observation on dislocations of stishovite indicated the easy slip systems with the [001] direction in the {100} and the {210} planes. On the other hand, various slip directions in the (001) plane are activated at high pressure and room temperature during uniaxial compression in diamond anvil cell (Kaercher et al., 2014). There is no consensus on the dominant slip system of stishovite because of the

lack of well-controlled deformation experiments at high pressure and high temperature. On the other hand, because the seifertite is only stable at pressures higher than 120 GPa and temperatures higher than 2500 K (Grocholski et al., 2013), which make it impossible to study the rheological feature by deformation at high pressure and high temperature. There is no investigation on the fabric on seifertite until now.

In this study, we conducted three types of deformation experiments, uniaxial deformation (compressional and tensional) and shear deformation, of stishovite at high pressure and high temperature to obtain LPO pattern formed by well controlled deformation process. Deformation experiment on α-PbO_2, which is an analogue of seifertite at relatively low pressure, was conducted to study the fabric of α-PbO_2 phase. The slip system and LPO pattern strongly depend on crystal structure, but not on chemistry (Karato, 1989). Therefore, the fabric developed in α-PbO_2 was observed and applied to the D″ layer.

2.2. Experimental procedure

2.2.1. Starting materials

To avoid large deformation during compression, well sintered polycrystalline aggregates of stishovite and α-PbO_2 were pre-synthesized as starting materials for deformation experiments. All synthesis experiments were done at high pressure and high temperature in the Kawai-type multianvil apparatus installed at Institute for Planetary Materials, Okayama University, Japan. MgO+5 %Cr_2O_3 octahedra with a 18 mm or 25 mm edge length and WC cubes with 11 mm or 15 mm truncated edge length were used for synthesis of stishovite and α-PbO_2 aggregates (Fig. 2.1 a and b), respectively.

To synthesis well-sintered stishovite, we compressed the starting material of anhydrous gel powder wrapped with platinum capsule to 12 GPa and annealed at 1450 °C for half an hour. Even small amount of water will promote grain growth largely, so silicagel was baked at 1000 ℃ for ~10 hours to remove the water. The baked silica gel put in capsule were kept at 473 K in a vacuum oven to minimize the water absorption of the powder before the experiment. The sintered stishovite samples were core-drilled with a diameter of 1.1 mm by ultrasonic coring machine and sliced with a thickness of 1.1 mm for uniaixal deformation experiments. For shear deformation experiments, stishovite aggregates were sliced at an angle of 45° respect to the cylindrical axis with 200 μm thickness.

The commercial PbO_2 powder was further ground down to ~1 μm to be the starting material of synthesis experiment for α-PbO_2 aggregates. The PbO_2 powder wrapped with platinum capsule was kept at 473 K in a vacuum oven to minimize the water contamination before the experiment. α-PbO_2 aggregates was synthesized at 5 GPa and 550 °C for 1 hour. The samples were core-drilled with a diameter of 2.0 mm by ultrasonic coring machine and sliced at an angle of 45° respect to the cylindrical axis with a thickness of 250 μm.

2.2.2. Deformation experiment

Deformation experiments were conducted with D-DIA type apparatus (Wang et al., 2003). Two differential rams introduced in the upper and lower guide blocks allow independent control of the differential strain and stress field under high confining pressure. As shown in Fig. 2.2, the 6-8 type deformation cell (Fig. 2.2a) (Kawai-type multianvil cell assembly, Nishihara, 2008; Tsujino et al., 2016), eight second-stage cubic anvils with an

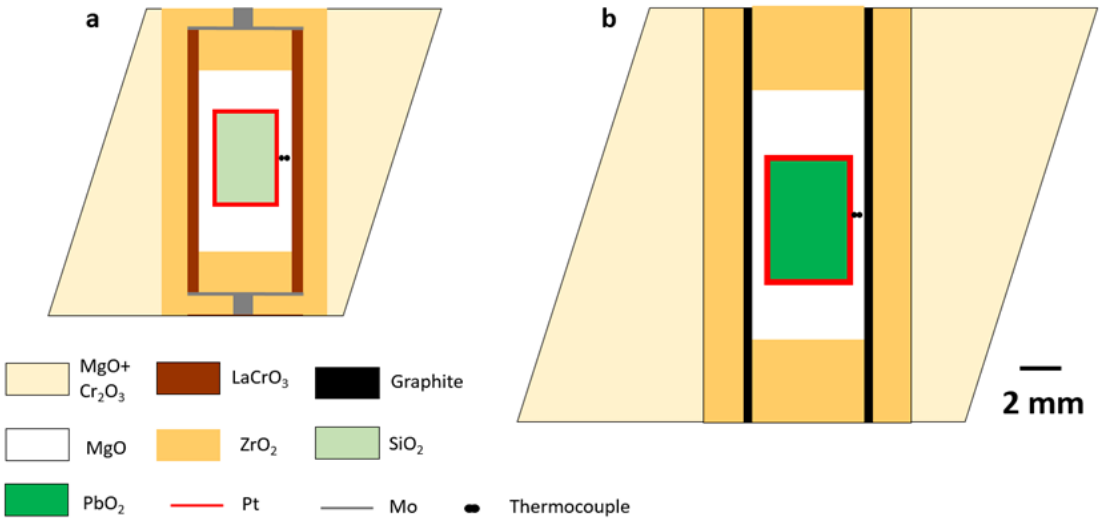

Fig. 2.1. Configuration of cell assemblies for synthesis of stishovite (a) and for α-PbO_2 aggregates (b).

octahedral shape pressure medium, was applied for deformation of stishovite. For deformation of α-PbO_2, 6-6 type cell assembly (Fig. 2.2b) (Nishiyama et al., 2008), six tungsten carbide (WC) anvils with cubic pressure medium, was utilized. As the better hydrostatic condition with more anvils compressing from more directions compared with MA6-6 type cell, the MA6-8 type cell has advantage of generating high pressure.

Deformation of stishovite

We conducted deformation experiments on stishovite at high pressure and high temperature using D-DIA type apparatus (SPEED MK-II) installed at Bl04B1, SPring-8, Japan. We performed deformation experiments in the stability filed of stishovite at 12 GPa and 1600 °C. Pressure medium of semi-sintered 5 wt.% Cr_2O_3-doped MgO octahedra with 10 mm edge length were compressed by tungsten carbide (WC) cubes with 5 mm truncation edge length. The cross-sections of cell assemblies for deformation experiments are shown in

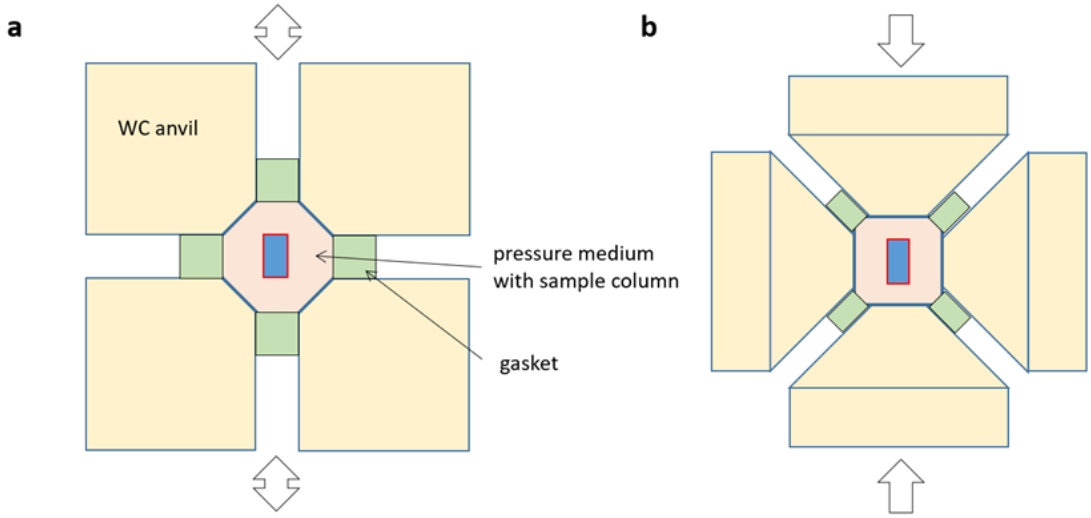

Fig. 2.2. Schematic show of 6-8 (a) and 6-6 (b) type assembly for deformation.

Fig. 2.3. High temperature was generated using a $LaCrO_3$ heater and was monitored with a $W_{97\%}Re_{3\%}$-$W_{75\%}Re_{25\%}$ thermocouple whose junction was set next to the samples. Mo foil was used as electrode between WC anvils and $LaCrO_3$ heater. In the uniaxial deformation experiments, we use sintered-diamond (SD) with Si binder as pistons, and Re foils to prevent the direct contact between sample and SD pistons in order to separate them easily after deformation experiments (Fig. 2.2a). In the shear deformation experiments, we cut the ellipsoid slices of sample to two halves to insert the platinum foil as strain marker (Fig. 2.2b). The samples were sandwiched by two alumina pistons with 45° cut respect to the cylindrical axis. In both cells, porous crushable alumina rods were used to avoid the deformation of sample during compression at room temperature.

We conducted deformation experiments by both advance and retraction of differential rams after compression to the target pressure (12 GPa) and heating to the target temperature (1600 °C). For deformation by advancement of differential rams, which were not activated

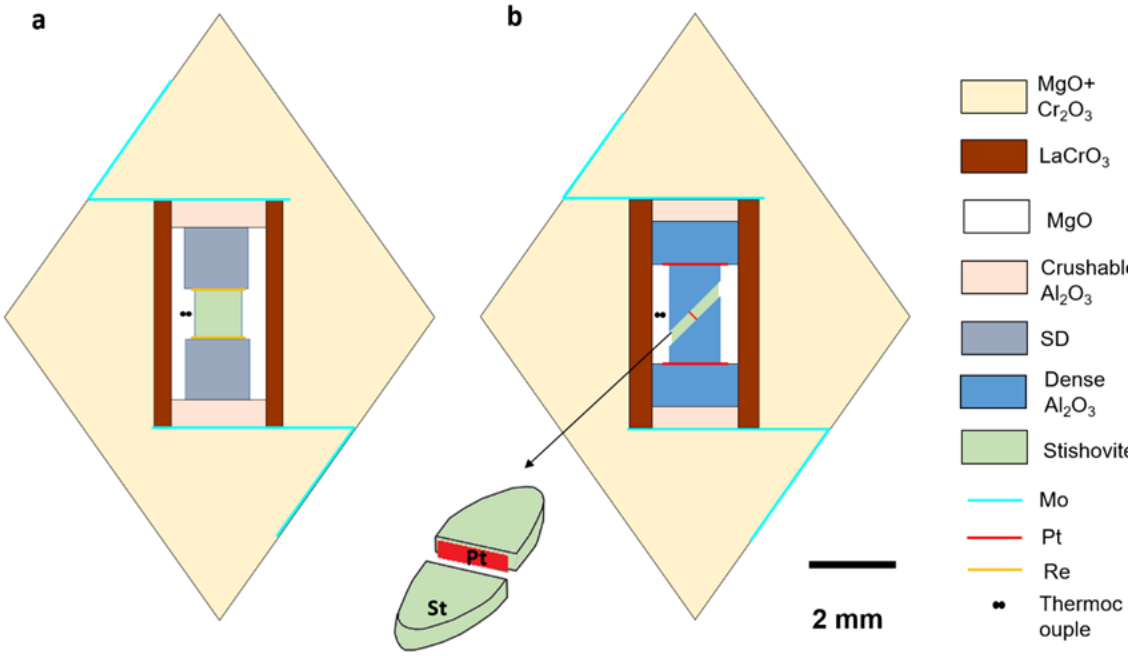

Fig. 2.3. Configuration of cell assemblies for uniaxial deformation experiment (a) and for simple shear deformation experiment (b).

during compression, we lifted the differential rams before deformation by rapidly oil pump to the differential rams until the loads reach one third of the main ram load. Sub-sequentially, the deformation were conducted with a constant advancement rate. As shown in Fig. 2.4a, first, the loads of differential rams rapidly increased up to more than 1.4 MN (main load is 4 MN) with insufficient movement of displacements, it is considered that the displacements of differential rams increased by elastic deformation of differential rams and guide block of apparatus. Plastic deformation is thought to occur during the next stage, in which activated differential ram efficiently moved with slightly increase of loads. For deformation by retraction of differential rams, we advanced the differential rams during compression to keep the cubic space after interference of alignment by increasing of top-bottom ram distance. The

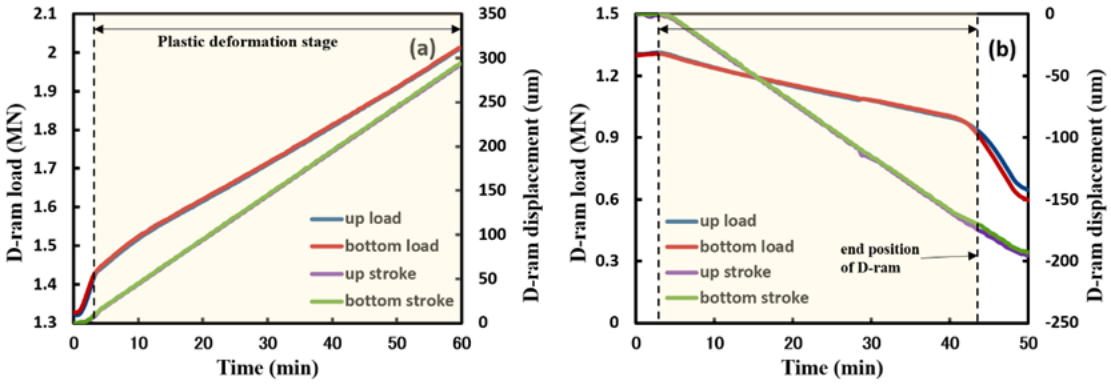

Fig. 2.4. Loads and displacements of upper and lower differential rams during deformation of stishovite by advancement (a) and retraction (b) of D-rams. (a) Each differential ram was advanced with constant speed of 5 μm/min. (b) Each D-ram was retracted for 200 μm with constant speed in 50 mins.

loads of differential rams were around one third of main ram (1.3 MN) load just after compression (Fig. 2.4b). The differential rams were retracted with constant retraction rate in order to deform the sample. The differential ram loads gradually decreased until ~1.0 MN, at which the differential rams reached at the end position. The insufficient movement causes the largely drop of differential rams loads by elastic deformation of differential rams and apparatus, deformation wouldn't occur during this stage. In this study, uniaxial deformation by both retraction and advancement of differential rams were conducted. Shear deformation experiment was conducted by advancement of differential rams.

Deformation of α-PbO_2

We conducted deformation experiment at pressure of 4 GPa and temperature of 727 °C in the stability filed of α-PbO_2 (Yagi&Akimoto, 1980). This temperature corresponds to ~0.7 of melting temperature (T_m) of PbO_2 (Grocholski et al., 2014), which is comparable to the ratio of temperature at the bottom of D″ layer to the T_m of SiO_2 composition (Luo et al., 2002).

Shear deformation experiments on α-PbO_2 aggregates were performed using Kawai-type multianvil apparatus (KATD) installed at Institute for Planetary Materials (Nishihara, 2008; Tsujino et al., 2016). WC anvils with a truncated edge length of 4 mm and a cubic pressure medium of semi-sintered 5 wt.% Cr_2O_3-doped MgO with 8 mm edge length was used for generate high pressure. The cross-section of the cell assembly for deformation experiment was shown in Fig. 2.5. The ellipsoid slice of sample was cut to two halves to insert the platinum foil as strain marker. The samples were sandwiched by two alumina pistons with 45° cut respect to the cylindrical axis. High temperature was generated using a graphite heater and was monitored with a W_{97}%Re_3%-W_{75}%Re_{25}% thermocouple which were connected to each other via the platinum capsule.

Shear deformation experiments on α-PbO_2 were conducted by advance of differential rams after compression and heating. Same with compressional deformation of stishovite, we lifted the differential rams before deformation by rapidly oil pump to the differential rams

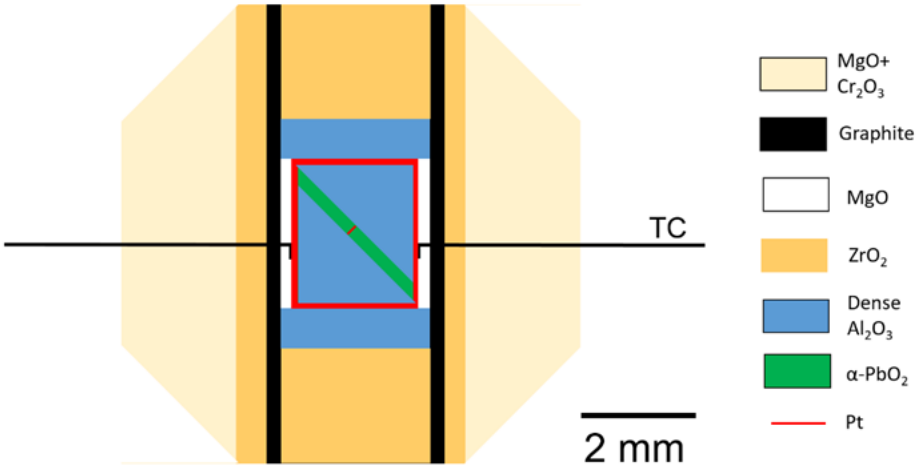

Fig. 2.5. Configuration of cell assemblies for shear deformation experiment of α-PbO_2 with 6-6 type cell assembly.

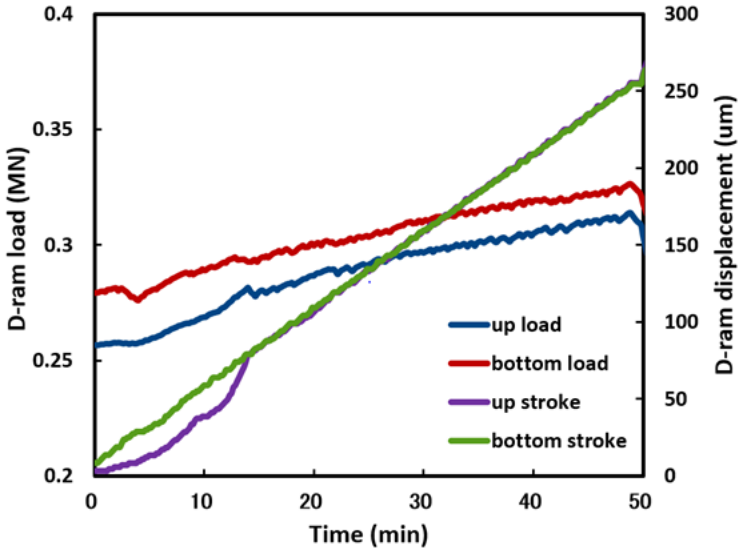

Fig. 2.6. Loads and displacements of upper and lower differential rams during deformation of α-PbO_2 by advancement of D-rams.

until the loads reach about one third of the main ram load (0.23 MN). Sub-sequentially, the deformation were conducted with a constant advancement rate. As shown in Fig. 2.6, during deformation, load of differential rams increase at a constant rate. Although top ram shown some sluggish during deformation, the deformation was conducted with a uniform rate.

After deformation, samples were quenched and sub-sequentially decompressed with controlling the differential ram position to avoid additional deformation during decompression. In the uniaxial deformation experiments, we calculated the strain from the change of sample lengths before and after deformation experiments. In the shear deformation experiments, strain was estimated from the rotation of the strain marker, which was initially located perpendicular to the shear direction. We simply calculated the averaged strain rate with total strain and duration of the deformation under the assumption of constant strain rate during deformation.

2.2.3. Microstructure analysis

After experiments, the recovered uniaxial deformed samples were separated from other parts and then polished parallel or perpendicular to the cylindrical axis after mounted in epoxy resin. Shear deformation cell was directly mounted in epoxy resin and polished parallel to the shear direction and shear plane normal. The samples were polished sequentially using SiC sand papers and diamond paste, and finally colloidal silica suspension to remove the physically damaged surface. We investigated the microstructure of recovered samples by field emission scanning electron microscopy (FE-SEM, JEOL JSM-700F) with electron backscatter diffraction (EBSD) system. The LPO of stishovite and α-PbO_2 was evaluated from the EBSD patterns obtained at 15 kV acceleration voltage and 5.0 nA probe current. The EBSD patterns were indexed with HKL CHANNEL5 software (Oxford instruments, Ltd.). The measurements were performed by the automatic beam scanning with a step of 1-3 μm and indexing of EBSD patterns to cover the large area of polished sample section. α-PbO_2 is too soft to be well polished, we also measured the LPO using the two-dimensional (2D) monochromatic X-ray diffraction pattern method. 2D X-ray diffraction pattern was obtained using the radial diffraction of 63.182 keV (wavelength λ=0.1962 Å) monochromatic X-rays (Seto et al., 2012) at Bl04B1, SPring-8, Japan. The sample was measured with the direction perpendicular to the shear direction and shear normal direction along the direction of the X-ray beam (Fig. 2.7). Optical parameters including camera length, pixel shape of camera, and so on were calibrated using a CeO_2 standard. The two-dimensional (2D) diffraction patterns were collected with a beam size of 200 μm×100 μm for 15 min using an imaging plate (IP). The IP data were acquired using a

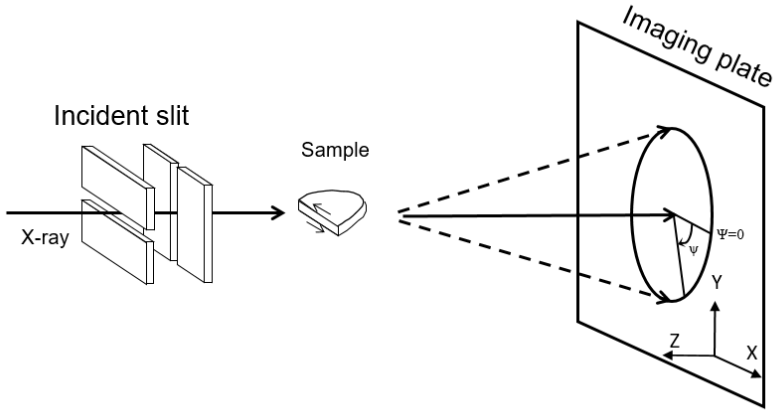

Fig. 2.7. Schematic showing of the two-dimensional X-ray diffraction measurement set-up.

FUJI BAS 2000 reader under a resolution of 100 μm×100 μm. The LPO was calculated using the software package of both ReciPro (Seto et al., 2012) and MAUD (Lutterotti et al., 2007) by simulating the obtained the 2D data.

2.3. Result

2.3.1. Result of deformation experiment on stishovite

The recovered samples after uniaxial deformation experiments by the advancement of the differential rams showed elongation along the cylindrical axis as a tensional geometry (hereafter, we call it “tensional deformation”) with the 6-8 type cell assembly, whereas samples deformed by retraction of differential rams showed shortening along the cylindrical axis as a compressional geometry (hereafter, we call it “compressional deformation”). The inconsistence between the movement of differential rams and resulted deformation geometry

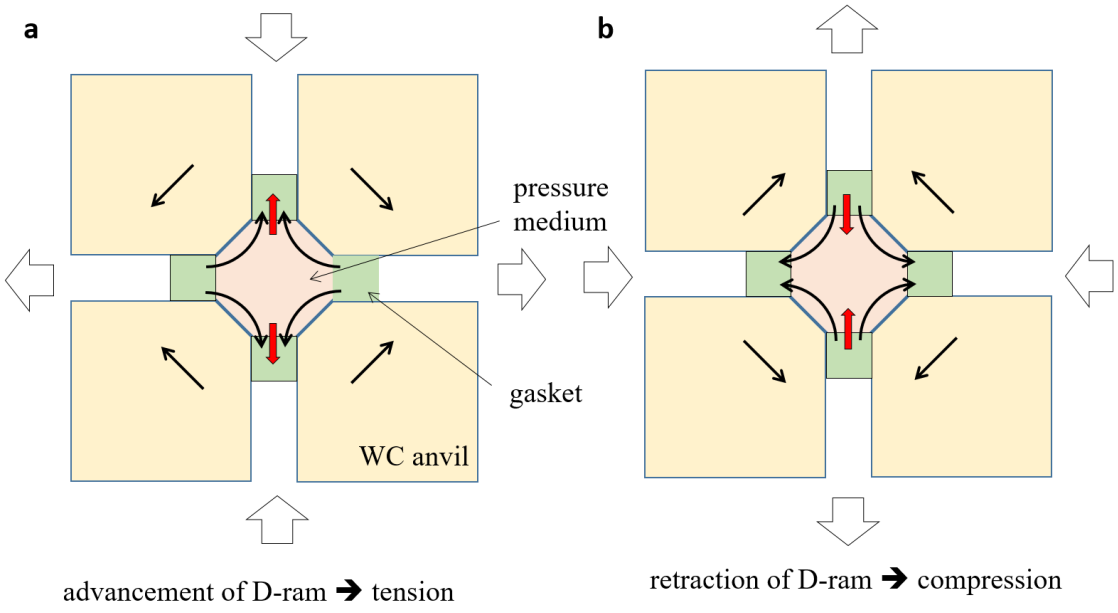

Fig. 2.8. Schematic view shows movement of anvils and flow of gasket and pressure medium during deformation by advancement (a) and retraction of differential rams (b). The arrows indicate the direction of movement or flow.

may be due to the flow of gasket and pressure medium between the anvils. As shown in Fig. 2.8a, the material tend to flow from the horizontal anvil gaps to vertical anvils gaps with the advancement of top and bottom anvils. This flow will drive the tension of the sample column which was located at the center of the pressure medium, and vice versa in the case of retraction of differential rams (Fig. 2.8b).

Results of deformation experiments were summarized in Table 2.1. The uniaxial tensional experiments were performed with strain of ε~0.25 (M1462), 0.33 (M1436) and 0.43 (M1395) corresponding to strain rate of $\dot{\varepsilon}$~1.39×10^{-4} s^{-1}, 0.96×10^{-4} s^{-1}, and, 1.36×10^{-4} s^{-1} respectively. Strain and strain rate of uniaxial compression experiments (M1515) were calculated to be ε~0.1 and $\dot{\varepsilon}$~0.42×10^{-4} s^{-1}, respectively. The strain of shear deformation

Table 2.1
Experimental conditions and results.

Run NO.[#]	Deformation geometry	Assembly[*]	Strain	Averaged strain rate (s^{-1})[§]
M1395	Tension	a	Ɛ=0.43	$\dot{\varepsilon}=1.36\times10^{-4}$
M1515	Compression	a	Ɛ=0.1	$\dot{\varepsilon}=0.42\times10^{-4}$
M1436	Tension	a	Ɛ=0.33	$\dot{\varepsilon}=0.96\times10^{-4}$
M1462	Tension	a	Ɛ=0.25	$\dot{\varepsilon}=1.39\times10^{-4}$
M1397	Simple shear	b	γ=1.0	$\dot{\gamma}=2.90\times10^{-4}$

[#] All the experiments were conducted at 12 GPa and 1600 °C.

[*] The cell assembly a and b represent the assemblies showed in Fig. 2.3a and Fig. 2.3b respectively.

[§] Strain rate was calculated with the time of deformation stage.

experiment was estimated to be γ~1 from the rotation of strain marker to ~45°and strain rate is $\dot{\gamma}$~2.90×10^{-4} s^{-1} (M1397).

Fig. 2.9 (a-g) shows the microstructure of synthesized and deformed samples. Before deformation, the sample shows equigranular texture with grain size of 5-10 µm (Fig. 2.9a). After tensional deformation, the original cylindrical shaped stishovite aggregates changed to inverse barrel-like shape (Fig. 2.9b), whereas, the compressional deformed sample changed to barrel-like shape (Fig. 2.9d). The microstructure of recovered samples show protomylonitic structures with large porphyloclasts (5-10 µm) and small recrystallized grains) (~1 µm, Fig. 2.9c, e, g). The dominant deformation mechanism is considered to be dislocation creep because the dynamic recrystallization were observed in all the samples.

The pole figures and inverse pole figures of synthesized and tensional, compressional and shear deformed samples are shown in Fig. 2.10. The patterns of sample before

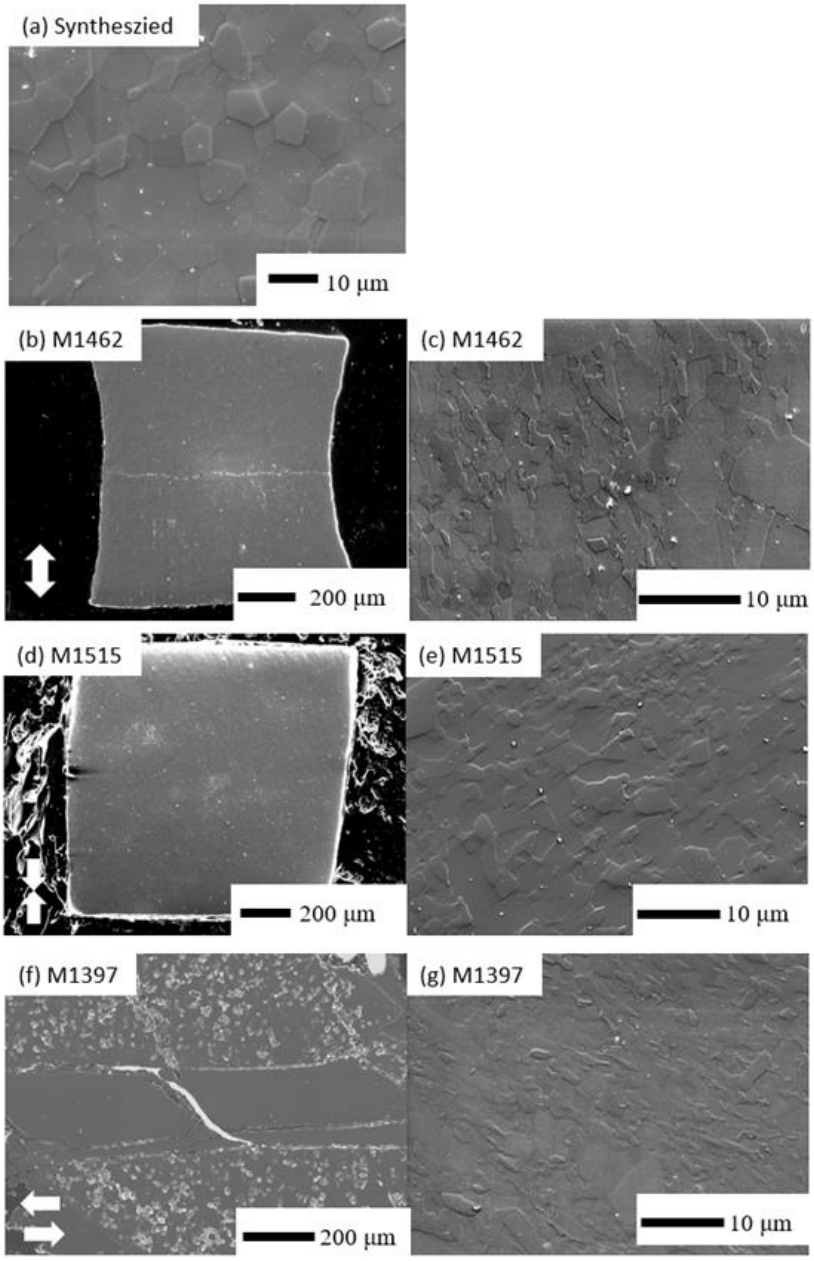

Fig. 2.9. Representative secondary electron images of recovered samples. SEI images of synthesized stishovite (a), uniaxial tension experiment (b and c, M1462), uniaxial compression experiment (d and e, M1515) and simple shear deformation experiment (f and g, M1397). The samples were sectioned parallel to the shear direction and shear plane normal.

deformation indicated crystal orientation with almost random distribution (Fig. 2.10a). Results of tensional experiments (Fig. 2.10b, c and d) showed that the [001] axes are preferentially subparallel to the elongation direction. Both the <100> and <110> axes lie on the plane normal to the elongation direction. In the inverse pole figures, the uniaxial tension direction concentrates near the [001] axes position. The pole figure of compressional deformation experiment (Fig. 2.10e) shows little concentration of the <100> or <110> axes, but the [001] axes is oriented on the plane normal to the compression direction. Also indicated by the inverse pole figure, the direction normal to the compressional direction concentrate on the [001] axes. The uniaxial compression direction distributes both <100> and <110> axis and does not show obvious preference.

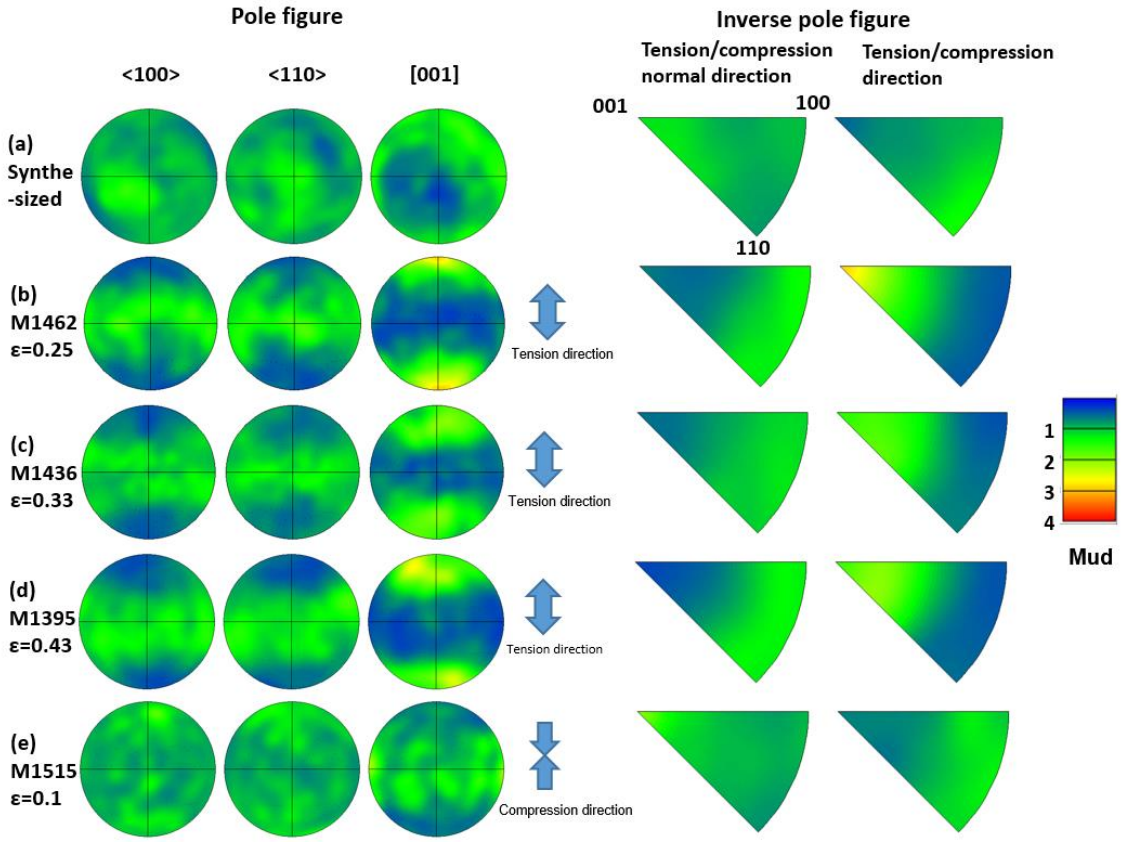

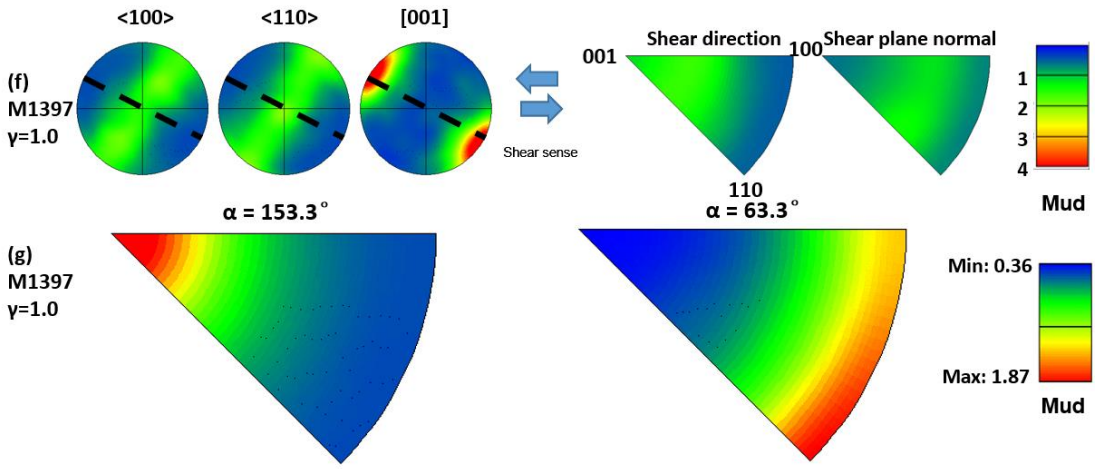

Fig. 2.10. Pole figures and inverse pole figures of stishovite before and after deformation with equal area upper hemispheres projections. The samples were synthesized (a), uniaxial tension experiment (b, M1462; c, M1436; d, M1395), uniaxial compression experiment (e, M1515) and simple shear deformed (e, M1397). The lines in figure (f) were at angle 63.3°, which is the direction perpendicular to the long axis of strain ellipsoid. Inverse pole figure along the direction parallel (α=153.3°) or perpendicular (α=63.3°) to the long axis of strain ellipsoid direction were also shown (g). Note that the degree of concentration of data represent by color in the inverse figure perpendicular to the long axis of strain ellipsoid direction is different from others. A half-width of 20° and cluster size of 10° was used for plotting and contouring (same conditions applied for current chapter).

The pole figure of shear deformation experiment (M1397, Fig. 2.10f) shows significant concentration of the [001] axes subparallel to the long axis of strain ellipsoid, which was calculated to be 153.3° for γ=1 (broken line in Fig. 2.10f). Both the <100> and <110> axes concentrated on the plane perpendicular to the long axis of strain ellipsoid. The strong concentration of the [001] axes parallel to the long axis of the strain ellipsoid was also shown in the inverse pole figure (Fig. 2.10g). The inverse pole figure plotted for the direction perpendicular to the long axis of strain ellipsoid showed obviously that the concentration of

<110> axes is the highest among all the crystallographic axes.

2.3.2. Result of deformation experiment on α-PbO_2

Microstructure of α-PbO_2 aggregate recovered from synthesis and deformation experiments are shown in Fig. 2.11. The synthesized sample shows equigranular texture with grain size of 10-20 μm (Fig. 2.11a). Initially, sample was polished with alumina piston as shown in Fig. 2.11b, c and d. The dense Al_2O_3 was largely advanced with deformation and extrude the sample out. The geometry of strain marker shows that the sample was deformed nearly homogeneously at the scale of sample thickness with strain of γ~1.3 and strain rate of $\dot{\gamma}$ ~4.3×10^{-4} s^{-1}. The large difference in hardness between alumina and α-PbO_2 makes the sample very challenging to be well polished (Fig. 2.11c and d). Furthermore, the polished grains turn to be cluster of small grains compared with the relatively well kept unpolished grains. We re-polished α-PbO_2 sample after separation from alumina pistons for further EBSD measurement (Fig. 2.11e and f). All the grains were polished with showing serrated grain boundaries (Fig. 2.11e and f). Small grains with straight grain boundaries can be observed in the large grain domains.

Fig. 2.12 shows the pole figure and inverse pole figure of deformed sample obtained by EBSD measurement. Because of the low quality of surface condition, ~60% of the measured data were indexed as α-PbO_2. The pole figure shows significant concentration of the [010] direction subparallel to the shear plane normal direction. The [001] direction preferred oriented along the shear direction. Although more concentrated perpendicular to shear direction and shear plane normal direction, [100] direction tend to distribute on the

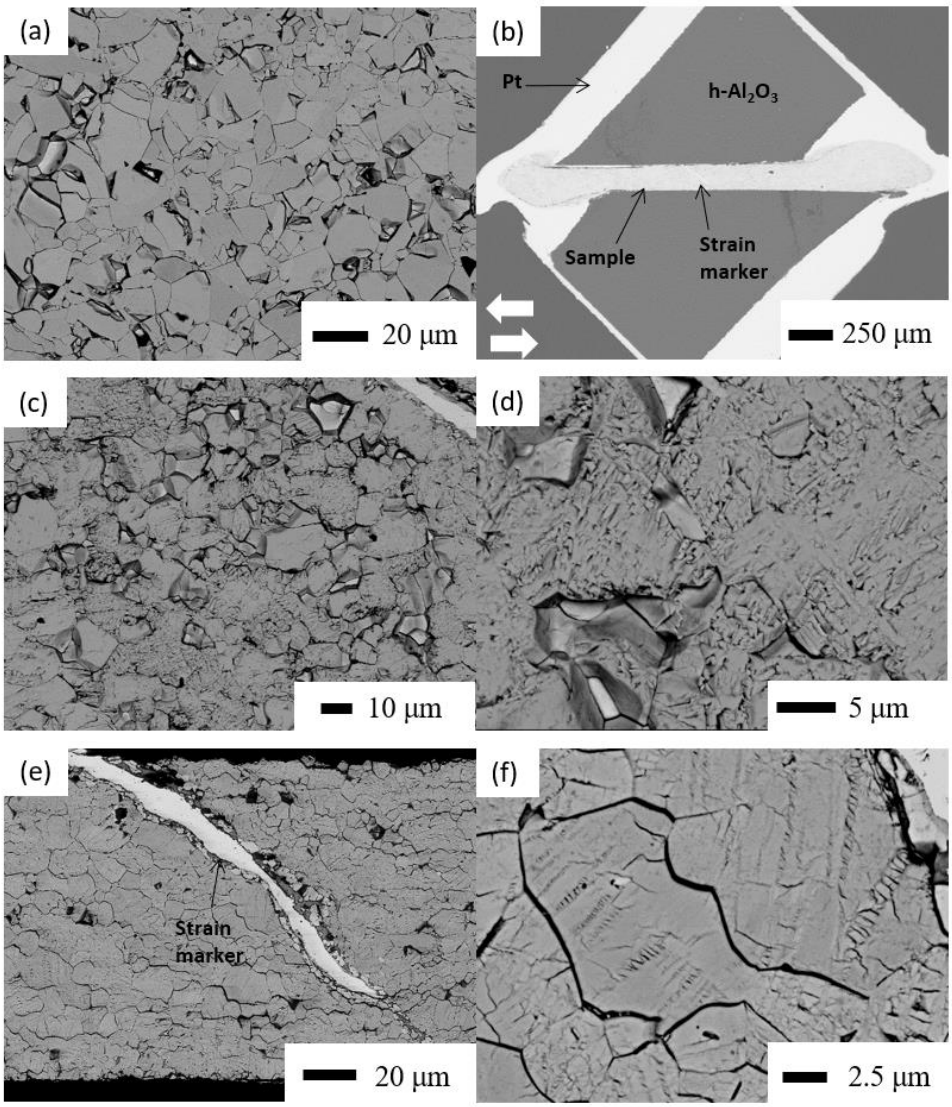

Fig. 2.11. Representative secondary electron images of recovered samples. SEI images of synthesized α-PbO_2 (a) and simple shear deformation experiment (b-f, D022). The samples were sectioned parallel to the shear direction and shear plane normal.

shear plane as a girdle. The inverse pole figure plotted for the shear direction and shear plane normal direction showed concentration of [001] and [010] direction, respectively.

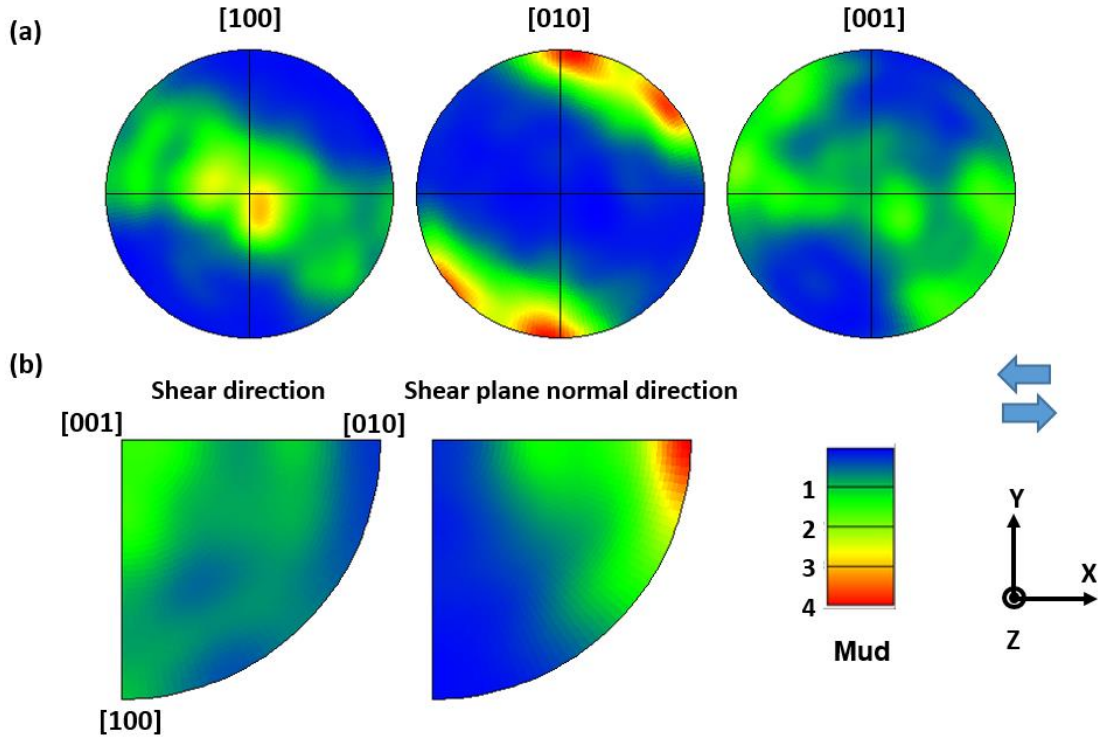

Fig. 2.12. Pole figures (a) and inverse pole figures (b) of shear deformed α-PbO_2 measured by EBSD with equal area upper hemispheres projections. The arrows indicate the shear sense. Coordination of sample geometry was used. The color coding refers to the density of data points and the number in the legend indicates the multiples of the uniform distribution (Mud). A half-width of 20 ° and cluster size of 10° was used for plotting and contouring.

Fig. 2.13 shows the pole figure and inverse pole figure of deformed sample obtained by 2D X-Ray diffraction method with ReciPro. The [010] direction shows consistent concentration with EBSD measurement with alinement along the shear plane normal direction. However, [100] direction turns to be subparallel to the shear direction, which is inconsistent with the result indicated by the EBSD measurement. This discrepancy was also shown in the inverse pole figure, with [100] direction concentrated on the shear direction. As

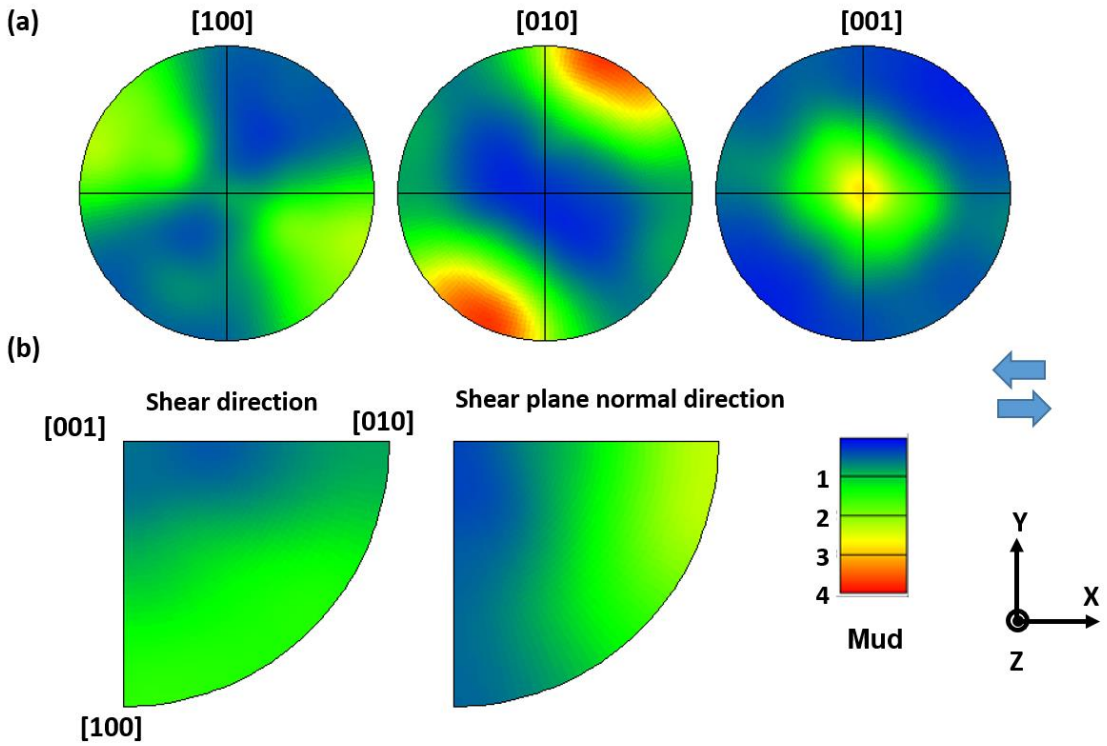

Fig. 2.13. Pole figures (a) and inverse pole figures (b) of shear deformed α-PbO_2 obtained by 2D X-ray diffraction using ReciPro.

shown in Fig. 2.14, the CPO of the deformed α-PbO_2 from the ReciPro and MAUD software programs were confirmed to be same. The coincident pattern from different algorithms used in each program convince us the simulating process.

2.4. Discussion

2.4.1. Dominant slip system

The slip direction of stishovite was determined to be the [001] direction based on the LPO formed by the tensional deformation (Fig. 2.10b-d). However, as the limited strain in the compressional deformation experiment, neither the <100> nor the <110> axes show

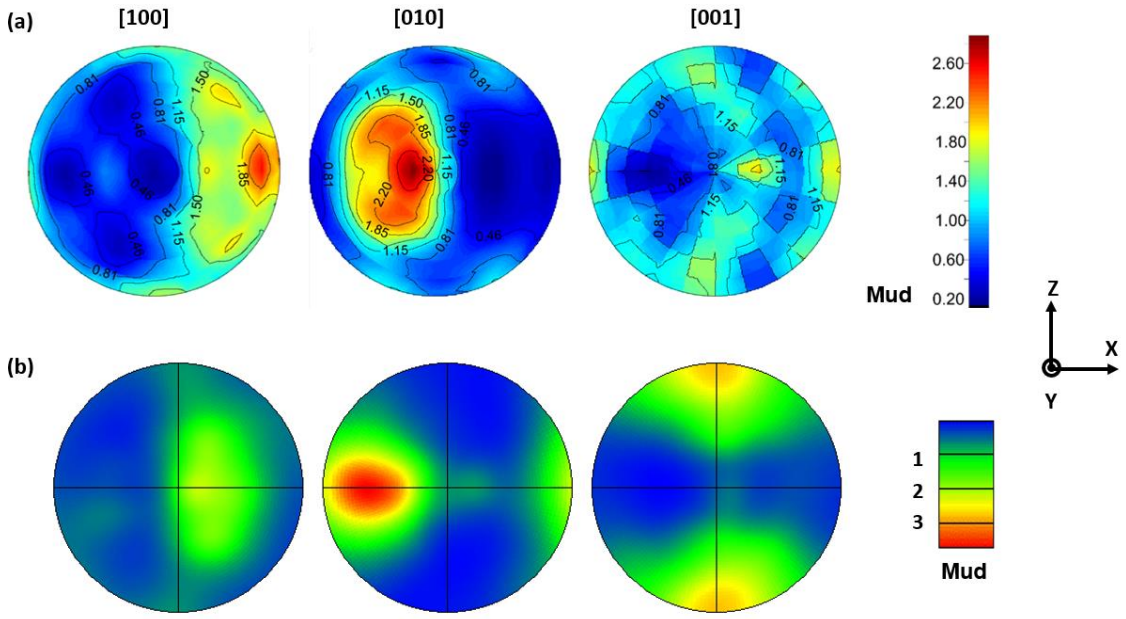

Fig. 2.14. Pole figures of shear deformed α-PbO_2 obtained by 2D X-ray diffraction using software of MAUD (a) and ReciPro (b). Note that (b) was obtained from changing coordination based on Fig. 2.13.

obvious preferred concentration. It is hard to identify which one is the most dominant slip plane. Therefore, the shear deformation experiment was conducted with strain as large as 1.0. The higher concentration of the <110> axis than the <100> axis reveal that the {110} plane is the preferable slip plane. Combine the result of both uniaxial deformation experiment and shear deformation experiment, the most dominant slip system of stishovite at high temperature and high pressure was determined to be [001] {110}.

Strong concentration of the [010] direction of α-PbO_2 along shear plane normal direction from both EBSD and 2D X-ray diffraction measurement consistently indicates the dominate slip plane of the (010) plane. Results from EBSD and 2D X-ray diffraction measurement show different pattern with the [001] and [100] subparallel to the shear direction, respectively.

Although EBSD was considered to be the most direct forward and high resolution method to measure LPO, the surface of highly deformed sample may not match the requirement for EBSD measurement (Karato, 2008). The low index ratio of EBSD measurement in this study may induce artifact in the LPO pattern, i.e. grains with certain orientation were better polished and selected indexed. With considering this, the LPO pattern derived from 2D X-ray diffraction measurement was used to infer the slip system of α-PbO_2. Therefore, the experimental textures indicate the orientation producing deformation mechanisms is [100](010).

Stishovite assumes the rutile structure which is characterized by six-folded coordination of silicon by oxygen (Stishov and Popover., 1961; Sinclair and Ringwood., 1978). The six-coordinated Si octahedra are edge-shared along the *c*-axes and corner-shared along *a*-axes with lattice constants of $a=b=4.18$ Å and $c=2.6678$ Å (Fig. 2.15a). From a mineralogical point of view, dislocation glide along the *c*-axes is expected to be easier because it does not break the strong edge-shared Si bond along the *c*-axes. The predominance of gliding along the *c*-axes is also consistent with strong concentration of the [001] direction as shown in the maximum mud in the pole figure (Fig. 2.10f). On the contrary, the priority of slip plane of {110} is weaker, which only can be identified at higher strain in the shear experiment (Fig. 2.10g). This is because the Si-O are both corner-shared on the {110} and the {100} plane (Fig. 2.12b). The choice of glide plane may be related with the density of Si-O bond breaking associated with dislocation glide in the certain plane (Texier and Cordier, 2006). As shown in Fig. 2.12b, for the slip on the {110} and the {100} plane, the number of Si-O bonds breaking on the {110} is obviously smaller compared with {100} plane. The consistency,

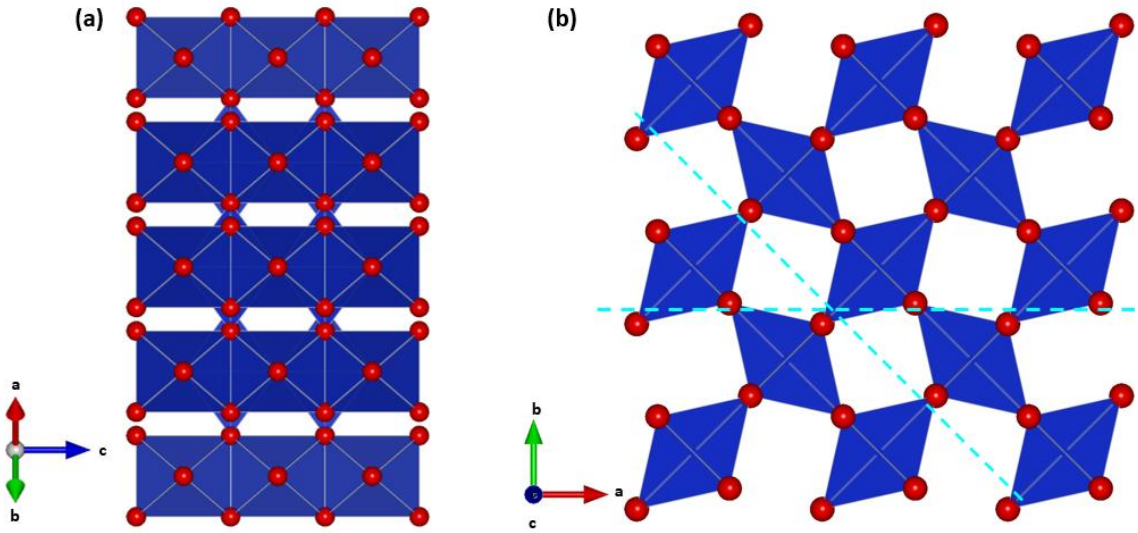

Fig. 2.15. Structure of rutile-type stishovite viewed along the <110> (a) and [001] (b) direction. Si^{4+} cations (small blue circle) are centered among six O^{2-} anions (red circles) in an octahedral arrangement (blue octehedra). Dashed aqua lines in (b) are with same length which indicate different slip plane.

from another point of view, supports the feasibility of prediction of slip system from atomic level.

Distorted from stishovite rutile structure, SiO_6 octehedra are arranged into kinked chains extending along the [001] direction in α-PbO_2 structure (Fig. 2.16) with unit-cell parameters *a*=4.097, *b*=5.0462, *c*=4.4946 Å and space group *Pbcn* (Grocholski et al., 2013). α-PbO_2 structure shows more compact configuration with the kinked chains along *c*-axes and shorter distance of the stacking octahedra along *a*-axes. The preferred slip plane of (010) is compatible with the strong bonding along *a* and *c*-axis. Although the *c*-axis was expected to be strongest due to the edge shared octahedra, the LPO indicate slip direction along *a*-axis during deformation. This may indicate other factors, rather than elastic energy, dominate the

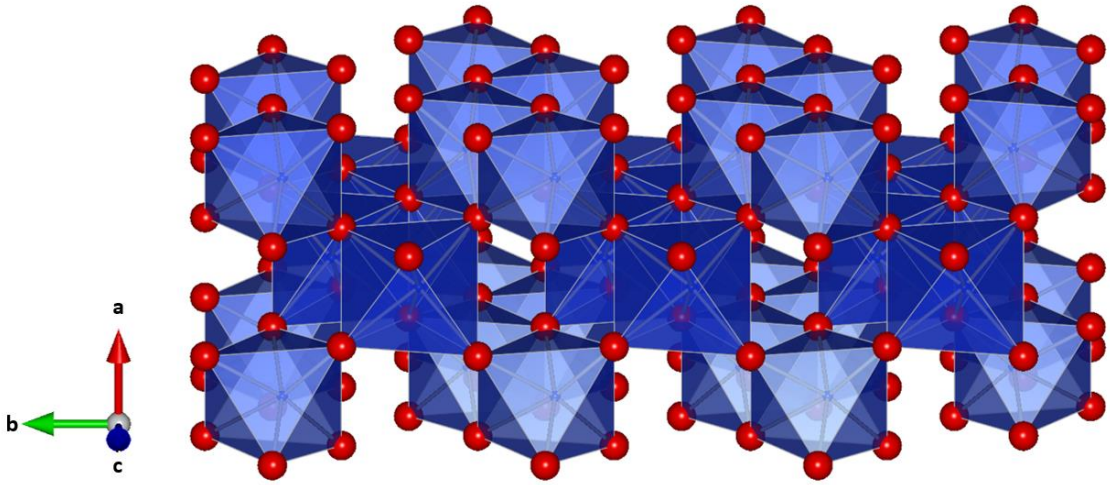

Fig. 2.16. Polyhedral representation of the crystal structure of α-PbO_2 type SiO_2, seifertite. The octahedral are depth shaded to aid in distinguishing top and bottom layers of SiO_6 octahedra, lighter blue, from sandwiched layer, darker blue.

deformation mechanism during deformation of α-PbO_2.

The slip system of stishovite obtained in this study is consistent with Cordier et al. (2004) and Texier and Cordier (2006) in slip direction, except their failure of constraint in slip plane. Compared with the small elastic strain accumulated during compression in their stress relaxation experiment, large strain generated in the shear deformation experiment play an important role to specify the slip plane. Deformation at high pressure and room temperature using DAC reported by Kaercher et al. (2014) suggested the (001) as the dominant slip plane, in contradiction with our results. The contrasting results might be caused by different deformation mechanism, i.e. Piers mechanism rather than dislocation creep, for the development of LPO of stishovite as the high deviatoric stress generated in their experiment at room temperature, which was observed in mantle minerals such as bridgmanite

Table 2.2
Experimentally determined dominate slip systems in rutile structure.

Compos-ition	Burgers vector	Glide plane	P (GPa)	T (°C)	Ref
SiO_2	[001]	{110}	12	1600	This study
	[001]	{110}, {100}	14	1300	Cordier et al. (2004)
	[001]	{100}, {210}	14	1300	Texier and Cordier (2006)
	ND[#]	(001)	38	RT[*]	Kaercher et al. (2014)
TiO_2	<101>	{101}	RP[*]	527- 1427	Ashbee and Smallman (1963), Blanchin and Fontaine (1975),
TeO_2	<100>	(001)	RP	733	Péter et al. (1986)

[#] Not determined.
[*] RT and RP represent room temperature and room pressure respectively.

(Tsujino et al., 2016; Miyagi et al., 2016), ringwoodite (Kawazoe et al., 2016) and wadsleyite (Kawazoe et al., 2013).

Several studies have been done on stishovite isostructural minerals (Table 2.2) such as rutile and paratellurite (TeO_2). Single crystals of rutile were deformed at high temperature (527-1427 °C) and ambient pressure (Ashbee and Smallman, 1963; Blanchin and Faisant., 1975). Uniaxial compressional experiments were conducted along specific crystallographic orientation of single crystals, i.e. [001], <100> and <110> directions in Ashbee and Smallman (1963) and [001] direction in Blanchin and Faisant. (1975). Similarly, deformation experiments were conducted on paratellurite (TeO_2) single crystals, which shows 'rutile like' structure by stacking two rutile unit cell along [001] axis in Péter et al. (1986). Uniaxial stress was applied along [110], [100], [001] and [221] directions of paratellurite single crystals at ambient pressure and high temperature (415-685 °C). TEM observations showed the dominant slip system with <101>{101} in rutile (Ashbee and Smallman, 1963; Blanchin and

Faisant., 1975). Optical microcopy and X-ray tomography suggested <010>(001) slip was the easiest slip system in paratellurite (Péter et al., 1986). According to the definition of Schimd factor, only limited slip systems can be possibly activated in deformation on single crystals, e.g. <101>{101}, <101>{111} and <111>{101} in Ashbee and Smallman (1963). Slip system of stishovite reported in present study ([001]{110}) can not be activated in these studies. So the difference was highly possibly caused by the limited activated slip systems in deformation on single crystals. To evaluate the systematic series in rutile structure, high temperature and high pressure deformation experiments on polycrystalline materials are required.

2.4.2. Implication for seismic anisotropy in the mantle

As mentioned earlier, the observed seismic anisotropy around subduction slab in the lower MTZ is difficult to be explained by the subducted peridotite layer. We considered the contribution of stishovite to seismic anisotropy based on the LPO and slip system determined in present study combined with elasticity. We calculated the seismic anisotropy of deformed stishovite based on the LPO obtained in simple shear deformation experiment (M1397) and density and elastic constants of stishovite single crystals (Yoneda et al., 2011) (Fig. 2.17) by using the software developed by Mainprice (1990). In shear deformation sample (M1397), the propagation direction of fastest P-waves and the polarization direction of the fast S-waves tends to be subparallel to the long axis of strain ellipsoid direction. The anisotropy of S-waves perpendicular to the strain ellipse direction is larger than parallel. The anisotropy of both P- and S-waves reach to ~6.5% at the shear strain of γ= 1.0 (M1397). The high magnitude of seismic anisotropy indicates that LPO of stishovite may contribute to the anisotropy although

dilution effect of garnet and ringwoodite are considered. Stishovite was considered to be harder than garnet and ringwoodite. Similar with experimentally and naturally deformed eclogite, certain strain in garnet was observed although coexisted omphacite is much softer (e.g. Zhang and Green, 2007; Jin et al., 2001). Stishovite is expected to be deformed to some extent in the composite with garnet depending on the strength contrast and geometry of garnet and stishovite.

To explain observed seismic anisotropy by LPO of deformed stishovite, $V_{SH} < V_{SV}$ polarization anisotropy reported by Visser et al. (2008) could be caused by locally vertical flow in the mantle transition zone. This is consistent with the flow pattern inferred from wadsleyite and seismic anisotropy in the upper mantle transition zone with predominance of horizontal flow with local contribution of vertical flow (Kawazoe et al., 2013). The vertical

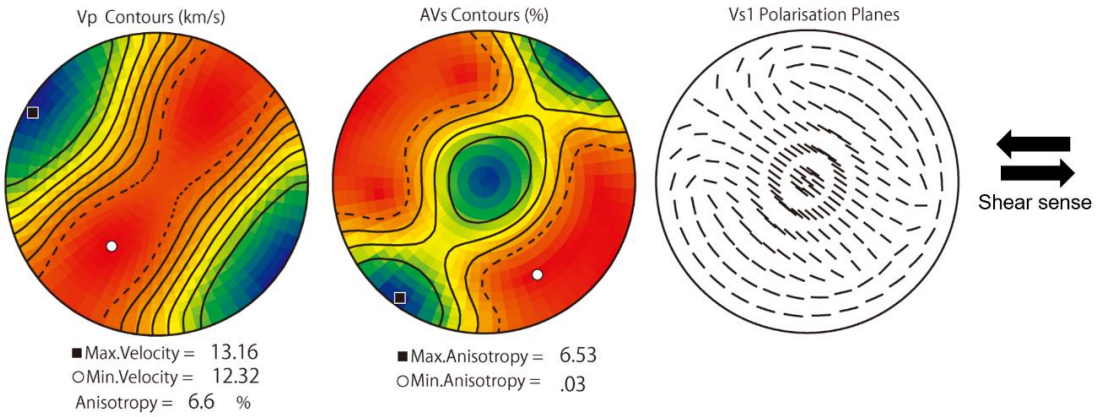

Fig. 2.17. Seismic anisotropy calculated from LPO data of stishovite (M1397). The shear direction is shown by arrows. The color indicate variation of P-wave seismic velocity (V_P, left) and S-wave anisotropy magnitude (AVs, middle) with direction of wave propagation. Dashes (right) denote orientation of polarization of the fast S-waves V_{S1} (right) with direction of wave propagation. Equal area upper hemisphere projections and inverse log scale are used.

flow related with stishovite also indicate the SiO_2-rich components may penetrated into the lower mantle, without horizontally accumulation at the bottom of mantle transition zone.

Although the experimental conditions in the present study is different from those in the D″ layer of the Earth, we assume the fabric information obtained here is applicable to the deep mantle conditions. In order to examine the seismic anisotropy in the D″ layer, we calculated the elastic wave velocities based on the LPOs obtained in this study together with the density and elastic constants of seifertite at 100 GPa (Karki et al., 1997) by using the software developed by Mainprice (1990). The propagation direction of slowest P-waves tends to be subparallel to the shear direction. This is because [100] direction, which is the slowest direction for P-wave in serifertite, is preferentially oriented subparallel to the shear direction (Fig. 2.17). The anisotropy of S-waves on the shear plane is larger than the direction

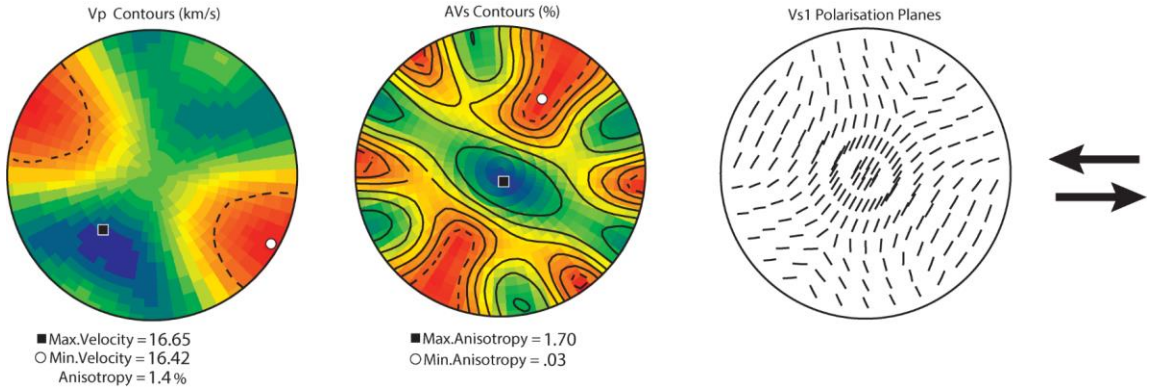

Fig. 2.18. Seismic anisotropy of serfertite at 100 GPa calculated from LPO data of α-PbO_2 (D022). The shear direction is shown by arrows. The color indicate variation of P-wave seismic velocity (V_P, left) and S-wave anisotropy magnitude (AVs, middle) with direction of wave propagation. Dashes (right) denote orientation of polarization of the fast S-waves V_{S1} (right) with direction of wave propagation. Equal area upper hemisphere projections and inverse log scale are used.

of the shear plane normal. The polarization direction of fast shear-wave, which corresponds to SV-wave in a horizontal flow, is perpendicular to the shear direction (on the shear plane). The sample produces 1.7% of shear-wave anisotropy in the polarization direction.

Most of the D″ layer flows horizontally as the subducting slab delaminate along the core-mantle boundary towards hotter regions of mantle upwelling. Here, we considered silica rich components including sediment, MORB layer and TTG are constantly injected into the mantle at the subduction zones. The heterogeneity may survive on a geologic timescale due to extremely sluggish solid state diffusion at mantle *P-T* conditions and possible high viscosity as indicated by Si and O diffusion in stishovite (see Chapter 3). Alternatively, Knittle and Jeanloz (1991) suggested that reaction between Mg-silicate and liquid iron may produce free silica together with iron oxide and iron silicide near the core-mantle boundary. Therefore, once free silica exist in the lowermost mantle as seifertite, they may contribute to the observed seismic anisotropy due to the strong dynamic at the core mantle boundary ((McNamara et al., 2002). According to the LPO obtained in this study, the observed faster horizontally polarization S-wave anisotropy under the circum Pacific region indicate a vertical flow with accumulated subducted material, which is inconsistent with the dominant horizontal flow in this region. This indicates an absence of large accumulation of seifertite in the D″ layer, the subducted SiO_2-rich components may be trapped in the lower mantle which were observed as seismic reflectors and scatters (e.g. Kaneshima, 2016).

Reference

Ashbee K H G., Smallman R E., 1963. The plastic deformation of titanium dioxide single

crystals. Proceedings of the Royal Society of London. Series A. Mathematical Phys. Sci., 274, pp. 195-205.

Blanchin M G., Fontaine G., 1975. Transmission electron microscope observations of deformed rutile (TiO_2). Phys. status solidi, 29, pp. 491-501.

Cordier P., Mainprice D., Mosenfelder JL., 2004. Mechanical instability near the stishovite-$CaCl_2$ phase transition implications for crystal preferred orientations and seismic properties. Euro. J. Min., 16, pp. 387-399.

Cordier P., Rubie D C., 2001. Plastic deformation of minerals under extreme pressure using a multi-anvil apparatus. Mat. Sci. Eng., 309, 38-43.

El Goresy, A., Dera, P., Sharp, T.G., Prewitt, C.T., Chen, M., Dubrovinsky, L., Wopenka, B., Boctor, N.Z., Hemley, R.J., 2008. Seifertite, a dense orthorhombic polymorph of silica from the Martian meteorites Shergotty and Zagami. Euro. J. Miner., 20, pp. 523-528.

Fukao, Y. and Obayashi, M., 2013. Subducted slabs stagnant above, penetrating through, and trapped below the 660 km discontinuity. J. Geophy. Res., 118, pp. 5920-5938.

Gerald Pacalo R E., Weidner D J., 1997. Elasticity of majorite, $MgSiO_3$ tetragonal garnet. Phys. Earth Planet. Int., 99, pp.145-154.

Grocholski, B., Shim, S.H., Prakapenka, V.B., 2013. Stability, metastability, and elastic properties of a dense silica polymorph, seifertite. J. Geophy. Res., 118, pp. 4745-4757.

Grocholski, B., Shim, S.H., Cottrell, E., Prakapenka, V.B., 2014. Crystal structure and compressibility of lead dioxide up to 140 GPa. American Mineralogist, 99, pp.170-177.

Hirose, K., Takafuji, N., Sata, N., Ohishi, Y., 2005. Phase transition and density of subducted MORB crust in the lower mantle. Earth Planet. Sci. Lett., 237, 239-251.

Irifune T, Ringwood A E., 1993. Phase transformations in subducted oceanic crust and buoyancy relationships at depths of 600–800 km in the mantle. Earth Planet. Sci. Lett., 117, pp. 101-110.

Irifune T, Ringwood A E, Hibberson W O., 1994. Subduction of continental crust and terrigenous and pelagic sediments: an experimental study. Earth Planet. Sci. Lett., , 126, pp. 351-368.

Jiang F, Gwanmesia G D, Dyuzheva TI et al., 2009. Elasticity of stishovite and acoustic mode softening under high pressure by Brillouin scattering. Phys. Earth Planet. Int., 172, pp. 235-240.

Jin, Z.M., Zhang, J., Green, H.W. and Jin, S., 2001. Eclogite rheology: Implications for subducted lithosphere. Geology, 29, pp. 667-670.

Kaercher PM, Zepeda-Alarcon E, Prakapenka V B, et al., 2014. Preferred orientation in experimentally deformed stishovite: implications for deformation mechanisms. Phys. Chem. Miner., 1-11.

Kaneshima. S, 2016. Seismic scatterers in the mid-lower mantle. Phys. Earth Planet. Inter., 257, pp. 105–114.

Karki, B.B., Stixrude, L., Crain, J., 1997. Ab initio elasticity of three high-pressure polymorphs of silica. Geophy. Res. Lett., 24, pp. 3269-3272.

Karato, S.I., 1989. Plasticity-crystal structure systematics in dense oxides and its implications for the creep strength of the Earth's deep interior: a preliminary result. Phys. Earth Planet. Int., 55, pp. 234-240.

Kawai K, Tsuchiya T, Tsuchiya J, Maruyama, S., 2009. Lost primordial continents.

Gondwana Res., 16, pp. 581-586.

Kawazoe T, Ohuchi T, Nishiyama N, et al., 2010. Preliminary deformation experiment of ringwoodite at 20 GPa and 1 700 K using a D-DIA apparatus. J. Earth Sci., 21, pp. 517-522.

Kawazoe T, Ohuchi T, Nishihara Y, Nishiyama N, Fujino K, Irifune T., 2013. Seismic anisotropy in the mantle transition zone induced by shear deformation of wadsleyite. Phys. Earth Planet. Int., 31, pp. 91-98.

Kawazoe T, Nishihara Y, Ohuchi T, Miyajima N, Maruyama G, Higo Y, Funakoshi KI, Irifune T. Creep strength of ringwoodite measured at pressure–temperature conditions of the lower part of the mantle transition zone using a deformation–DIA apparatus. Earth Planet. Sci. Lett., 2016, 454, 10-19.

Knittle, E., R. Jeanloz, 1991. Core-mantle boundary: results of experiments athigh pressures and temperatures. Science, 251, 1438-1443.

Komabayashi, T., Maruyama, S., Rino, S., 2009. A speculation on the structure of the D" layer: The growth of anti-crust at the core-mantle boundary through the subduction history of the Earth. Gondwana Res., 15, 342-353.

Lebensohn R, Tomé C., 1994. A self-consistent viscoplastic model: prediction of rolling textures of anisotropic polycrystals. Mater Sci. Eng., 175:71–82

Luo, S.N., Çağin, T., Strachan, A., Goddard, W.A. and Ahrens, T.J., 2002. Molecular dynamics modeling of stishovite. Earth Planet. Sci. Lett., 202, pp. 147-157.

Lutterotti, L., M. Bortolotti, G. Ischia, I. Lonardelli, and Wenk H. R., 2007. Rietveld texture analysis from diffraction images, Z. Kristallogr. Suppl., 26, 125-130.

Mainprice D., 1990. A FORTRAN program to calculate seismic anisotropy from the lattice preferred orientation of minerals. Comp. & Geos., 16, pp. 385-393.

Montagner J P, Kennett B L N. How to reconcile body-wave and normal-mode reference Earth models. Geophys. J. Int., 1996, 125, pp. 229-248.

Miyagi L, Wenk HR., 2016. Texture development and slip systems in bridgmanite and bridgmanite+ ferropericlase aggregates. Phys. Chem. Miner., 1-7.

McNamara, A.K., Van Keken, P.E., Karato, S.I., 2002. Development of anisotropic structure in the Earth's lower mantle by solid-state convection. Nature, 416, pp. 310-314.

Nishihara Y., 2008. Recent technical developments of high-pressure deformation experiments. Rev. High Pressure Sci. Tech., 18.

Nishiyama, N., Wang, Y., Sanehira, T., Irifune, T., Rivers, M.L., 2008. Development of the multi-anvil assembly 6-6 for DIA and D-DIA type high-pressure apparatuses. High Pressure Res., 28, pp.307-314.

Nowacki, A., Wookey, J., Kendall, J.-M., 2010. Deformation of the lowermost mantle from seismic anisotropy. Nature, 467, pp. 1091-1094.

Tsujino, N., Nishihara, Y., Yamazaki, D., Seto, Y., Higo, Y., Takahashi, E., 2016. Mantle dynamics inferred from the crystallographic preferred orientation of bridgmanite. Nature, 539, pp. 81-84.

Ohuchi T, Fujino K, Kawazoe T, et al., 2014. Crystallographic preferred orientation of wadsleyite and ringwoodite: Effects of phase transformation and water on seismic anisotropy in the mantle transition zone. Earth Planet. Sci. Lett., 397, pp. 133-144.

Péter A, Fries E, Janszky J, et al., 1986. Dislocations in paratellurite TeO2: elastic energies

and plastic deformation. Revue de physique application, 21, pp. 289-298.

Panning, M. and Romanowicz, B., 2004. Inferences on flow at the base of Earth's mantle based on seismic anisotropy. Science, 303, pp.351-353.

Panning M, Romanowicz B., 2006. A three-dimensional radially anisotropic model of shear velocity in the whole mantle. Geophys. J. Int., 167, pp. 361-379.

Seto, Y., 2012. Whole pattern fitting for two-dimensional diffraction patterns from polycrystalline materials. Rev. High Press. Sci. Technol. 22, pp. 144-152.

Ritsema, J., Ni, S., Helmberger, D.V. and Crotwell, H.P., 1998. Evidence for strong shear velocity reductions and velocity gradients in the lower mantle beneath Africa. Geophys. Res. Lett., 25, pp. 4245-4248.

Sinogeikin S V, Bass J D., 2000. Single-crystal elasticity of pyrope and MgO to 20 GPa by Brillouin scattering in the diamond cell. Phys. Earth Planet. Inter., 120, pp. 43-62.

Stishov SM, Popova SV., 1961. New dense polymorphic modification of silica. Geochem., 10, pp. 923-926.

Texier M, Cordier P., 2006. TEM characterization of dislocations and slip systems in stishovite deformed at 14 GPa, 1,300° C in the multianvil apparatus. Phys. Chem. Miner., 33, pp. 394-402.

Thurel E, Cordier P., 2003. Plastic deformation of wadsleyite: I. High-pressure deformation in compression. Phys. Chem. Miner., 30, pp. 256-266.

Tsujino N, Nishihara Y, Yamazaki D, Seto Y, Higo Y, Takahashi E., 2016. Mantle dynamics inferred from the crystallographic preferred orientation of bridgmanite. Nature, 539, 81-84.

Xu, F., Yamazaki, D., Sakamoto, N., Sun, W., Fei, H. and Yurimoto, H., 2016. Silicon and oxygen self-diffusion in stishovite: Implications for stability of SiO_2-rich seismic reflectors in the mid-mantle. Earth Planet. Sci. Lett., 459, pp. 332-339.

Visser K, Trampert J, Lebedev S, et al., 2008. Probability of radial anisotropy in the deep mantle. Earth Planet. Sci. Lett., 270, pp. 241-250.

Wang, Y., Durham, W.B., Getting, I.C. and Weidner, D.J., 2003. The deformation-DIA: A new apparatus for high temperature triaxial deformation to pressures up to 15 GPa. Rev. Sci. Instr., 74(6), pp.3002-3011.

Weidner D J, Bass J D, Ringwood A E, et al., 1982. The single‐crystal elastic moduli of stishovite. J. Geophys. Res., 87, pp. 4740-4746.

Weidner D J, Sawamoto H, Sasaki S, et al., 1984. Single−crystal elastic properties of the spinel phase of Mg2SiO4. J. Geophys. Res., 89, pp. 7852-7860.

Yagi, T., Akimoto, S.I., 1980. Phase boundary and transition rate of orthorhombic-cubic transformation in PbO_2. J. Geophys. Res., 85, pp. 6991-6995.

Yamazaki, D., Yoshino, T., Ohfuji, H., Ando, J.I, Yoneda, A., 2006. Origin of seismic anisotropy in the D" layer inferred from shear deformation experiments on post-perovskite phase. Earth Planet. Sci. Lett., 252, pp.372-378.

Yoneda A, Cooray T, Shatskiy A. Single-crystal elasticity of stishovite: New experimental data obtained using high-frequency resonant ultrasound spectroscopy and a Gingham check structure model. Phys. Earth Planet. Inter., 2012, 190: 80-86.

Zhang, J. and Green, H.W., 2007. On the deformation of UHP eclogite: from laboratory to nature. International Geology Review, 49, pp. 487-503.

Chapter 3. Silicon and oxygen self-diffusion in stishovite implications for stability of SiO2-rich seismic reflectors in the mid-mantle

Abstract

Seismic reflectors were observed in the mid-mantle, which was considered to origin from former subducted SiO_2-rich fragments such as mid-oceanic basalt (MORB), continental crust (CC) and/or tonalite–trondhjemite–granodiorite (TTG). For the preservation of such platy shape seismic reflectors in the vigorous convecting mantle, viscosity plays an important role. Therefore, the viscosity of stishovite, stable phase of SiO_2 until mid-mantle with rutile structure, will be one of the key parameter to constrain the mixing up of seismic reflector with surrounding mantle. In diffusion creep and climb controlled dislocation creep region, creep rate is dominated by the diffusion of the slowest species. Thus, as the excluding constituting elements in stishovite, diffusivity of Si and O was studied in this study.

Diffusion of Si and O in single crystal stishovite was examined at pressures of 14.0-21.5 GPa and temperatures of 1673-2073 K. Self-diffusion coefficients of Si and O are expressed as Arrhenius equation: $D = D_0 \exp(-(\Delta E + P\Delta V)/RT)$, with $\log D_0 = -11.6 \pm 1.0$ $\log(m^2/s)$, $\Delta E = -237 \pm 65$ kJ/mol, $\Delta V = 6.0 \pm 1.0$ cm^3/mol for Si and $\log D_0 = -10.1 \pm 3.0$ $\log(m^2/s)$, $\Delta E = -263 \pm 103$ kJ/mol, $\Delta V = 4.8 \pm 1.7$ cm^3/mol for O. It was revealed that diffusion of Si is approximately one order of magnitude slower than that of O and, thus, Si is the rate-controlling element for plastic deformation of stishovite. Si diffusion in stishovite is assessed to be at least three orders of magnitude slower than that in bridgmanite under mid-mantle conditions. Therefore, it is anticipated that highly viscous SiO_2-rich components subducted into the lower mantle persist as the seismic reflectors for long term without mixing up with the bridgmanite-dominated surrounding mantle.

3.1. Introduction

A number of seismic reflectors have been discovered beneath the circum-Pacific region in the mid-mantle from 800 to 1800 km depths (Kaneshima and Helffrich, 1999, 2003; Castle and Creager, 1999; Niu et al., 2003) (recently reviewed by Kaneshima, 2016). The seismic reflectors are characterized by a sharp reduction in shear wave velocity by 2~8 % compared with the surrounding mantle, laterally extending over several hundred km with a thickness of 8-12 km (Kaneshima and Helffrich, 1999, 2003; Castle and Creager, 1999; Niu et al., 2003). Platy shaped elastically distinct fragments would be responsible to the seismic reflectors. It was revealed that the rutile-$CaCl_2$ type transition in SiO_2 displays second-order character (Nomura et al., 2010). Shear modulus of the rutile type decreases with pressure and reaches zero at the transition pressure and that of the $CaCl_2$ type, in turn, increases at higher pressures (Carpenter et al., 2000). The resultant decrease in V_S amounts to some 25 % at the transition pressure of 50 GPa (at 300 K) (Carpenter et al., 2000). Therefore, it is expected that rutile-$CaCl_2$ type transition is capable of making V_S of the SiO_2-rich layers be lower than that of the surrounding mantle and emit the reflected waves over depths of a few hundred km around the transition depth. It has been argued that SiO_2-rich fragments, such as mid-oceanic basalt (MORB), continental crust (CC) and/or tonalite–trondhjemite–granodiorite (TTG), carried into the lower mantle by ancient subduction would be responsible for the seismic reflectors (Kaneshima and Helffrich, 2009; Tsuchiya et al., 2011; Hirose et al., 2005; Nomura et al., 2010). High pressure equilibrium studies on the SiO_2-rich fragments revealed that rutile type SiO_2 (stishovite) composes 20 vol.% in MORB (Ono et al., 2001), 35 vol.% in CC (Ishii et al., 2012), and 70 vol.% in TTG (Komabayashi et al., 2009), respectively.

The seismic reflectors, however, would be dissipated by vigorous mantle convection on geologic time scales. On the other hand, a chemically distinct region with greater viscosity can be kept undisturbed from mixing up with the surrounding mantle for a geologic period (Manga, 1996). For preservation of the observed SiO_2-rich seismic reflectors, therefore, viscosity of stishovite would play an important role.

Plastic deformation of minerals is dominated by diffusion creep and/or dislocation creep in the lower mantle. In diffusion creep, deformation occurs through mass transportation by atomic diffusion (Nabarro, 1948; Herring, 1950). In dislocation creep at high temperature, dislocation climb is regarded as the rate limiting process of deformation and is also controlled by atomic diffusion (Weertman, 1999; Frost and Ashby 1982). In both the mechanisms, therefore, diffusion is a major factor controlling viscosity of the mantle minerals.

Si diffusion in stishovite was first studied by Shatskiy et al. (2010) at 14 GPa. Nevertheless, the pressure dependence of the diffusion coefficient, which is vital to extrapolate it to the deep mantle conditions, is still unknown. On the other hand, O diffusion in stishovite has never been examined yet. Thus, we simultaneously studied the pressure dependence of Si and O diffusion in stishovite up to 21.5 GPa and 2073 K. We estimated the viscosity contrast between stishovite dominated fragments and surrounding bridgmanite dominated mantle under mid-mantle condition based on the diffusivities obtained in this study. Implications to the preservation of the observed SiO_2-rich seismic reflectors in the mid-mantle was discussed.

3.2. Experimental procedures

3.2.1. Starting materials

Single crystals of stishovite were synthesized by slow cooling method (Shatskiy et al., 2010) in the Kawai-type multianvil apparatus installed at Institute for Planetary Materials, Okayama University, Japan. Pressure was generated by octahedral pressure medium with eight truncated tungsten carbide (WC) anvils, so called 6-8 type. The starting material of reagent-grade silicic acid, which contains ~13 wt.% H_2O, was welded in the Pt capsule under liquid nitrogen to keep the water solvent. As shown in the Fig. 3.1, the capsule was shift from the center of heater for 0.4 mm to generate thermal gradient. The sample was compressed to 12 GPa at room temperature, sequentially heated to 1873 K, and then cooled to 1473 K with a rate of 100 K/hr. After recovery, we picked up crack- and inclusion-free crystals with sizes from 0.5 to 1.0 mm under the optical microscope (Fig. 3.2).

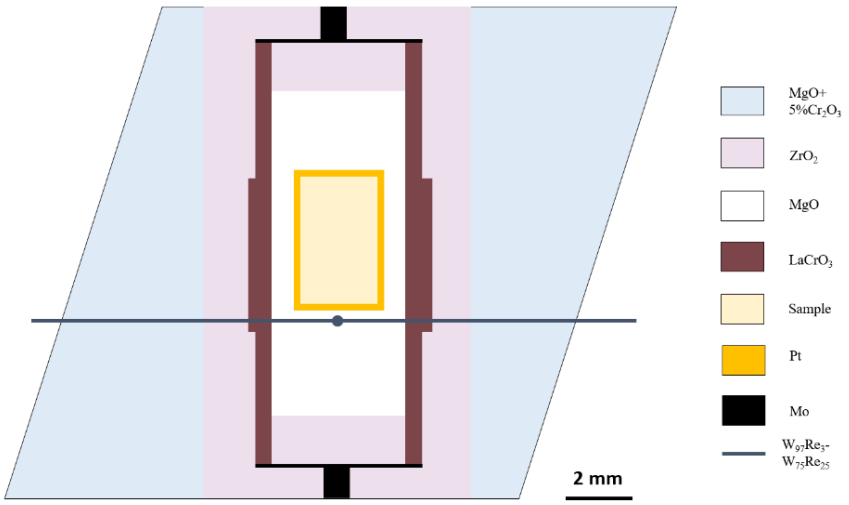

Fig. 3.1. Schematic drawing of cell assemblies for synthesis of stishovite single crystals.

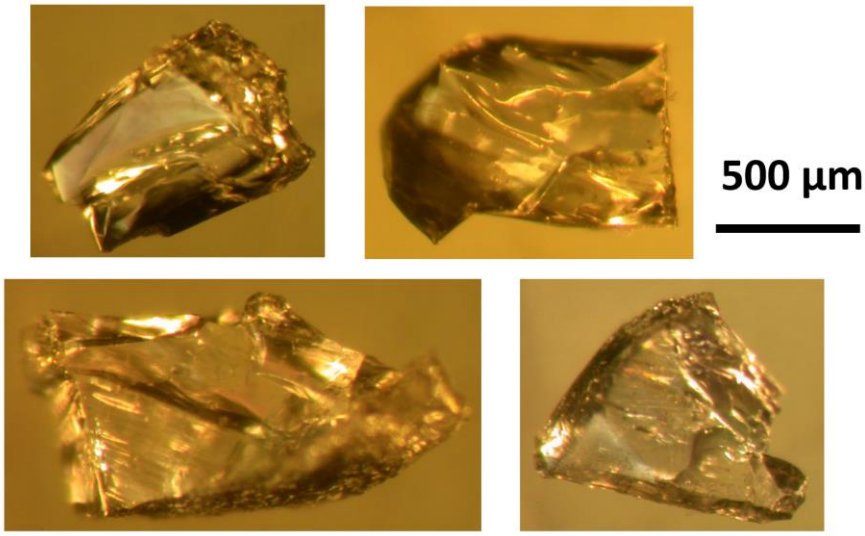

Fig. 3.2. Gallery of synthesized stishovite single crystals.

The stishovite single crystals were oriented to the <110> or the [001] directions by a precession X-ray camera with an acceleration voltage of 40 kV and current of 30 mA installed at the Institute for Planetary Materials, Okayama University. Crystal was exposed to white X-ray produced by Cu target for 5 min. When the imaging plate exercises conical oscillating between -20° to 20°, single crystal diffracts X-ray with continuous variation of incident orientation and thus products representative diffraction patterns on the imaging plate. By adjusting orientation of crystals from three dimensions, we could obtain typical diffraction patterns from the target orientation of stishovite. Fig. 3.3a illustrates X-ray diffraction patterns of stishovite single crystal with <110> direction. The crystal was thus fixed in the epoxy with oriented typical direction and surfaces perpendicular to the oriented directions were finally polished by the diamond paste with 0.25 µm grain size until all the scratches were removed (Fig. 3.3b).

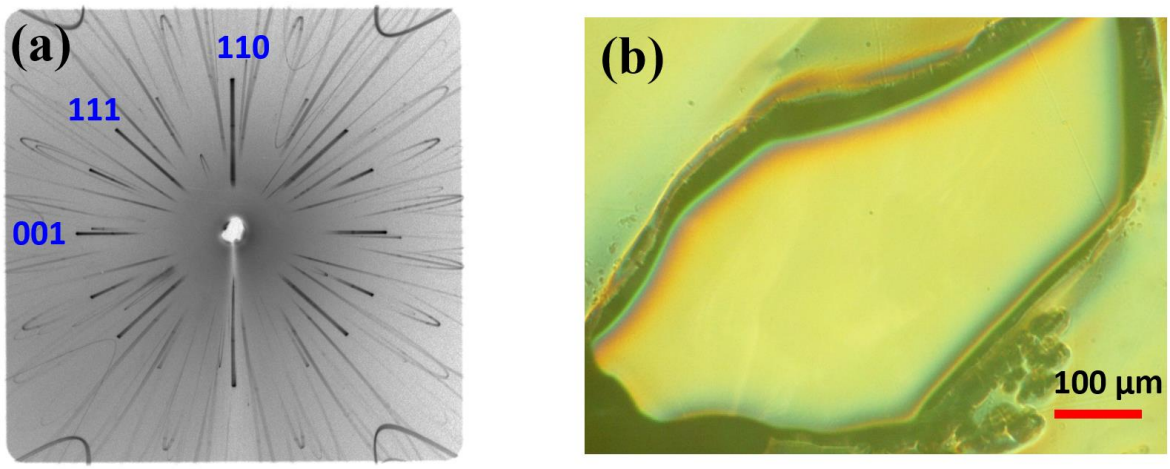

Fig. 3.3. Typical X-ray diffraction image of stishovite with the <110> orientation (a) and the image of surface after fine polishing (b).

In the diffusion experiments, we used ^{18}O and ^{29}Si as tracers. At first, we obtained the ^{18}O enriched quartz powder by reacting reagent-grade SiO_2 with natural isotopic abundance with ^{18}O enriched H_2O at 1 GPa and 1273 K for 40 hours in a piston cylinder apparatus. Then, the ^{18}O enriched quartz was mixed with ^{29}Si enriched SiO_2 to prepare SiO_2 powder enriched in both ^{29}Si and ^{18}O. The polished surfaces of stishovite crystals were coated with the SiO_2 enriched in both ^{29}Si and ^{18}O using the high vacuum thermal evaporation method (Fig. 3.4) (Schwandt et al., 1993). The stishovite crystals were placed in an inverted position with ^{29}Si and ^{18}O enriched SiO_2 source, which was loaded in a tungsten crucible. The isotope source sublines uniformly upon heat in the vacuum chamber. Thickness and isotopic composition of the deposited film on the stishovite crystal was determined by depth-profiling method using the secondary ion mass spectrometer (SIMS) to be ~150 nm and $^{29}Si/(^{28}Si+^{29}Si+^{30}Si)$ = 0.26, $^{18}O/(^{16}O+^{18}O)$ = 0.22, respectively (see later in detail).

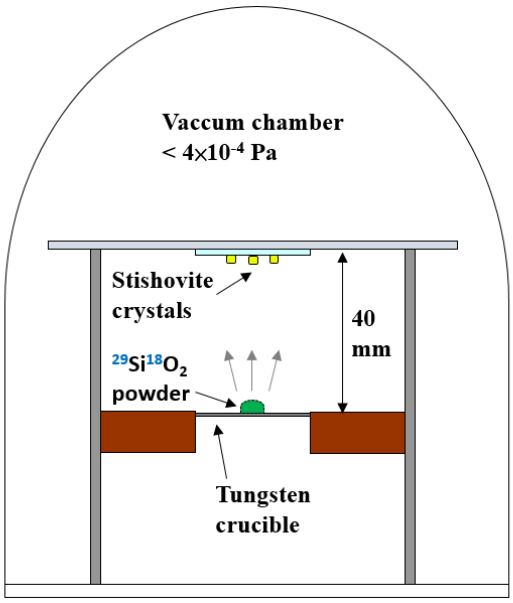

Fig. 3.4. Schematic showing of the high vacuum thermal evaporation method.

3.2.2. Diffusion experiments

Diffusion experiments at high pressure and high temperature were also conducted in the Kawai-type multianvil apparatus. In order to determine the pressure and temperature dependence on Si and O self-diffusion, the experiments were conducted at pressures of 14, 15, 18 and 21.5 GPa and at temperatures of 1673, 1873 and 2073 K. In the experiments at pressures lower (higher) than 20 GPa, MgO+5 %Cr_2O_3 octahedra with a 14 mm (10 mm) edge length and WC cubes with a 6 mm (5 mm) truncated edge length were used. Pressure calibration was done at 1873 K by detecting the forsterite-wadsleyite-ringwoodite transitions in Mg_2SiO_4 at 15.3 GPa and 21.3 GPa (Katsura et al., 2004; Suzuki et al., 2000) and coesite-stishovite transition in SiO_2 at 9.9 GPa (Zhang et al., 1996). Schematic view of the cell assemblies is shown in Fig. 3.5. High temperature was generated using a tubular $LaCrO_3$ furnace and was monitored with a $W_{97}Re_3$-$W_{75}Re_{25}$ thermocouple whose junction was set at

the position symmetrical to the sample capsule with respect to the center of furnace. The stishovite crystals with and without isotope coating were embedded in CsCl powder to reduce deviatoric stress in annealing at high pressures. The whole octahedral assembly was kept at 473 K in a vacuum oven for 12 hours to minimize the water absorbed in CsCl immediately before the experiment. The assembly was first compressed to the prescribed pressure and then heated to the target temperature with a rising rate of ~100 K/min. The temperature was automatically kept at the set value within fluctuation of ±2 K during diffusion annealing.

In order to monitor change in water content during annealing experiment, in some runs, a crystal without isotope coating was also put in the CsCl capsule (Fig. 3.5). The crystal was oriented to the <110> direction and two surfaces normal to the direction were polished for the Fourier transformed infrared spectroscopy (FTIR) measurement both before and after

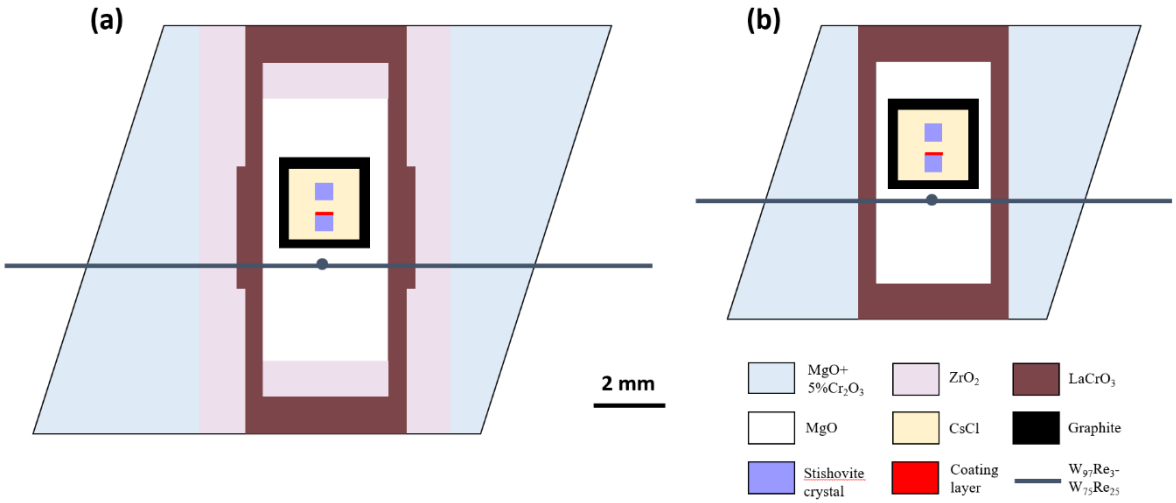

Fig. 3.5. Schematic drawing of cell assemblies for high pressure diffusion experiments. Assemblies (a) and (b) were adopted in the experiments at pressures lower and higher than 20 GPa, respectively. Stishovite crystals with and without isotope coating were loaded in the CsCl capsule for SIMS and FTIR measurement, respectively.

annealing experiment. Infrared absorption spectrum was obtained using a Jasco FTIR-6200 Fourier-transform spectrometer. The unpolarized IR light was aimed at 30 × 30 μm on the sample surface by a Jasco IRT-7000 microscope. The water content was calculated from absorption spectrum based on the calibration given by Paterson et al. (1982) as,

$$C_{\mathrm{OH}} = \frac{1}{150}\int \frac{K_v}{\gamma(3780-v)}\,\mathrm{d}v \qquad (3.1)$$

where C_{OH} is the molar concentration of incorporated H_2O, K_ν is the absorption coefficient, v is the wave number, γ is the anisotropy factor (fixed to 1/4 in the present study). Previous studies on stishovite using polarized infrared light indicated that the absorption by OH stretching is strongly pelochroic, and all the OH dipoles orient perpendicularly to the [001] direction (Pawley et al., 1993; Litasov et al., 2007). By applying the anisotropy factor γ=1/4, measurement along the <110> direction using unpolarized beam gives the water content of stishovite single crystal (Paterson et al., 1982).

Si and O penetration profiles were obtained concurrently by the depth-profiling method using the SIMS (Camera ims-6f) installed at Hokkaido University. Primary beam of Cs^+ focused to a 20 μm diameter spot was sputtered to the sample surface and rastered over an area of 150×150 μm to form a crater with a depth of several hundred nm along the diffusion direction. In order to minimize the crater edge effect, secondary ion intensities were collected only from the central 75×75 μm area of the sputtered crater as a function of sputtering time. Sequentially, the depth of the sputtered crater was measured by 3D laser scanning confocal microscope with a precision of 0.5 nm (VK-X250, KEYENCE Corp., Japan) installed at Hokkaido University. The time data of secondary ion intensity profile was converted to the

depth data by assuming a constant sputtering rate. To appraise the uncertainty, a few profiles were obtained for each sample.

In order to evaluate the convolution effect of SIMS measurement on determination of diffusivity, a pre-diffusion experiment (or a "zero time run") was conducted at 15 GPa. In this run, sample was immediately quenched by shutting off the electric power when temperature reached 1773 K. The obtained penetration profiles of the "zero time run" for Si and O were fitted to the double error function as

$$C(x) = C_0 + \frac{C_1 - C_0}{2}\left(erf\frac{h-x}{\sqrt{L_C^2}} + erf\frac{h+x}{\sqrt{L_C^2}}\right) \qquad (3.2)$$

where $C(x)$ denotes the concentration of ^{29}Si or ^{18}O at depth x from the surface, expressed as $^{29}Si/(^{28}Si+^{29}Si+^{30}Si)$ or $^{18}O/(^{16}O+^{18}O)$, respectively. C_1 and C_0 are the initial ^{29}Si or ^{18}O concentrations in the isotopic film and in the stishovite crystal, respectively. h is the thickness of deposited film and L_C is the nominal diffusion length of the "zero time run". L_C provides an evaluation of the spatial resolution of measurement, which denotes the broadening of the measured profile originated from the convolution effect (Ganguly et al., 1988). The Si and O diffusion coefficients (D_{Si} and D_O) were obtained by fitting the penetration profiles for each element to the double error function with correction of L_C,

$$C(x,t) = C_0 + \frac{C_1 - C_0}{2}\left(erf\frac{h-x}{\sqrt{4Dt+L_C^2}} + erf\frac{h+x}{\sqrt{4Dt+L_C^2}}\right) \qquad (3.3)$$

where t is the annealing duration (Crank, 1975).

3.3. Results

Typical FTIR spectra of the stishovite both before and after the annealing experiments are shown in Fig. 3.6 after a background correction and thickness normalization to 1 cm. The absorption peaks located at 3351, 3311, 3240, 3111 and 2667cm^{-1} coincide with those observed in the previous studies (Pawley et al., 1993; Litasov et al., 2007). Except for run 1K2155, absorption intensities of the spectra were almost identical before and after the run, indicating that the water content did not change during the annealing. Based on Eq. (3.1), we calculated the water contents in the monitored runs and listed them in Table 3.1. All the samples show the similar water contents before and after diffusion, with an average of 19±4 ppm (comparable to ~16-30 wt. ppm by Litasov et al., 2007). However, in run 1K2155, clear stishovite absorption peaks were superimposed on broad absorption spectra. Under the optical microscope, the recovered crystal was found to be turbid, indicating presence of submicroscopic fluid inclusions, which is consistent with the broad absorption background in the infrared spectrum (Keppler and Rauch, 2000). The formation of fluid inclusions indicates that the sample was in more hydrous circumstances than in others during sample preparation.

Measured penetration profiles of Si and O of the "zero time run" are shown in Fig. 3.7. The O penetration profile shows O isotope depletion near the surface (less than 50 nm), which is probably resulted from O isotopic exchange between the sample and the surroundings, although the experiment was quenched immediately just after temperature reached 1773 K. By fitting the profiles to Eq. (2), L_C were determined to be 14.2±0.5 nm and 11.1±0.4 nm for

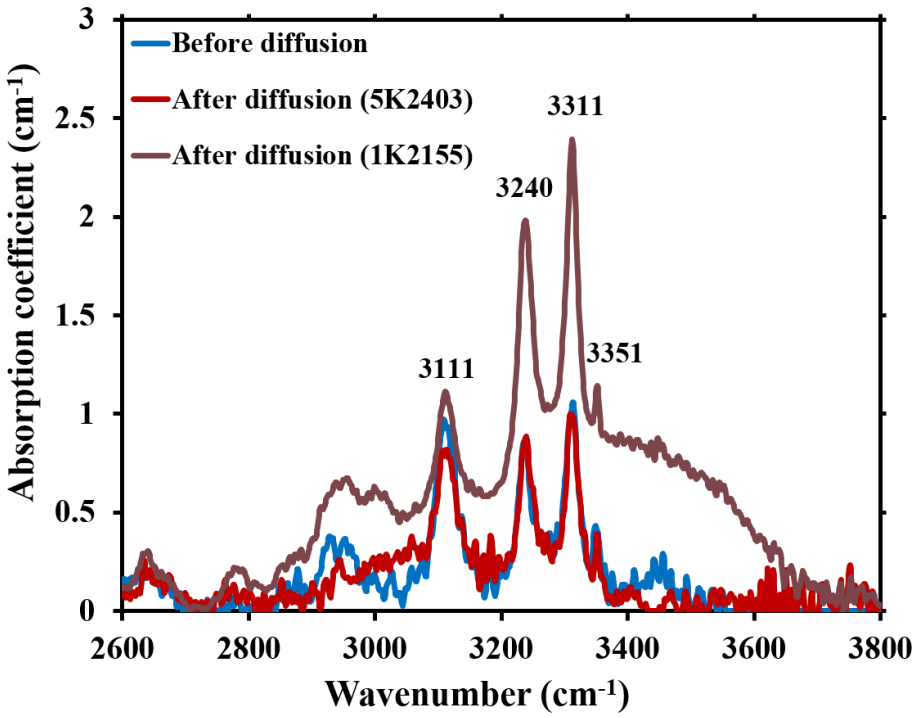

Fig. 3.6. Typical FTIR spectra of stishovite crystals before and after annealing experiments (runs 5K2403, 1K2215) after a background correction. A beam of unpolarized light was aimed to the crystal surface along the <110> direction. In run 5K2403, absorption spectra indicate no changes in water content in the crystal during the annealing. Spectra of 1K2155 displays to contain abnormally large amount of water (see text for detail).

Si and O, respectively. The L_C are comparable to the roughness of "zero time run" (~10 nm) and annealed samples (~15 nm) (Fig. 3.8). The convolution effect is mainly caused by the roughness of sample surface. Since the L_C values are much smaller than the real diffusion lengths ($4Dt >> L_C^2$) in this study (typically the real diffusion lengths are tens to hundreds of nanometer as described below), the uncertainties of diffusion coefficients caused by SIMS convolution effects were thus small in comparison with other Si and O self-diffusion studies in silicate minerals (e.g., Shimojuku et al., 2009; Fei et al., 2012, 2014).

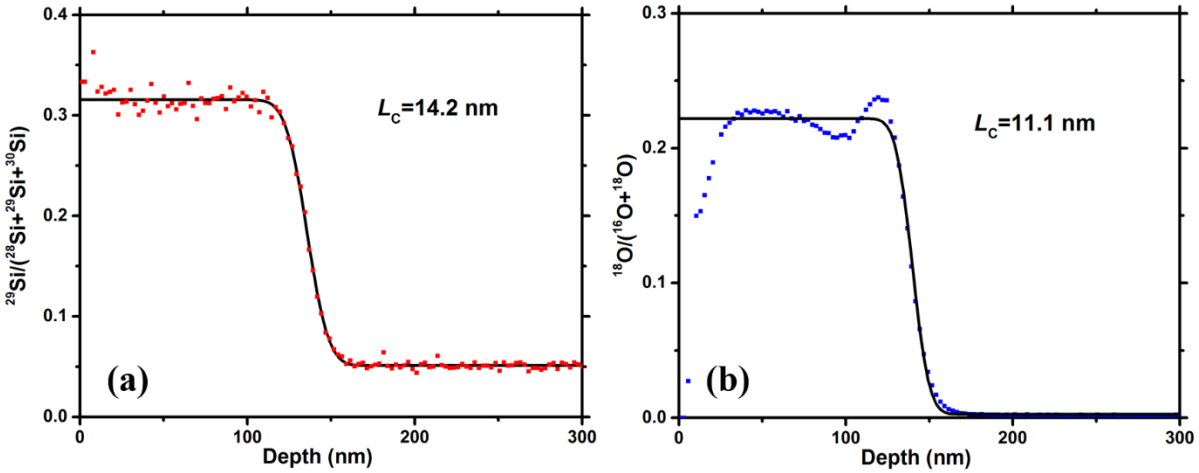

Fig. 3.7. Penetration profiles of Si and O of the "zero-time run" obtained by SIMS measurement. The depth "0 nm" corresponds to the surface of the recovered sample. The solid lines show results of numerical fitting of the profiles to Eq. (2.2). L_C is the nominal diffusion lengths deduced from fitting (see text for detail).

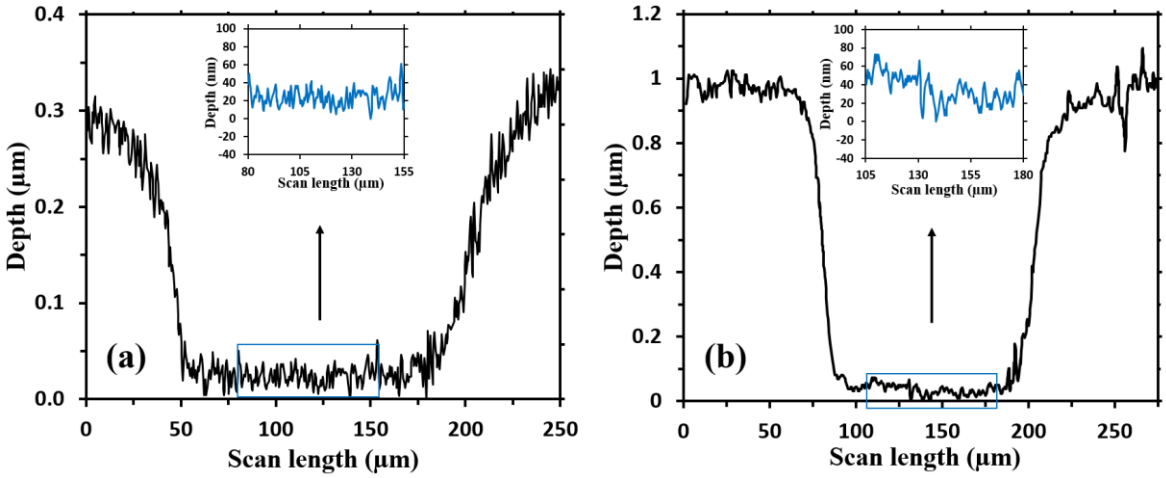

Fig. 3.8. Typical topographic profiles of crater after SIMS depth-profiling measurement obtained by using 3D laser scanning confocal microscope. The sample is stishovite of "zero time run" (a) and annealed at 21.5 GPa and 2073 K for 48 hours (b) (run 5K2506). Insert figures are the central 75×75 μm bottom of crater from which secondary ion was detected by SIMS.

Fig. 3.9 shows the typical penetration profiles of Si and O for the sample annealed at 21.5 GPa and 2073 K for 48 hours (run 5K2506). The diffusion coefficients were obtained by fitting the penetration profiles to Eq. (3). The apparent diffusion lengths for Si and O were 30-105 nm and 138-309 nm, respectively, both of which were much larger than the L_C values. Isotope ratio of O was largely reduced (by more than 1 order of magnitude) by annealing in comparison with the "zero time run", ~90 % depletion of total O isotope concentration based on the SIMS profiles of "zero time run" and annealing experiments. This would be also caused by isotope exchange of O between the samples and the surroundings, as had been noted in the previous studies (Dobson et al., 2008; Costa and Chakraborty, 2008). Since this exchange reaction is extremely rapid and brings uniform reduction of O isotope ratio over all the crystal, the obtained O diffusion coefficients were not affected by the O isotopic exchange.

Results of Si and O diffusion in stishovite obtained in the present study are summarized

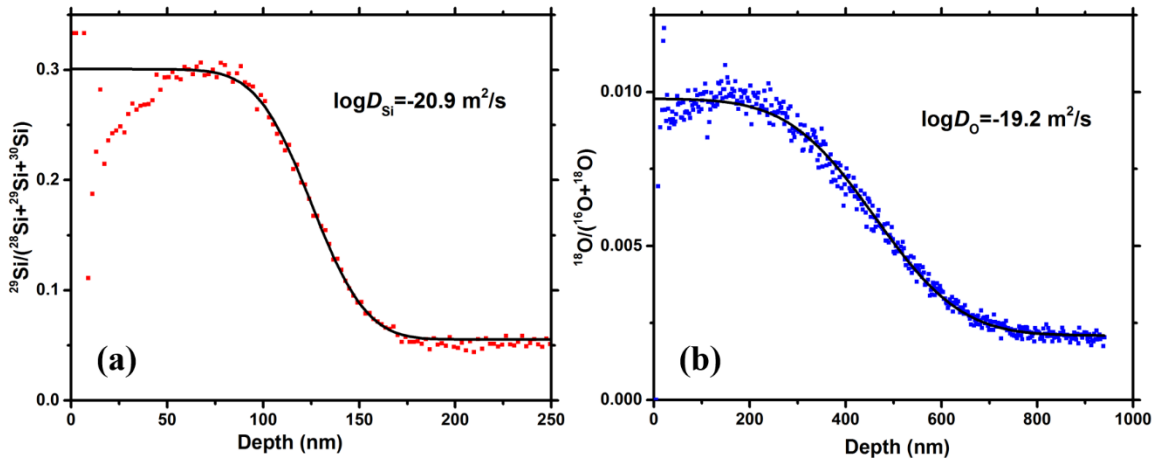

Fig. 3.9. Typical penetration profiles for Si (a) and O (b) after the annealing experiment. The solid lines show fitting of the profiles to Eq. (2.3). The experiment condition was at 21.5 GPa and 2073 K for 48 hours (run 5K2506).

in Table 3.1 together with the experimental conditions and are plotted against pressure in Fig. 3.10. Uncertainties of the diffusion coefficients given in Table 3.1 were mainly originated from those of measurements of crater depths. We deduced the uncertainties of diffusion coefficients by repeating SIMS measurements and crater depths determination few times. The diffusion coefficients presented in Table 3.1 are the arithmetic average of results obtained from different SIMS measurements on one sample. As shown in Fig. 3.11, the square of characteristic diffusion length expressed by $4Dt+L_C^2$ shows linear relationship with increasing annealing time. We used results from "zero time run" and annealing experiments at 14 and 15 GPa because of the pressure effect is negligible small with 1 GPa. The linearity indicates good consistency in obtained diffusivities between runs at same temperature and similar pressure. The Si diffusion coefficient plotted at 14 GPa and 1673 K (run 1K2155) seems to be anomalous compared with others. This feature could be due to the hydrous condition during the annealing in accord with the high and broad absorption band in FTIR spectra in Fig. 2.6 and turbid nature of the recovered crystal. Therefore, the run was excluded from analysis to obtain pressure and temperature effects on diffusion coefficients.

Pressure and temperature dependence of diffusion coefficient D can be assessed by the Arrhenius equation,

$$D = D_0 \exp\left(-\frac{\Delta E + P\Delta V}{RT}\right) \qquad (3.4)$$

where D_0 is the pre-exponential factor, ΔE is the activation energy, P is pressure, ΔV is activation volume, R is the ideal gas constant and T is absolute temperature. Least-square fitting of the diffusion data along the <110> direction (Table 3.1) to Eq. (3.4) yields ΔE, ΔV,

and logD_0 for Si and O diffusions to be 237±65 kJ/mol, 6.0±1.0 cm^3/mol, -11.6±1.0 log(m^2/s), and 263±103 kJ/mol, 4.8±1.7 cm^3/mol, -10.1±3.0 log(m^2/s), respectively. The attached errors were derived from the propagation of the uncertainties of the diffusion coefficients and the errors associated with the least-squares fit to the Arrhenius equation. It should be noted that the error of activation energies may be underestimated because of the limited data for temperature dependence.

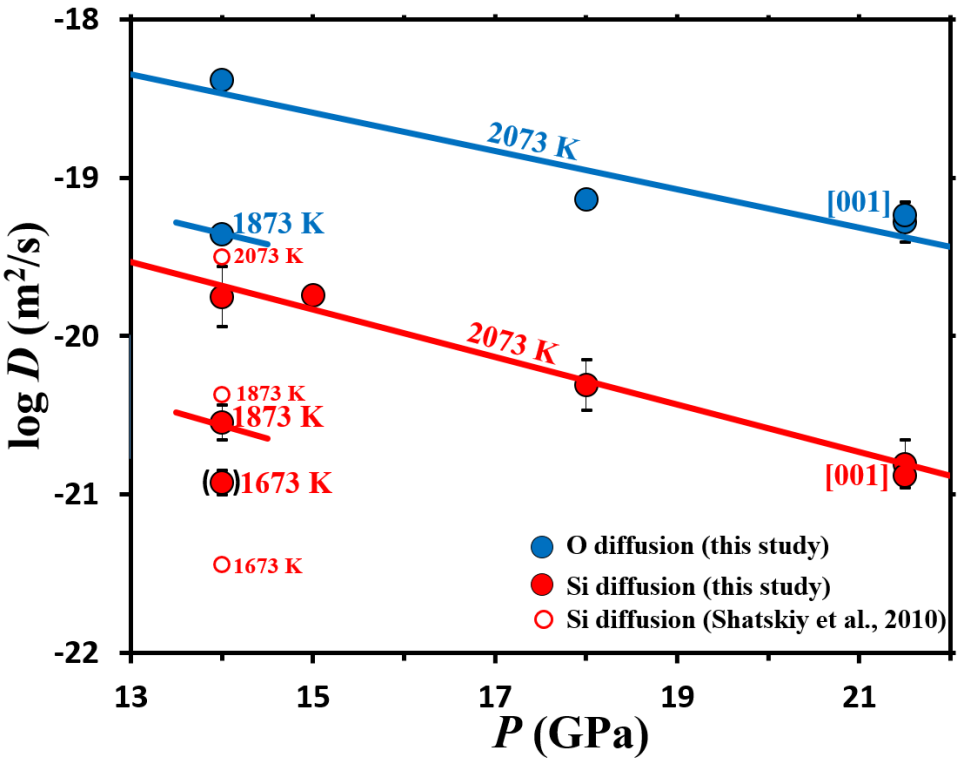

Fig. 3.10. Pressure dependence of Si and O diffusion coefficients in stishovite. All data plotted were obtained along the <110> direction, except for those labeled [001] which were deduced along the [001] direction. Solid lines show the results of least square fitting of all data along the <110> direction, except for datum in the parentheses (run 1K2155 at 14 GPa and 1673 K). Previous results by Shatskiy et al. (2010) at 14 GPa are also shown.

Table 3.1. Experimental conditions (pressure, temperature, duration, and crystallographic orientation) and the resultant Si and O diffusion coefficients in single crystal stishovite.

Run No.	P (GPa)	T (K)	direction	t (h)	Water content (wt.ppm) Before	After	$\log D_{Si}$ (m^2/s)	$\log D_O$ (m^2/s)
1K215*	14	1673	110	60	ND§	140 (30)	-20.9 (0.1)	ND
1K2126	14	1873	110	30	15 (1)	16 (4)	-20.5 (0.1)	-19.4 (0.1)
1K1802	14	2073	110	16	ND		-19.8 (0.2)	18.4 (0.1)
1K1799	15	2073	110	40	ND		-19.7(0.1)	ND
5K2403	18	2073	110	50	15 (1)	20 (7)	-20.3 (0.2)	-20.2 (0.1)
5K2404	21.5	2073	110	44	ND		-20.8 (0.2)	-19.3 (0.1)
5K2506	21.5	2073	001	48	23 (3)	22 (6)	-20.9 (0.1)	-19.2 (0.1)

Numbers in parentheses represented the uncertainties.

* Data was excluded for fitting (See text for detail).

§ Not determined.

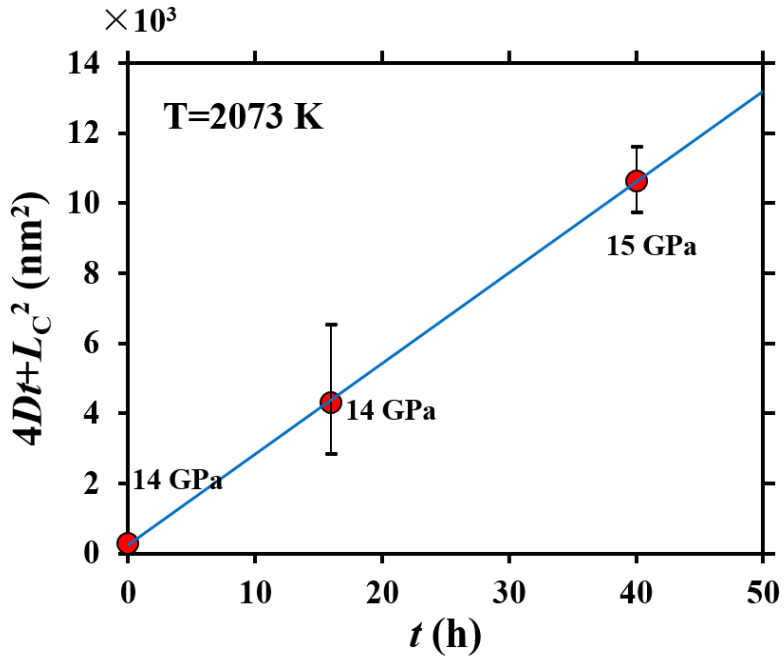

Fig. 3.11. Time dependence of $4Dt+L_C^2$ at 2073 K ("zero time run", runs 1K1802 and 1K1799).

3.4. Discussion

3.4.1 Si and O diffusion in stishovite

Our results indicate that the diffusion coefficients of both Si and O systematically decrease with pressure by 1-1.5 orders of magnitude from 14.0-21.5 GPa, and increase with temperature by nearly one order of magnitude from 1873-2073 K (Fig. 3.10). It is obvious that Si diffusion is approximately one order of magnitude slower than O diffusion. Therefore, Si is the rate-controlling element in plastic deformation of stishovite, as shown in many silcate mantle minerals such as forsterite (Fei et al., 2012), wadsleyite and ringwoodite (Shimojuku et al., 2009) and pyrope garnet (Shimojuku et al., 2013). The Si diffusion in stishovite obtained in the present study is slightly slower than the result obtained by Shatskiy et al. (2010) (less them 0.3 log unit), although the activation enthalpies are comparable between two studies. This discrepancy in diffusivity may be caused by that the convolution effect was not taken into account in their study, in which the convolution effect is expected to be larger because smaller crater size (~50×50 μm) yields larger edge effect.

Stishovite assumes the rutile structure (space group: *P4/mnm*) which constrains the equivalent diffusion flow on the (001) plane, leading to the identical diffusivity along the <100> and the <110> directions. Our diffusion experiments were mainly conducted along the <110> direction. It should be remarked that diffusivity along the [001] direction measured at 21.5 GPa, 2073 K is almost identical to that along the <110> direction (see table 3.1). The feature is consistent with Shatskiy et al. (2010). Thus, it is concluded that diffusivity of Si in stishovite is almost isotropic and hence the viscosity of stishovite can be assessed from the

Si diffusion coefficient along the <110> direction.

Using Eq. (3.4), Si and O diffusivities in stishovite are compared with those in other minerals in Fig. 3.12a and b by plotting them against temperature and pressure, respectively. As shown in Fig. 3.12a, Si and O diffusion in stishovite are slower than bridgmanite and quartz. Si in stishovite is six-fold coordinated with respect to O as Si in bridgmanite. Although large uncertainty in activation energy obtained in this study because of the limited range of temperature, the estimated activation enthalpy of Si diffusion in stishovite is similar to that of bridgmanite at 25 GPa, i.e., 387±90 kJ/mol for the former (this study) and 347±73 kJ/mol for the later (Dobson et al., 2008), both being smaller than quartz at room pressure (445±26 kJ/mol, Cherniak, 2003). O diffusivity is larger than Si diffusivity in both stishovite and bridgmanite, whereas vice versa in quartz (Dobson et al., 2008; Sharp et al., 1991). The estimated activation enthalpy of O diffusion in stishovite of 383±146 kJ/mol is different from that in bridgmanite of 501±80 kJ/mol at 25 GPa (Dobson et al., 2008), both being significant larger than 159±13 kJ/mol in quartz at room pressure (Sharp et al., 1991).

Fig. 3.12b shows comparison of Si diffusion coefficients of various silicates at 2073 K as functions of pressure. Due to the lack of the activation volume for wadsleyite and ringwoodite, that of forsterite (1.7±0.4 cm^3/mol, Fei et al., 2012) was substituted to calculate the pressure dependence of Si diffusion in these minerals. Pressure dependence of Si diffusion in bridgmanite was quoted from Yamazaki and Karato (2001). As shown in Fig. 3.12, stishovite has distinctly low Si diffusivity among the dominant mantle minerals, approximately 1-2 orders of magnitude lower than forsterite (Fei et al., 2012), 2-3 orders of

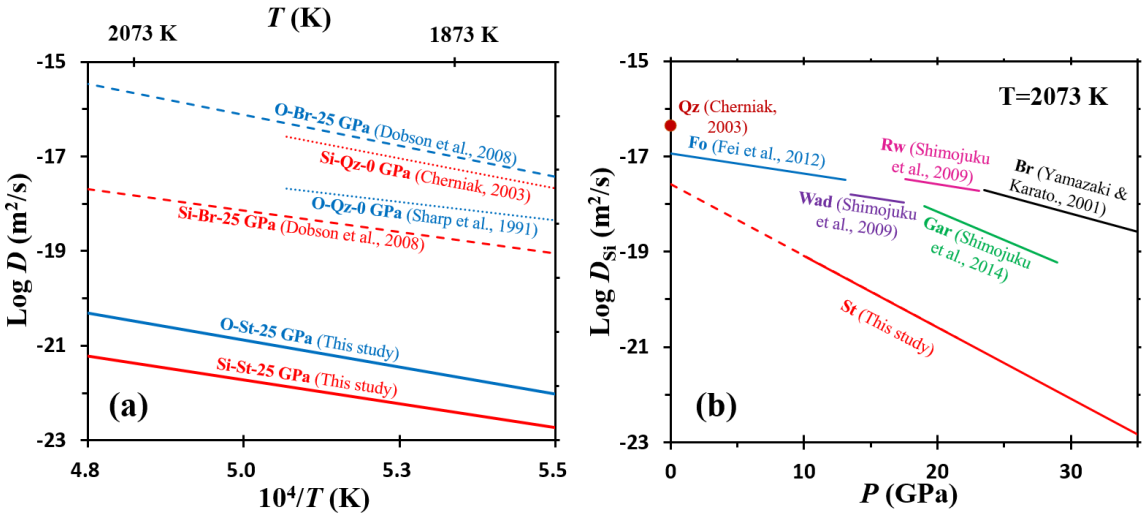

Fig. 3.12. Comparison of Si and O diffusivities in stishovite obtained in the present study with those in bridgmanite (Br: Dobson et al., 2008; Yamazaki and Karato, 2001), quartz (Qz: Cherniak, 2003; Sharp et al., 1991), forsterite (Fo: Fei et al., 2012), wadsleyite (Wad: Shimojuku et al., 2009), ringwoodite (Rw: Shimojuku et al., 2009) and garnet (Gar: Shimojuku et al., 2014). Temperature dependence at various pressures (a) and Si diffusivities in major minerals at 2073K as functions of pressure (b).

magnitude lower than wadsleyite (Shimojuku et al., 2009) and garnet (Shimojuku et al., 2014), and three orders or more lower than ringwoodite (Shimojuku et al., 2009) and bridgmanite (Yamazaki and Karato, 2001).

3.4.2. Implications for stability of seismic reflector in the mid-mantle

Plastic flow by diffusion and dislocation climb is controlled by the atomic diffusion of species with the lowest diffusivity (Nabarro, 1948; Herring, 1950; Weertman, 1968). Assuming that the viscosity is inversely proportional to diffusion coefficient of the slowest element (Nabarro, 1948; Weertman, 1999), the viscosity of stishovite is estimated to be 2 to

4 orders of magnitude larger than those of other dominant mantle minerals. Stishovite has a larger activation volume (6.0±1.0 cm^3/mol, the present study) than bridgmanite (3.0 cm^3/mol, Yamazaki and Karato, 2001), leading to an increase in viscosity contrast between the both minerals with pressure. Stishovite would significantly harden the SiO_2-rich fragments in the lower mantle, because of the distinctly higher viscosity compared with the surrounding mantle which is dominated by bridgmanite.

According to Manga's (1996) simulation, chemically distinct fragments can persist in the lower mantle over the course of Earth history if it is two orders of magnitude more viscous than the surrounding mantle. Bridgmanite is the dominant phase in the surrounding lower mantle (>70 vol.% (e.g. Ringwood, 1991)), and hence the viscosity is considered to be mainly controlled by bridgmantie (e.g. Yoshino et al., 2008) although secondary phase of ferro-periclase may reduce the viscosity with large strain (Girard et al., 2016). Although the fragments contain other phases (e.g. Ca-perovskite, $NaAlSiO_4$-rich calcium ferrite, $KALSiO_3$-rich hollandite and Na-Al-phase) (Ono et al., 2001; Ishii et al., 2012; Komabayashi et al., 2009), it is highly likely that stishovite is the hardest mineral in the fragments. Therefore, the proportion of stishovite is a key for mixing up of fragments with the surrounding mantle. With simple assumption that the fragments are composed of stishovite plus bridgmanite and the surrounding lower mantle is solely composed of bridgmanite, we calculated the viscosity contrast between the fragments and the surrounding lower mantle at 1000 km depth (40 GPa, 2073 K) as a function of proportion of stishovite. We adopted Si diffusivity of stishovite and its pressure dependence obtained in the present study. As the similar low diffusivity of Mg to Si in bridgmanite (Xu et al., 2011), the effective diffusivity

($\frac{1}{D_{eff}} = \frac{1}{D_{Si}} + \frac{1}{D_{Mg}}$) was taken into account to control the viscosity of bridgmanite (Jaoul et al., 1990). In a multi-phase composite, the bulk viscosity depend on the geometry of constituent components (Handy, 1994) as well. We first calculated the relative viscosity using Taylor and Sachs averages as the extreme bounds, and then their Hill's arithmetic and geometric averages were figured out (Hill, 1952). The results are shown in Fig. 3.9, in which viscosity ratios of the composite to bridgmanite in logarithmic scale are illustrated against the stishovite proportion, together with those of MORB (Ono et al., 2001), CC (Ishii et al., 2012) and TTG (Komabayashi et al., 2009). The horizontal line at *log2* is drawn to indicate a critical viscosity contrast required for preservation of the SiO_2-rich fragments for long time (Manga, 1996).

As shown in Fig. 3.13, the presence of stishovite even in a small proportion can significantly harden the composite in both Taylor average and Hill's averages (Hill's arithmetic and geometric averages), e.g. a few volume percent of stishovite makes the composite be more than one order of magnitude viscous than bridgmanite. The viscosity ratio increase with increasing volume fraction of stishovite. When the stishovite reaches ~ 30 vol.%, the viscosity ratio calculated from Hill's geometric average turn to be larger than two orders of magnitude, it's ~3.5 orders of magnitude from Taylor and Hill's arithmetic average. It indicates that SiO_2-rich fragments (originating from MORB, CC and TTG) are capable of being preserved as the observed seismic reflectors (Kaneshima and Helffrich, 1999, 2003; Castle and Creager, 1999; Niu et al., 2003) for long term in the mid-mantle depth. If the bulk viscosity is controlled by the Sachs average, however, no bulk rock among these three

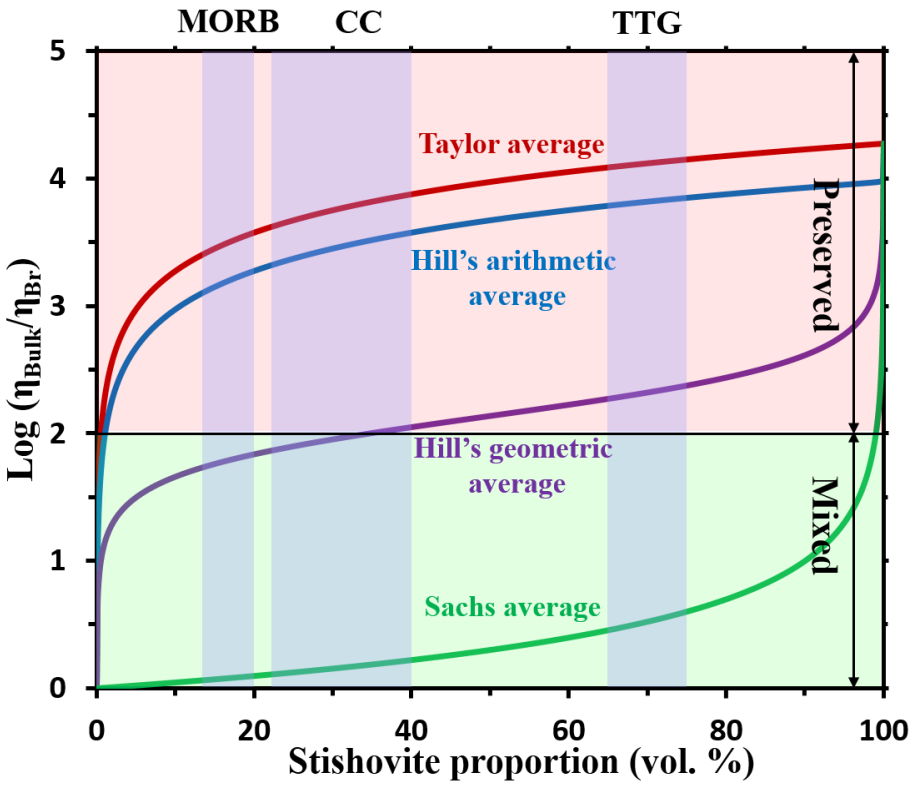

Fig. 3.13. Viscosity contrast between a composite of stishovite plus bridgmanite (bulk viscosity, η_{bulk}) and bridgmanite (η_{Br}) as functions of stishovite volume fraction at 2073 K, 40 GPa, corresponding to the temperature and pressure conditions at 1000 km depth. η_{Bulk} was calculated based on Taylor and Sachs averages and their arithmetic and geometric means (Hill's average, Hill, 1952). The ranges of viscosity contrast for preservation (pink region) or mixing up (green region) of a composite is divided by the horizontal line drawing at *log2* following Manga (1996). Proportional ranges of stishovite in MORB (Ono et al., 2001), CC (Ishii et al., 2012) and TTG (Komabayashi et al., 2010) are marked by blue color.

compositions can be preserved.

However, as mentioned above, we should note that the composition of fragments and surrounding lower mantle are more complicated than the present assumption of stishovite

plus perovskite. In future, more studies on the viscosity of other minerals of the lower mantle (e.g. Ca-perovskite, $NaAlSiO_4$-rich calcium ferrite, $KALSiO_3$-rich hollandite and Na-Al-phase) (Ono et al., 2001; Ishii et al., 2012; Komabayashi et al., 2009) may lead us to better constraints. In addition, more realistic modeling of multi-phase viscosity rather than Taylor, Sachs and Hill's average is required because of significant dependency of the viscosity on the multi-phase geometry (Handy, 1994).

3.5. Summary

1) Si and O self-diffusion in stishovite was studied simultaneously by means of the isotopic tracer method adopting single crystals. Annealing experiments were carried out up to 21.5 GPa and 2073 K in the Kawai-type multianvil apparatus. Penetration profiles of the run products were obtained by the SIMS method to derive the diffusion coefficients.

2) Present experiments demonstrate that Si diffusion in stishovite is distinctly slow compared with other mantle minerals. O diffusion in stishovite is more than one order of magnitude faster than Si and, therefore, Si diffusion controls the plastic deformation of stishovite.

3) Experiments over wide ranges of pressure made it possible to determine the activation volumes of both Si and O diffusion. Thus, diffusivities can be extrapolated to deeper mantle conditions.

4) Assuming the inverse relationship between viscosity and diffusivity of Si, stishovite is judged to be by far harder than other mantle minerals. It is likely that stishovite is ~4 orders of magnitude harder than bridgmanite at 1000 km depth.

5) Viscosity assessment for a composite of stishovite and bridgmanite supports that stishovite is capable to stabilize the seismic reflectors originated from MORB, CC and TTG subducted to the mid-mantle.

Reference

Carpenter, M. A., Hemley, R. J., Mao, H. K., 2000. High-pressure elasticity of stishovite and the P42/mnm⇔ Pnnm phase transition. J. Geophys. Res, 105, 10807-10816.

Castle, J. C., Creager, K. C., 1999. A steeply dipping discontinuity in the lower mantle beneath Izu‐Bonin. J. Geophys. Res: 104, 7279-7292.

Cherniak, D. J., 2003. Silicon self-diffusion in single-crystal natural quartz and feldspar. Earth Planet. Sci. Lett., 214, 655-668.

Costa, F., Chakraborty, S., 2008. The effect of water on Si and O diffusion rates in olivine and implications for transport properties and processes in the upper mantle. Phys. Earth Planet. Inter., 166, 11-29.

Crank, J., 1979. The mathematics of diffusion. Oxford university press.

Dobson, D. P., Dohmen, R., Wiedenbeck, M., 2008. Self-diffusion of oxygen and silicon in $MgSiO_3$ perovskite. Earth Planet. Sci. Lett., 270, 125-129.

Fei, H., Hegoda, C., Yamazaki, D., Wiedenbeck, M., Yurimoto, H., Shcheka, S., Katsura, T., 2012. High silicon self-diffusion coefficient in dry forsterite. Earth Planet. Sci. Lett., 345, 95-103.

Fei, H., Wiedenbeck, M., Yamazaki, D., Katsura, T., 2014. No effect of water on oxygen self‐diffusion rate in forsterite. J. Geophys. Res., 119, 7598–7606.

Frost, H. J., Ashby, M. F., 1982. Deformation mechanism maps: the plasticity and creep of metals and ceramics. Pergamon Press, Oxford, UK.

Ganguly, J., Bhattacharya, R.N., Chakraborty, S., 1988. Convolution effect in the determination of compositional profiles and diffusion coefficients by microprobe step scan. Am. Miner., 73, 901–909.

Girard, J., Amulele, G., Farla, R., Mohiuddin, A., Karato, S. I., 2016. Shear deformation of bridgmanite and magnesiowüstite aggregates at lower mantle conditions. Science, 351, 144-147.

Handy, M. R., 1994. Flow laws for rocks containing two non-linear viscous phases: a phenomenological approach. J. Struct. Geol., 16, 287-301.

Herring, C., 1950. Diffusional viscosity of a polycrystalline solid. J. Appl. Phys., 21, 437-445.

Hill, R., 1952. The elastic behaviour of a crystalline aggregate. Proc. Phys. Soc., 65, 349.

Hirose, K., Takafuji, N., Sata, N., Ohishi, Y., 2005. Phase transition and density of subducted MORB crust in the lower mantle. Earth Planet. Sci. Lett., 237, 239-251.

Ishii, T., Kojitani, H., Akaogi, M., 2012. High-pressure phase transitions and subduction behavior of continental crust at pressure–temperature conditions up to the upper part of the lower mantle. Earth Planet. Sci. Lett., 357, 31-41.

Jaoul, O., Béjina, F., Élie, F., Abel, F., 1995. Silicon self-diffusion in quartz. Phys. Rev. Lett., 74, 2038.

Kaneshima, S., 2009. Seismic scatterers at the shallowest lower mantle beneath subducted slabs. Earth Planet. Sci. Lett., 286, 304-315.

Kaneshima. S, 2016. Seismic scatterers in the mid-lower mantle. Phys. Earth Planet. Inter., 257, pp. 105–114.

Kaneshima, S., Helffrich, G., 1999. Dipping low-velocity layer in the mid-lower mantle: evidence for geochemical heterogeneity. Science, 283, 1888-1892.

Kaneshima, S., Helffrich, G., 2003. Subparallel dipping heterogeneities in the mid‐lower mantle. J. Geophys. Res., 108, 2272.

Katsura, T., Yamada, H., Nishikawa, O., Song, M., Kubo, A., Shinmei, T., Yokoshi, S., Aizawa, Y., Yoshino, T., Walter, M. J., Ito, E., Funakoshi, K., 2004. Olivine‐wadsleyite transition in the system $(Mg,Fe)_2SiO_4$. J. Geophys. Res., 109, B02209.

Keppler, H., Rauch, M., 2000. Water solubility in nominally anhydrous minerals measured by FTIR and 1H MAS NMR: the effect of sample preparation. Phys. Chem. Miner., 27, 371-376.

Komabayashi, T., Maruyama, S., Rino, S., 2009. A speculation on the structure of the D” layer: The growth of anti-crust at the core-mantle boundary through the subduction history of the Earth. Gondwana Res., 15, 342-353.

Litasov, K. D., Kagi, H., Shatskiy, A., Ohtani, E., Lakshtanov, D. L., Bass, J. D., Ito, E., 2007. High hydrogen solubility in Al-rich stishovite and water transport in the lower mantle. Earth Planet. Sci. Lett., 262, 620-634.

Manga, M., 1996. Mixing of heterogeneities in the mantle: effect of viscosity differences. Geophys. Res. Lett., 23, 403-406.

Nabarro, F. R. N., 1948. Deformation of crystals by the motion of single ions. In Report of a Conference on Strength of Solids (pp. 75-90).

Niu, F., Kawakatsu, H., Fukao, Y., 2003. Seismic evidence for a chemical heterogeneity in the midmantle: a strong and slightly dipping seismic reflector beneath the Mariana subduction zone. J. Geophys. Res., 108, 2419.

Nomura, R., Hirose, K., Sata, N., & Ohishi, Y., 2010. Precise determination of post-stishovite phase transition boundary and implications for seismic heterogeneities in the mid-lower mantle. Phys. Earth Planet. Inter., 183, 104-109.

Ono, S., Ito, E., Katsura, T., 2001. Mineralogy of subducted basaltic crust (MORB) from 25 to 37 GPa, and chemical heterogeneity of the lower mantle. Earth Planet. Sci. Lett., 190, 57-63.

Paterson, M. S., 1982. The determination of hydroxyl by infrared absorption in quartz, silicate glasses, and similar materials. Bull. Miner., 105, 20-29.

Pawley, A. R., McMillan, P. F., Holloway, J. R. (1993). Hydrogen in stishovite, with implications for mantle water content. Science, 261, 1024-1024.

Sharp, Z. D., Giletti, B. J., Yoder, H. S., 1991. Oxygen diffusion rates in quartz exchanged with CO_2. Earth Planet. Sci. Lett., 107, 339-348.

Shatskiy, A., Yamazaki, D., Borzdov, Y. M., Matsuzaki, T., Litasov, K. D., Cooray, T., Ferot, A., Ito, E., Katsura, T., 2010. Stishovite single-crystal growth and application to silicon self-diffusion measurements. Am. Miner., 95(1), 135-143.

Shimojuku, A., Kubo, T., Kato, T., Yoshino, T., Nishi, M., Nakamura, T., Okazaki, R., Kakazu, Y., 2014) Effects of pressure and temperature on the silicon diffusivity of pyrope-rich garnet. Phys. Earth Planet. Inter., 226, 28-38.

Shimojuku, A., Kubo, T., Ohtani, E., Nakamura, T., Okazaki, R., Dohmen, R., Chakraborty, S., 2009. Si and O diffusion in $(Mg, Fe)_2$ SiO_4 wadsleyite and ringwoodite and its implications for the rheology of the mantle transition zone. Earth Planet. Sci. Lett., 284, 103-112.

Suzuki, A., Ohtani, E., Morishima, H., Kubo, T., Kanbe, Y., Kondo, T., Okada, T., Terasaki, H., Kato, T., Kikegawa, T., 2000. In situ determination of the phase boundary between wadsleyite and ringwoodite in Mg_2SiO_4. J. Geophys. Res., 27, 803-806.

Tsuchiya, T., 2011. Elasticity of subducted basaltic crust at the lower mantle pressures: Insights on the nature of deep mantle heterogeneity. Phys. Earth Planet. Inter., 188, 142-149.

Weertman, J., 1968. Dislocation climb theory of steady-state creep. Transactions of the American Society of Metals, 61, 681-694.

Weertman, J., 1999. Microstructural mechanisms of creep. Mechanics and materials: Fundamentals and linkages, 451-488.

Xu, J., Yamazaki, D., Katsura, T., Wu, X., Remmert, P., Yurimoto, H., Chakraborty, S., 2011. Silicon and magnesium diffusion in a single crystal of $MgSiO_3$ perovskite. J. Geophys. Res., 116.

Yamazaki, D., Karato, S. I., 2001. Some mineral physics constraints on the rheology and geothermal structure of Earth's lower mantle. Am. Miner., 86, 385-391.

Yoshino, T., Yamazaki, D., Ito, E., Katsura, T., 2008. No interconnection of ferro-periclase in post-spinel phase inferred from conductivity measurement. Geophys. Res. Lett., 35.

Zhang, J., Li, B., Utsumi, W., Liebermann, R. C., 1996. In situ X-ray observations of the coesite-stishovite transition: reversed phase boundary and kinetics. Phys. Chem. Miner., 23, 1-10.

Chapter 4. Technical development of deformation experiment under lower mantle conditions and application to the rheology of post-spinel and bridgmanite

Abstract

Seismic tomography has imaged slab stagnation at mid-mantle depth, which is coincident with the depth of proposed viscosity jump in lower mantle. However, the mineralogical mechanism to this increase in viscosity is still a mystery due to the absence of phase transition in main constituting minerals. A perovskitic lower mantle was reported consist of more than 93 vol.% bridgmanite whereas harzburgite layer in subducting slab contains ~20 vol.% of ferropericlase. Ferropericlase is likely much weaker than bridgmanite it may significantly reduce the bulk viscosity of bridgmanite and ferropericlase aggregate once interconnected structure was formed. Therefore, the chemical difference layer between the accumulated subducted harzburgite layer in the upper lower mantle and the underlying perovskitic lower mantle may be responsible to the viscosity jump at mid-mantle depth.

To study the viscosity contrast between single bridgmanite phase and bridgmanite and ferropericlase aggregate, deformation experiment was designed. However, the available experimental setup for deformation experiments under lower mantle conditions is still limited due to the experimental difficulty. We utilized both D-DIA multi-anvil press and DT-Cup with the Kawai-type cell assembly (6–8 type) in this study. *In-situ* deformation experiments has been done using D-DIA apparatus at BL04b1 at SPring-8, Japan. Although trying with different cell assemblies, little strain was obtained in the sample (<3%). It's difficult for us to obtain substantial strain with current design in D-DIA apparatus. Instead, DT-Cup has an advantage in deformation as the sample column line along the direction of movement of differential anvils. But the highest pressure was limited in ~ 19 GPa at room temperature.

With optimization of the experimental design, we firstly reached the lower mantle condition in DT-Cup apparatus. With preliminary result on uniaxial deformation experiment, the recovered samples show substantial deformation. This study demonstrates an approach of using DT-Cup to study the rheology of lower mantle minerals.

We applied the experimental design for deformation of bridgmanite and post-spinel two layer sample. Deformation experiments were conducted at 1500 ℃ up to strain of ~0.2. The recovered sample showed similar strain in bridgmanite and post-spinel sample, which suggested the bridgmanite dominate the bulk viscosity of post-spinel under current conditions. This indicates harzburgite unable to be responsible for the viscosity jump in the lower mantle, or because the strain is not large enough to induce the interconnectivity of ferropericlase.

4.1. Introduction

The Earth's lower mantle, which occupies ~65% of Earth's mantle, plays an important role for mantle dynamics. The convecting lower mantle involves plastic deformation of constituting minerals, hence understanding the plastic properties of lower mantle minerals is a key to access the dynamic process. The most direct approach of plastic property of minerals is deformation experiment with applying deviatoric stress and observation of resulted strain and structure. Although many studies have been done by numerical simulation (e.g. Madi et al., 2005) or deformation experiments of analog materials (e.g. Wang et al., 2013; Kaercher et al., 2016) on lower mantle minerals, deformation experiment under lower mantle conditions is still limited due to the experimental difficulties. The main challenge is the generation of pressure and temperature conditions corresponding to the Earth's lower mantle (P>25 GPa, T>1827 K). In order to move the differential rams, the differential piston and oil system have to support both the confining pressure and load needed for deformation, leads to a high requirement for apparatus. As the development of hard material and also designation of apparatus, significant breakthrough has been achieved over the last decades.

The diamond anvil cell is a powerful tool in generating extremely high pressures (e.g. Mao et al., 1998), and high temperature can be obtained with laser heating. Merkel et al. (2003) conducted deformation experiments of perovskite at room temperature using diamond anvil cell. However, due to the high stress by axial compression and limited temperature condition, it is insufficient to be applied to the mantle. Stress relaxation experiments at 25

Table 4.1. Characteristics of various apparatus for deformation of deep mantle minerals.

Apparatus		*P* (GPa)	*T* (K)	Note	Ref.
D-DIA*	MA6-6	< 18	<1700	Limited P&T region	(1)
	6-8 type	< 25	<1827	Limited strain	(2)
Rotational Drickamer		<27.5	<2150	Poor stress, strain resolution	(3)
DT-Cup		<18	<1727	Limited P	(4)
Multianvil press§		<25	2500	Non controlling deformation	(5)
Diamond anvil cell		<200	<1000	High stress, non-steady state	(6)

(1) Kawazoe et al., 2016; (2) Tsujino et al., 2016; (3) Girard et al., 2016; (4) Hunt et al., 2014; (5) Cordier et al., 2004; (6) Mao et al., 1998.

* Both MA6-6 and 6-8 type cell assemblies were used with D-DIA apparatus. See text for details.

§ Stress relaxation experiment.

GPa up to 2500 K were performed by Cordier et al. (2004). But as high stress was generated during compression, deformation at high temperature is out of controlling in strain and stress.

Recently, using rotational Drickamer apparatus (RDA), Girard et al. (2016) firstly successfully deformed ~70% bridgmanite +~30% ferropericlase aggregates under lower mantle conditions up to 100% strain. RDA is a modification of the Drickamer apparatus in which torsional deformation can be obtained by rotating the upper anvil relative to the lower one under high pressure and temperature (Fig. 4.1a) (Yamazaki and Karato, 2001). However, as widely notified, the heterogeneous distribution of strain across the sample will cause large uncertainties in determination of properties of the sample (Fig. 4.1b). Temperature was estimated from power-temperature relationship due to the breakage of thermocouple during shear deformation, which is the other source of uncertainty. Large uncertainties in temperature and strain lead difficulty to obtain quantitative measurement on the rheological

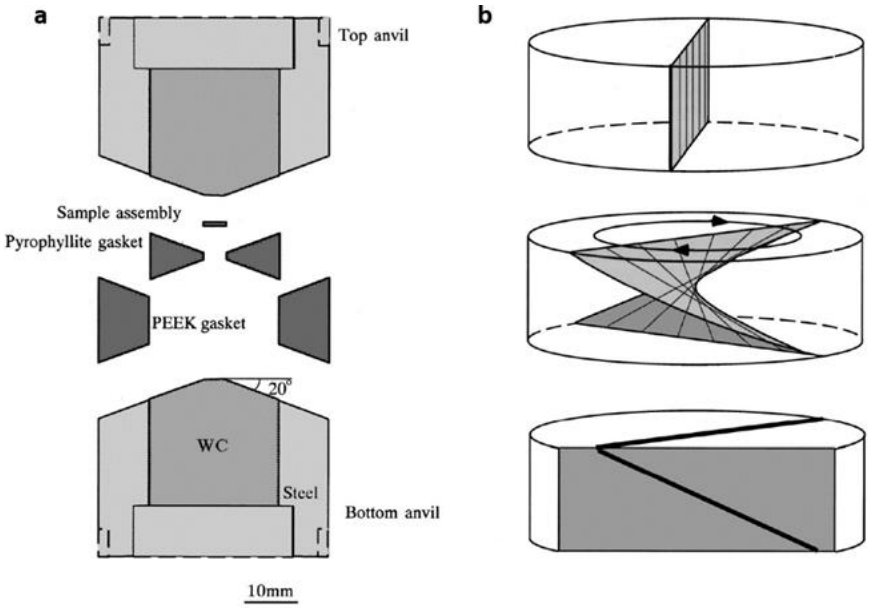

Fig. 4.1. Schematic drawing of set up of RDA (a) and rotation of strain maker during deformation (b) from Yamazaki and Karato (2001). Strain marker is shown in shaded plane in (b).

properties (Kawazoe et al., 2016). The viscosity data obtained from RDA show hardly consistent with those from D-DIA (Kawazoe et al., 2016), which may be caused by the large uncertainties of temperature and strain measurement.

As I mentioned in Chapter 2, a deformation-DIA (D-DIA) was developed based on the cubic-anvil apparatus known as the DIA by introducing two differential rams in the upper and lower guide blocks (Wang et al., 2003). It was widely used for deformation experiment of minerals, in particular in beamlines of synchrotron radiation facilities as the advantageous design with vertical anvils gaps in this cell, in upper mantle and transition zone (e.g. Ohuchi et al., 2015; Kawazoe et al., 2013, 2016). The Multi-anvil Assembly 6-6 (MA6-6) was

applied in the D-DIA apparatus most widely, except recently 6-8 type was also utilized (Tsujino et al., 2016). The MA6-6 type cell is consist of six tungsten carbide (WC) anvils with cubic pressure medium (Nishiyama et al., 2008) which were aligned with anvil guide (steel or Teflon). With improvement of the cell, recently viscosity of ringwoodite was studied under lower mantle transition zone condition with pressure mediums of 3.2 mm edge lengths and fine grained (Fujilloy TF05) WC anvils with 2.0 mm truncation (Kawazoe et al., 2016). But up to date, it is unavailable to conduct deformation experiments under the lower mantle conditions (>24 GPa) with MA6-6 type cell.

In the 6-8 type cell assembly, eight second-stage cubic anvils with a truncated corner compress an octahedral shape pressure medium to generate high pressure (Tsujino, 2012, Doctoral thesis). Due to compression from eight directions compared with six, better hydrostatic condition is expected in 6-8 type cell. It is expected that 6-8 type has potential to generate higher pressure compared with MA6-6 type. Tsujino et al. (2016) successfully deformed bridgmanite in steady state under lower mantle condition to understand the slip system. Furthermore, the volume of octahedral pressure medium used in Tsujino et al. (2016) is almost three times larger than that of cubic one in Kawazoe et al. (2016), which indicates a better pressure, temperature and differential stress conditions during deformation with 6-8 type cell assembly. However, no information about the viscosity was obtained from this recovered sample, in-situ deformation experiment or modified cell assembly is required to obtain more information on lower mantle rheology.

Recently, a new multi-anvil deformation apparatus, based on the widely used 6-8

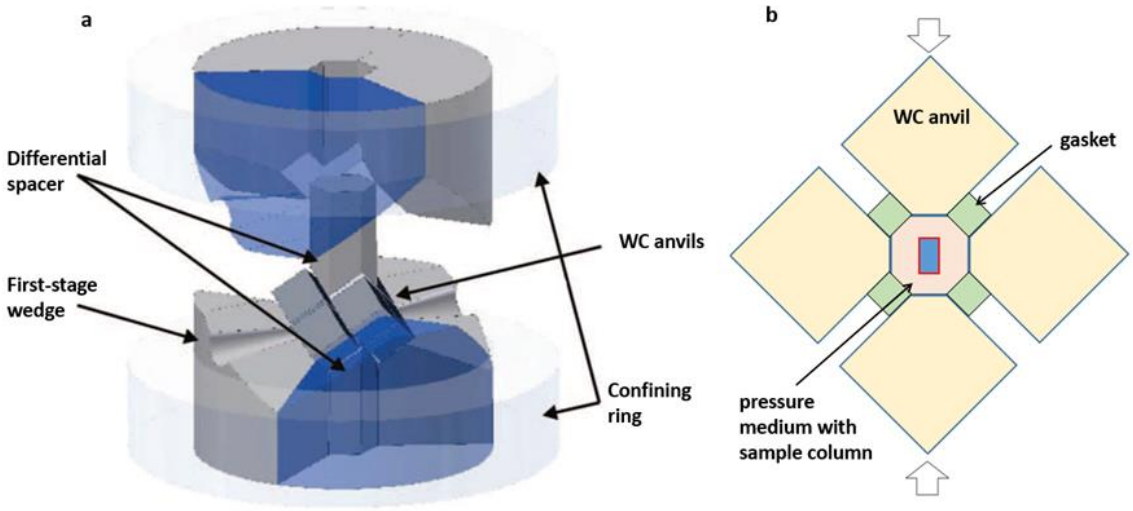

Fig. 4.2. Schematic drawing of DT-Cup tooling (a) and applied MA6-8 type cell assemblies (b). Modified after Hunt et al., (2014).

split-cylinder, geometry, has been developed (Hunt et al., 2014). Different from the traditional Kawai-type apparatus, in which the top and bottom split 6 first-stage steel wedges compressed eight cubic anvils simultaneously. In this newly developed deformation apparatus, two of the eight cubes which sit along the split-cylinder axis can move independently with differential actuators incorporated into the load frame (Fig. 4.2a). Advancement of these differential anvils drives the deformation of sample column which sits along the same direction (Fig. 4.2b). To date the apparatus has succeed to conduct deformation experiment under 18.8 GPa at room temperature and 9.0 GPa up to 1300 K.

In this study, we utilized both D-DIA multi-anvil press and DT-Cup with MA6-8 type cell assembly with intent to study the rheology of lower mantle minerals. In-situ deformation experiment has been done on D-DIA apparatus at BL04b1 at SPring-8. The experiments

using DT-Cup apparatus were conducted at University College London with collaboration with Prof. David Dobson and his group.

4.2. Experimental development for deformation at high pressure

4.2.1 Experiment with D-DIA apparatus

The deformation experiments with D-DIA apparatus were conducted using the multi-anvil apparatus SPEED-Mk.II at the BL04B1 beamline of the synchrotron facility SPring-8, Japan. We adopted the MA6-8 assembly modified for the in situ stress-strain measurements based on the previous work by Tsujino (2012). Pressure was generated by 1.5 mm truncated WC anvils combined with 5.74 mm MgO+5%Cr_2O_3 or crushable Al_2O_3 pressure media (Fig. 4.3a). Ultra-fine grains WC anvils (Fujilloy, TF05) with slit and cone on the upstream and downstream side, respectively, were used for X-ray path. The pressure medium and pyrophyllite gasket on the X-ray path was also replaced by amorphous boron bonded by epoxy (B-epoxy) because of scarce X-ray diffraction from amorphous boron (Fig. 4.3b). High temperature was realized by $LaCrO_3$ heater and monitored by the thermocouple which was located at the end of the sample (Fig. 4.3). Mo foil of 50 μm thickness was used as electrode between heater and WC anvils. Stress was induced by the hard Al_2O_3, sintered-diamond (SD) or sapphire rod along the sample column. Re foil with 10 μm thickness, which is opaque under X-ray, inserted between the samples and pistons was used as a strain marker.

The in-situ stress and strain measurements were conducted by two-dimensional (2D) X-ray diffraction and X-ray radiography at the BL04B1 beamline of SPring-8 (Fig. 4.4). White X-rays from a bending magnet were monochromatized to energies of 51-62keV

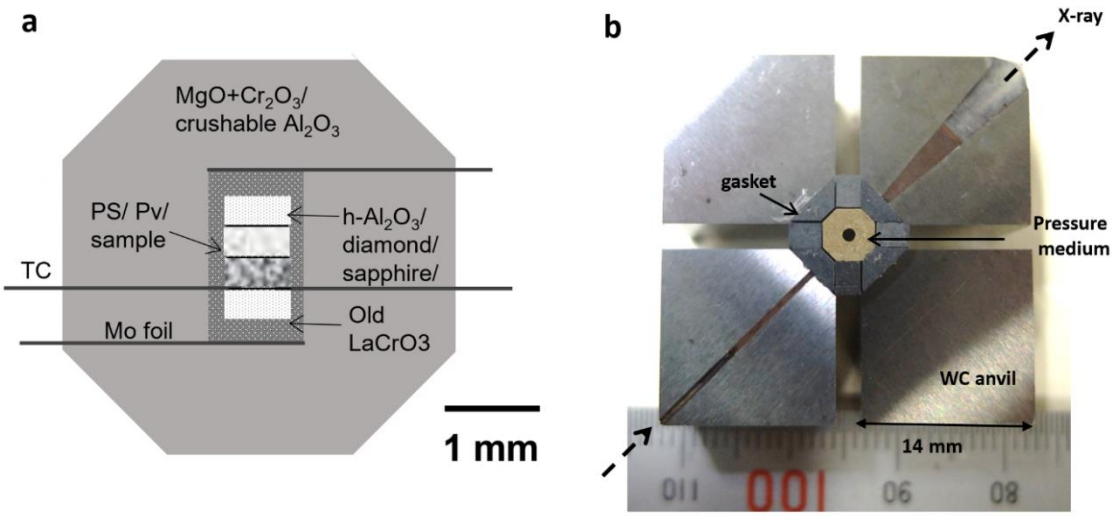

Fig. 4.3. Schematic drawing of assembly for *in-situ* deformation experiments. Design of cell assembly (a) and anvils settings (b).

(wavelengths of 0.2000-0.2431Å) using a Si (111) double-crystal monochromator. The monochromatic X-rays were collimated to 100×100 μm to 200×200 μm by incident slits. Diffracted X-rays were detected with an imaging plate (IP) for 10 min. Optical parameters including camera length, pixel shape of camera, and so on were calibrated using a CeO_2 standard. The IP data were acquired using a FUJI BAS 2000 reader under a resolution of 100 μm×100 μm. The computer software "IPAnalyzer" and "PDIndexer" (Seto et al., 2012) were used for integration of the 2D data to one dimensional profiles with a function of azimuthal angle along the Debye ring pattern and subsequent peak fitting, respectively. X-ray radiographs of the strain markers were taken using an imaging system composed of a YAG crystal and a CCD camera with exposure times of 60 s.

The magnitude of axial deviatoric stress was determined from the 2D X-ray diffraction data based on a model of relationship between axial stress and lattice strain (Singh

et al., 1998),

$$d_{hkl}(\psi) = d^0{}_{hkl}\left[1 + (1 - 3cos^2\psi)\frac{\sigma}{6\langle G_{hkl}\rangle}\right] \qquad (4.1)$$

where d_{hkl} is the d-spacing measured as a function of azimuth angle ψ, $d^0{}_{hkl}$ is the d-spacing under the hydrostatic pressure, G_{hkl} is the appropriate shear modulus and σ is the axial stress for a given hkl. The analyses were made for three diffraction peaks of bridgmanite (111, 112 and 200). The stress magnitude and $d^0{}_{hkl}$ were determined by fitting the observed d_{hkl} to Eq.(4.1) by the least-squares method.

Axial strain of the sample was measured with the in situ X-ray radiographs of the two strain markers placed at both ends of the cylindrical sample. Strain against time was monitored continuously during deformation. The strain rate was obtained by linear fitting of the strain-time plot in the steady state region. For *in-situ* deformation experiment, simultaneously stress and strain measurement at high pressure and high temperature is the most significant advantage, but also bring challenge to the cell design and material. Although deformation with MA6-8 cell has been succeed in the quenched experiment (Tsujino et al., 2016), some improvement is required to apply it to *in-situ* deformation experiment.

The WC anvils are opaque for X-ray, which will limit the radiographic and Debye ring observation within the anvil gap through the gasket region. As the high cost of cBN and sintered-diamond anvils, slotted WC anvils were proposed to be adopted for in-situ high pressure experiments (Dobson et al., 2012). As shown in Fig. 4.3b, the anvils located at the upstream were cut with ~0.3 mm depth and ~0.3 mm width slit and downstream with 5-6°

cone for radiograph and diffraction study. The slit and cone were tapered with ~2° to make shallower cut near the truncation, as the larger anvil gap due to higher pressure. The slot was filled with X-ray transparent material, i.e. near the truncation part with B-epoxy and the other with Araldite epoxy. The B-epoxy is hard after compression which can protect the slotted anvils from collapse under high pressure. The Araldite can stick with the anvil surface well, which is able to prevent the B-epoxy from sliding as the extrusion of pressure medium and gasket during compression.

To obtained more diffraction peaks as a fixed monochromatic energy, the slotted cone with larger angle is desired. Whereas, in our experiments, the blow out possibility is largely

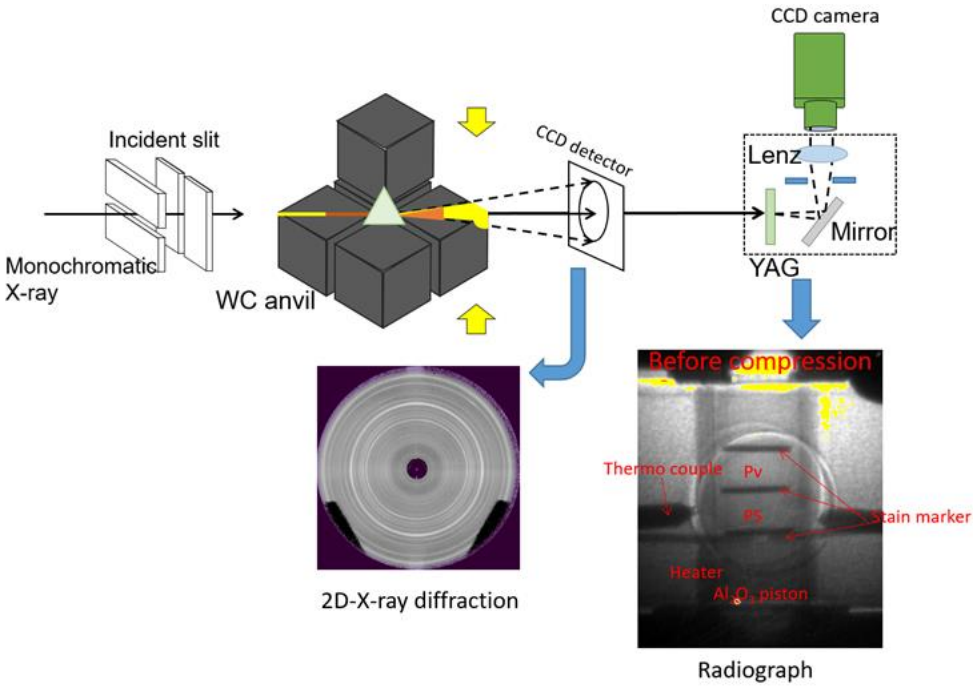

Fig. 4.4. Schematic drawing of *in-situ* stress and strain measurements setup. Example of 2D diffraction pattern and X-ray image are shown.

related to the cone size. The experiments with anvils with cone of 6° blow out almost 100%, while it decreased to ~20% once the cone size was decreased to 5°. We can not exclude effect of other factors, but the size of cone should be carefully considered when cone anvils are utilized under high pressure.

As the weak diffraction from bridgmanite samples, any other diffraction on the X-ray path should be avoided. Thus, we changed the upstream side gasket and pressure medium which are on the X-ray path with 1.1 mm boron-epoxy rod. As the deformation of the B-epoxy rod upon compression, pyrophyllite peaks were always observed. On the X-ray path, to avoid diffraction from gasket, the downstream gasket were replaced with B-epoxy cuboid which is the same thickness with gasket. Although it will cause higher possibility of blow out, the diffraction peaks from pyrophyllite can be eliminated.

As shown in Fig. 4.5a, diffraction of bridgmanite can be obtained without interference of pyrophyllite peaks in situ X-ray diffraction patterns. Although diffraction peaks from LaCrO3 heater still exist, sufficient bridgmanite peaks can be obtained to calculate the stress. The azimuthal dependence of the diffraction peaks of bridgmanite were obtained from 2D X-ray diffraction (Fig. 4.5b). The stress magnitudes were successfully derived at high pressure and high temperature with uniaxial stress ~1.2 GPa. During compressional deformation, anvil gap become smaller, but no resulted strain was observed (Fig. 4.5c). Although we cannot access the definite viscosity of the samples, it indicates high yield strength of the samples.

4.2.2 Experiment with DT-Cup apparatus

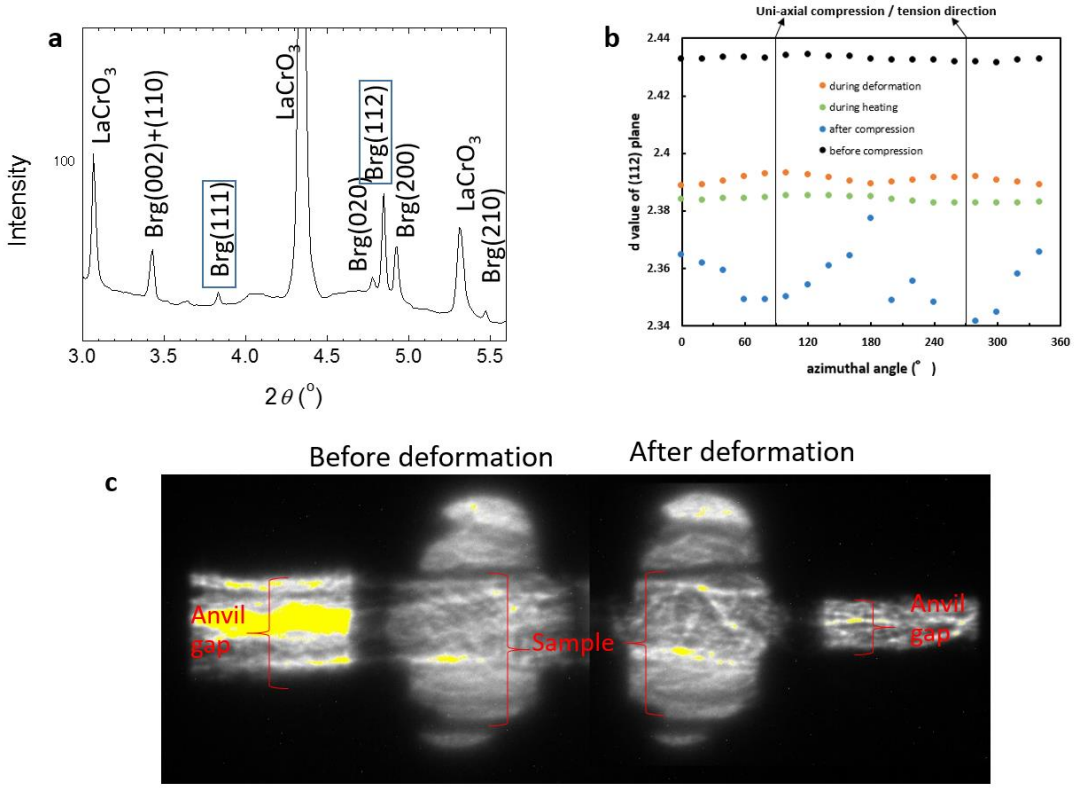

Fig. 4.5. In-situ X-ray diffraction and radiograph. (a) Integrated diffraction pattern from *in-situ* diffraction pattern during deformation. (b) Variation in the d-spacing of bridgmanite (112) with the azimuth angle. (c) The radiograph taken before and after deformation experiment.

The deformation experiments with DT-Cup (Hunt et al., 2014) apparatus were conducted at University College London, UK. We adopted the 6-8 type assembly as used for traditional multi-anvil press. Pressure was generated by 1.5mm truncated WC anvils combined with 5.74 mm MgO+5%Cr_2O_3 pressure media. High temperature was realized by TiB_2 or $LaCrO_3$ heater and monitored by the thermocouple which was located at the center of the cell (Fig. 4.6). To avoid the deformation of sample during cold compression, MgO + 5% Cr_2O_3 and crushable Al_2O_3 piston were set at the two ends of sample column. Hard Al_2O_3

pistons were set near the sample to induce stress during deformation. Two 25 μm thickness Re foil shown in the Fig. 4.6 was inserted in the MgO+5%Cr_2O_3 and crushable Al_2O_3 piston to be the electrode. 10 μm thickness Re was used as the strain marker.

As the limit of maximum load of the press, various optimization have been made to the cell assembly to increase the pressure generation efficiency. The dimension of pressure medium and edge length of truncation of anvils have direct effect on the pressure generation, while decrease the size of cell assembly means decrease of sample size and also causes demerits of worse hydrostaticity condition and homogeneous heating condition. So we started from type (hardness) of WC anvils and design of cell assembly to improve the generated pressure in this study.

The hardness of anvil material is the most essential factor for high-pressure generation, even a small difference in the hardness of WC anvils results in significant

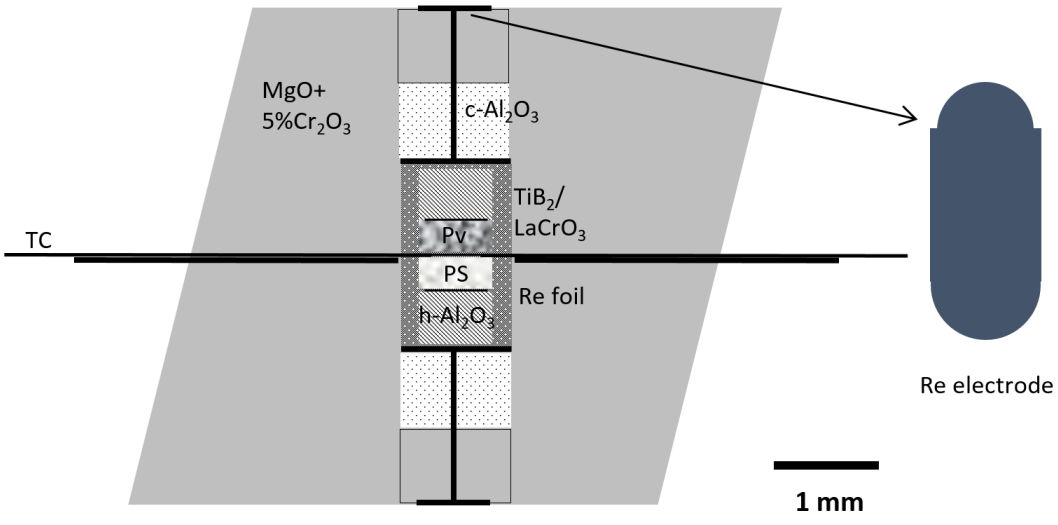

Fig. 4.6. Configuration of cell assemblies for deformation experiment with DT-Cup.

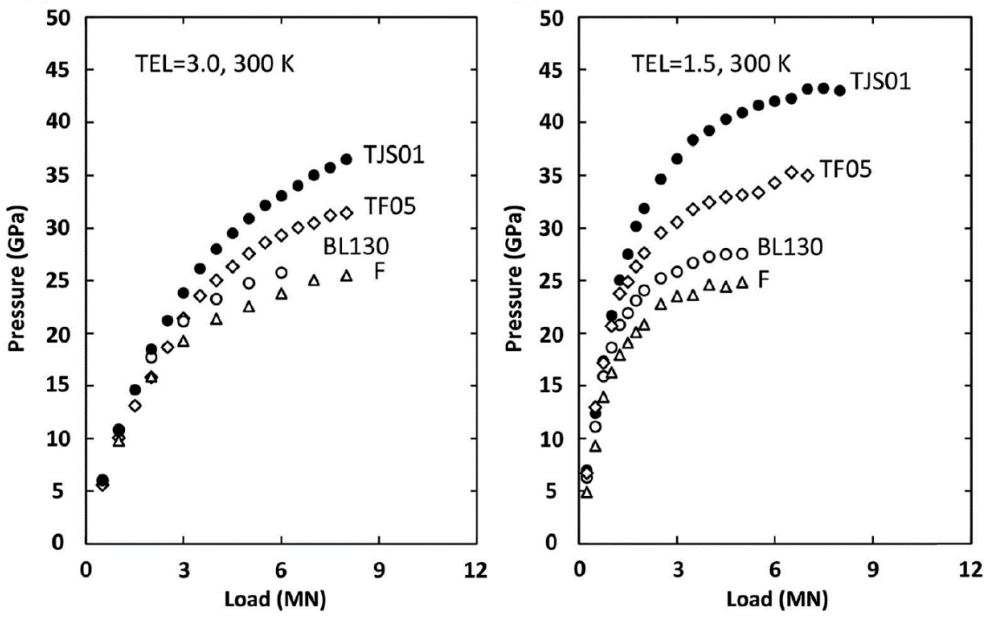

Fig. 4.7. Pressures versus applied press loads in the KMA using various WC second-stage anvils with TEL = 3.0 mm and TEL = 1.5 mm (figure from Kunimoto et al., 2016).

difference in achievable pressures (Irifune et al., 1992). Recently, a new type of ultra-hard WC (Fujilloy TJS01) cubes with extraordinarily high hardness has been developed. This WC composite is made of ultrafine WC powders (~130 nm) with a very small amount of Ni binder (≤0.2 wt%) and small amounts of additives (VC and Cr_3C_2) for suppression of grain growth. Pressure generation with TJS01 has been checked and compared with other commercial anvils as shown in Fig.4.7 (Kunimoto et al., 2016). The higher performance of TJS01 over other types of anvils in pressure generation is more obvious in the experiments using anvils with smaller truncation and higher pressure. So in this study, TJS01 anvils with 16 mm edge length and 1.5 mm truncation were used to generate pressure.

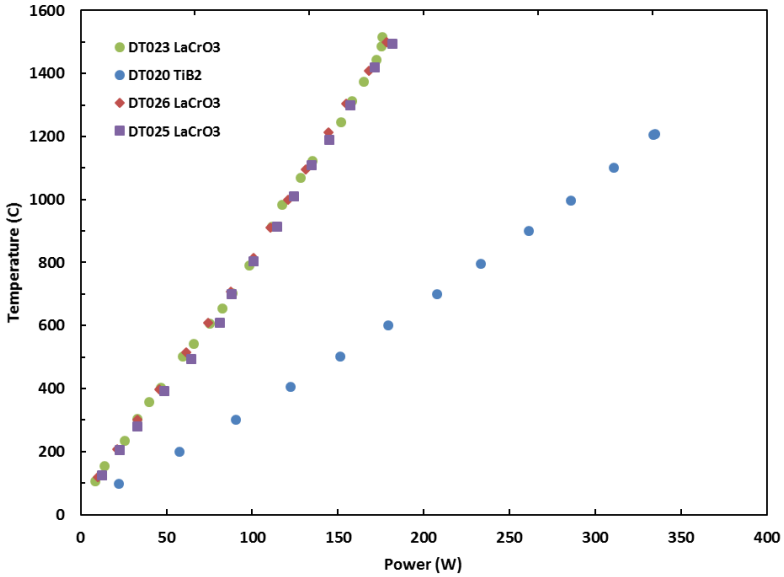

Fig. 4.8. Power-Temperature relationship in experiments with TiB_2 and $LaCrO_3$ as heater. Same cell assembly was used except heater material in these experiments.

The heating efficiency is essential for high-pressure generation with multi-anvil apparatus at high temperatures, because pressure reduction occurs by the enhanced flow of gaskets and pressure medium by heat released from heater at high temperature. In this study, both TiB_2 and $LaCrO_3$ heater were applied to generate high temperature (Fig. 4.8). The comparison of heating efficiency of two kinds of heater indicates the less heat dispersion from the $LaCrO_3$ heater to the pressure medium and gasket. This may enhance the pressure generation efficiency as stated before. As the negative clapeyron slope of the postspinel transition (Katsura et al., 2003), higher pressure decrease the stable pressure of lower mantle mineral assemble.

Fig. 4.9 illustrates pressure and displacement of main ram and differential rams

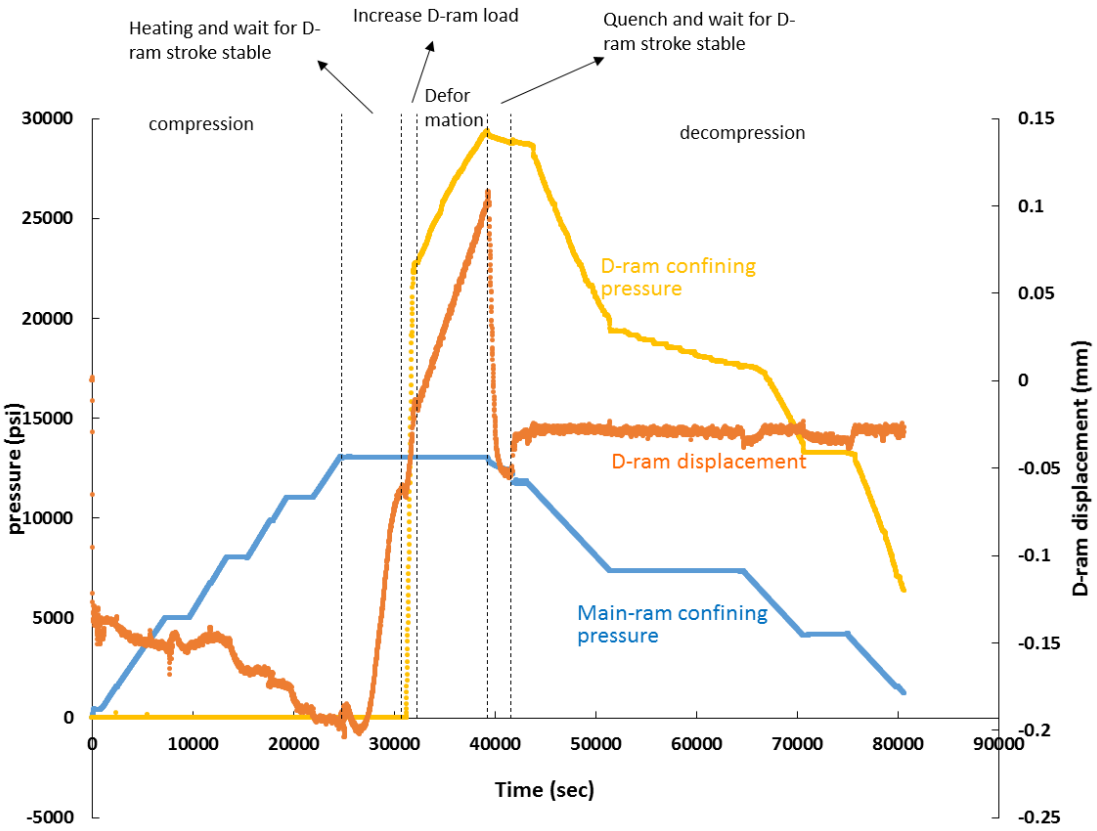

Fig. 4.9. Illustration of pressure and displacement of main ram and differential rams during deformation experiment.

during deformation experiment. The assembly was first compressed to the target load (14000 psi) with the differential rams fully retracted. The drift of differential ram displacement during compression was caused by the back force of differential piston from main rams. After compression, sample was subsequentially heated to target temperature. The apparent differential ram displacement value increased dramatically during heating, due to the thermal effect on the inductance-based displacement transducer, by which voltage was utilized to calculate the displacement. Deformation was not start until the displacement drift is negligible. The differential rams were first advanced rapidly with constant oil pumping rate

until the differential pistons are lifted from their retracted positions, which is marked by the increasing of differential ram displacement. Deformation was conducted with controlling constant displacement rate, with increasing of differential ram load correspondingly. The differential rams were well controlled during deformation. After deformation finished, the sample was quenched and the assembly was decompressed after the displacement getting stable from the temperature effect. During decompression, the positons of differential rams were kept to keep the strain in the deformed sample. Finally, deformation experiment under lower mantle conditions succeed with strain up to ~0.2 after the optimization of the cell assembly.

4.3. Application of deformation experiment to the rheology of post-spinel and bridgmanite

4.3.1 Introduction of rheology of lower mantle

Seismic images indicated that subducting slabs of oceanic lithosphere can stagnate and broaden in the mid-mantle (e.g. Fukao et al., 2013; Li et al., 2008). The mantle viscosity structure inferred from geoid data showed a viscosity jump coincident with depth of slab stagnation (Rudolph et al., 2015). Depth distribution profile of seismic reflectors shows a decrease in the number with depth in the mid-lower mantle with a peak at 800-1200 km. The lack of prominent deeper seismic reflectors than 1600 km may partly reflect decrease in elastic anomalies in the SiO_2 phase and it may also indicates the presence of a viscosity hill in the mid-mantle that blocks the SiO_2-rich components to penetrate deeper. However, the mineralogical mechanism to this increase in viscosity is still a mystery due to the absence of

phase transition in main constituting minerals. A perovskitic lower mantle was reported consist of more than 93 vol.% bridgmanite (Murakami et al., 2012) whereas harzburgite layer in subducting slab contains ~20 vol.% of ferropericlase (Irifune and Ringwood, 1987). Ferropericlase may significantly affect the rheology of the composite of ferropericlase and bridgmanite depend on the microstructure (Handy, 1994), as ferropericlase is likely much weaker than bridgmanite under lower mantle condition (Yamazaki and Karato, 2001). Ferropericlase can remarkably reduce the bulk viscosity when the interconnected weak layer (IWL) of ferropericlase was established. Therefore, the chemical difference layer between the accumulated subducted harzburgite layer in the upper lower mantle and the underlying perovskitic lower mantle may be responsible to the viscosity jump at mid-mantle depth.

Although many studies have been focused on this issue, the role of ferropericlase in the lower mantle rheology is still controversial. Finite element modeling (FEM) of deformation in bridgmanite-ferropericlase aggregates by Madi et al. (2005) found bridgmanite limits deformation even when both phases are highly interconnected. Wang et al. (2013) deformed 72% $CaGeO_3$-perovskite with 28% isolated MgO aggregate in the D-DIA up to 20% axial shortening and found that the bridgmanite analog ($CaGeO_3$) controlled deformation. However, by deformation of mixture of $NaMgF_3$ with various concentration of NaCl (Kaercher et al., 2016), ferropericlase analog was found controls the deformation although the concentration is as little as 15% volume percent. This maybe partially attributed to the microstructure of their starting aggregates, in which ferropericlase analog phase grains were interconnected. Recently, using rotational Drickamer apparatus, Girard et al. (2016) firstly successfully deformed ~70% bridgmanite +~30% ferropericlase aggregates under lower

mantle conditions up to 100% strain. They suggest ferropericlase controlled deformation based on observations of strain weakening during deformation and microstructure of two phases after recovering, even though it was not interconnected. Till to date, the relationship between microstructure (weak phase was interconnected or not) and which phase controls deformation is still controversial, i.e. Madi et al. (2005) shows strong phase controlling deformation when the weak phase is interconnected, while the weak phase controlling deformation when weak phase is not interconnected was also observed (Girard et al., 2016).

In this study, we purpose to clarify the deformation of aggregate of bridgmanite with isolated ferropericlase under lower mantle condition. Here we firstly synthesized well sintered bridgmanite and ferropericlase aggregate with isolated ferropericlase grains inside of a bridgmanite matrix. Uniaxial deformation experiments were done using newly developed DT-Cup apparatus with the Kawai-type cell assembly (MA6-8) (Tsujino et al., 2016; Hunt et al., 2014). To understand the viscosity of bridgmanite and ferropericlase mixture, relative viscosity of two-layered samples composed of post-spinel (PS) (bridgmanite with ~ 30 vol.% of ferropericlase) aggregate and bridgmanite aggregate will be obtained.

4.3.2. Experimental procedures

In this study, two-layered samples of post-spinel and bridgmanite aggregate were stacked along the compression column together for deformation. Strain of each layer is indicated by the change of sample lengths before and after deformation experiments. As the same stress and chemical condition of deformation (e.g. oxygen fugacity, water fugacity), we

can have a direct comparison of the relative strengths of the sample by the strain contrast (e.g. Li et al., 2007). In order to deform the sample at dislocation creep region, post-spinel and bridgmanite aggregate with large grain size are required. Well sintered samples are required to avoid the large deformation during compression.

We pre-synthesized polycrystalline aggregates of post-spinel and bridgmanite as starting materials of deformation experiments at high pressure and high temperature in the Kawai-type multianvil apparatus installed at Institute for Planetary Materials, Okayama University, Japan. Pressure medium of semi-sintered 5 wt. % Cr_2O_3-doped MgO octahedra with 10 mm edge length were compressed by WC cubes with 4 mm truncation edge length. The cross-section of cell assembly is shown in Fig. 4.10. High temperature was generated

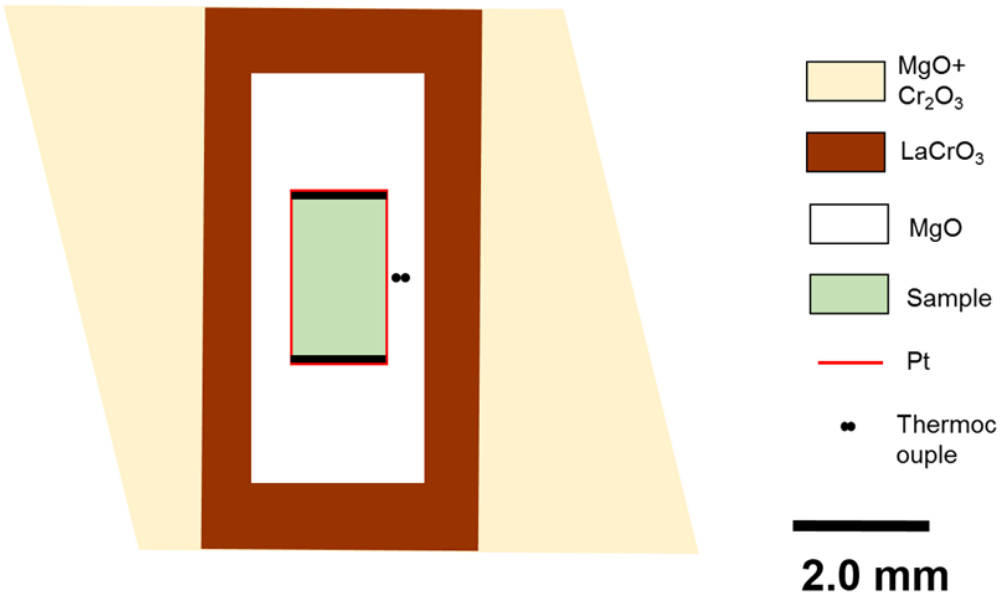

Fig. 4.10. Configuration of cell assemblies for synthesis experiment.

using a $LaCrO_3$ heater and was monitored with a $W_{97\%}Re_{3\%}$-$W_{75\%}Re_{25\%}$ thermocouple whose junction was set next to the samples.

For synthesis of post-spinel, forsterite gel was used as starting material. The starting material was wrapped with platinum capsule and compressed to ~25 GPa and annealed at 1800 °C for three hours. For synthesis of bridgmanite, we use $MgSiO_3$ glass starting material. To suppress the grain size, the sample was compressed with over-pressure (~27 GPa) and fast heat to 1600 °C (from 400 to 1300 °C in 18 secs). The sample was quenched by shut down the power supply after annealing for 5 mins. The sintered samples were core-drilled with a diameter of 0.7 mm by ultrasonic coring machine and sliced with a thickness of 0.3 mm for uni-aixal deformation experiments.

The deformation experiments with DT-Cup (Hunt et al., 2014) apparatus were conducted at University College London, UK. We adopted the MA6–8 assembly as used for traditional multi-anvil press. Pressure was generated by 1.5mm truncated WC anvils combined with 5.74 mm MgO+5%Cr_2O_3 pressure media. High temperature was realized by $LaCrO_3$ heater and monitored by the thermocouple which was located at the center of the cell (Fig. 4.11). To avoid the deformation of sample during cold compression, MgO+5%Cr_2O_3 and crushable Al_2O_3 piston were set at the two ends of sample column. Hard Al_2O_3 pistons were set near the sample to induce stress during deformation. Two 25 μm thickness Re foil was inserted in the MgO+5%Cr_2O_3 and crushable Al_2O_3 piston to be the electrode. 10 μm thickness Re was used as the strain marker.

The sample was first compressed to the target load (~ 2.0 MN) at room temperature

with the differential actuator fully retracted, and temperature was increased to 1500 ℃. In the deformation experiments, temperature was kept at 1500 ℃ for about one hour for annealing. Before deformation, the differential oil pumps are advanced rapidly, usually with a speed of 10 ml/min, until the differential pistons are lifted from their retracted positions, which was indicated by the displacement transducer of the differential rams. The sample was sub-sequentially deformed with advancing upper and lower anvils with a constant oil pump rate (0.25 ml/min for 2 hours in these experiments). After deformation finished, the experiment was quenched and decompressed with keeping the differential rams position. The strain was estimated from the change of sample lengths before and after deformation experiments. We simply calculated the averaged strain rate with total strain and duration of the deformation under the assumption of constant rate of length change during deformation.

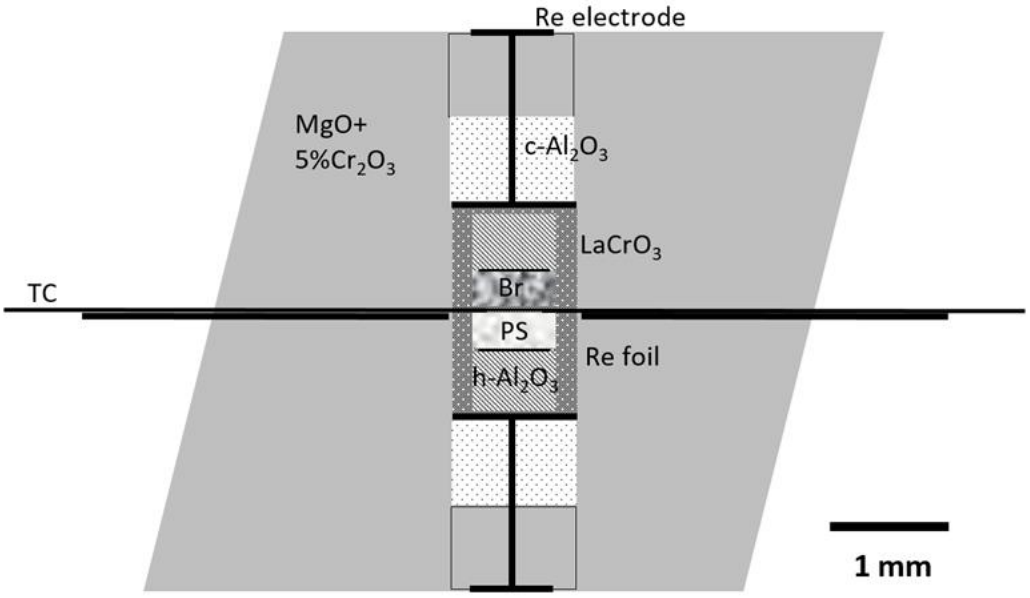

Fig. 4.11. Configuration of cell assemblies for deformation experiment with DT-Cup.

After experiments, the recovered sample were polished parallel to the cylindrical axis after mounted in epoxy resin. It should be pay attention that bridgmanite easily get amorphous at high temperature, epoxy which will be solidify at room temperature should be used. The samples were polished using SiC sand papers and diamond paste. We investigated the microstructure of recovered samples by field emission scanning electron microscopy (FE-SEM, JEOL JSM-700F). As bridgmanite will become amorphous under electron beam, electron backscatter diffraction (EBSD) is not available to obtain the lattice preferred orientation (LPO) pattern. Thus, the LPO of bridgmanite was determined using the two-dimensional (2D) monochromatic X-ray diffraction pattern method. As introduced in Chapter 2, the samples were measured with the uniaxial compressional direction both perpendicular (along ψ=0 and 90° as shown in Fig. 4.12) and parallel to the direction of the X-ray beam. Depend on the sample size, the two-dimensional (2D) diffraction patterns were

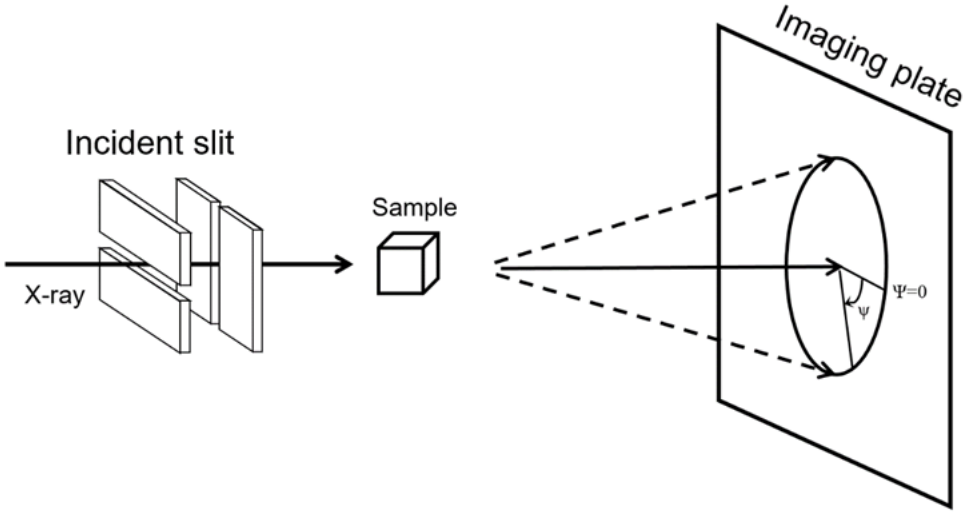

Fig. 4.12. Schematic showing of the two-dimensional X-ray diffraction measurement set-up.

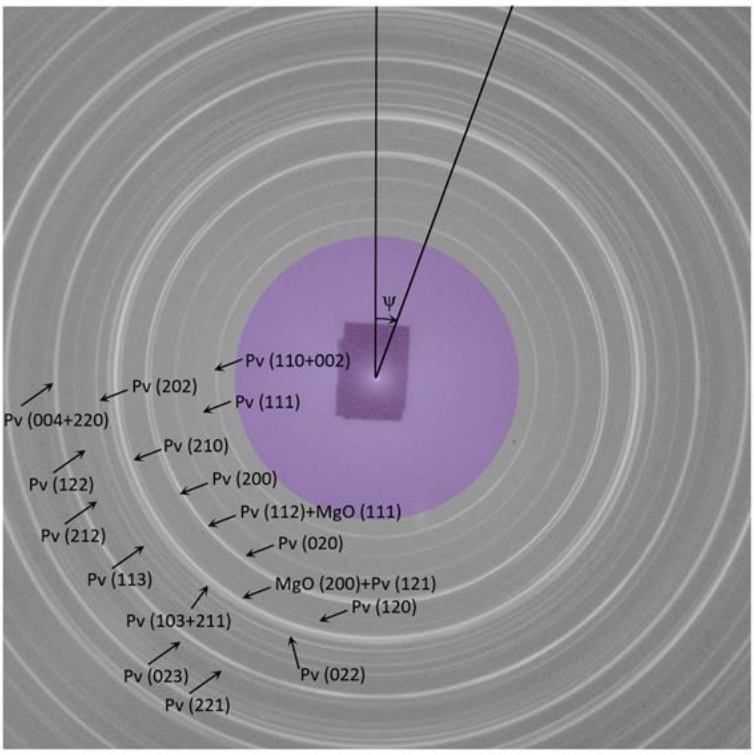

Fig. 4.13. Example of 2D X-ray diffraction pattern of deformed post-spinel sample.

collected with a beam size of 200 μm×100 μm to 400 μm×400 μm for 15 min using an imaging plate (IP). Fig. 4.13 represents the two-dimensional data converted from IP data. The LPO was calculated using the software package of ReciPro (Seto et al., 2012) by simulating the obtained the 2D data (previous study also used, e.g. Tsujino et al., 2016).

4.3.3. Results and discussion on the rheology of lower mantle

The uniaxial deformation experiments with strain of 0.2±0.03 (DT16-037), 0.1±0.04 (DT16-034) were achieved with strain rate of about 2.8 $\times 10^{-5}$ and 1.4 $\times 10^{-5}$, respectively. In both experiments, post-spinel and bridgmanite show similar strain, which indicates the same

viscosity of post-spinel and bridgmanite sample. Fig. 4.14 (a-j) show the microstructure of synthesized and deformed samples. The synthesized post-spinel and bridgmanite aggregates show equigranular texture with almost homogeneous distribution of ferropericlase in the bridgmanite frame in the post-spinel sample. Average grain size for bridgmanite is about 10

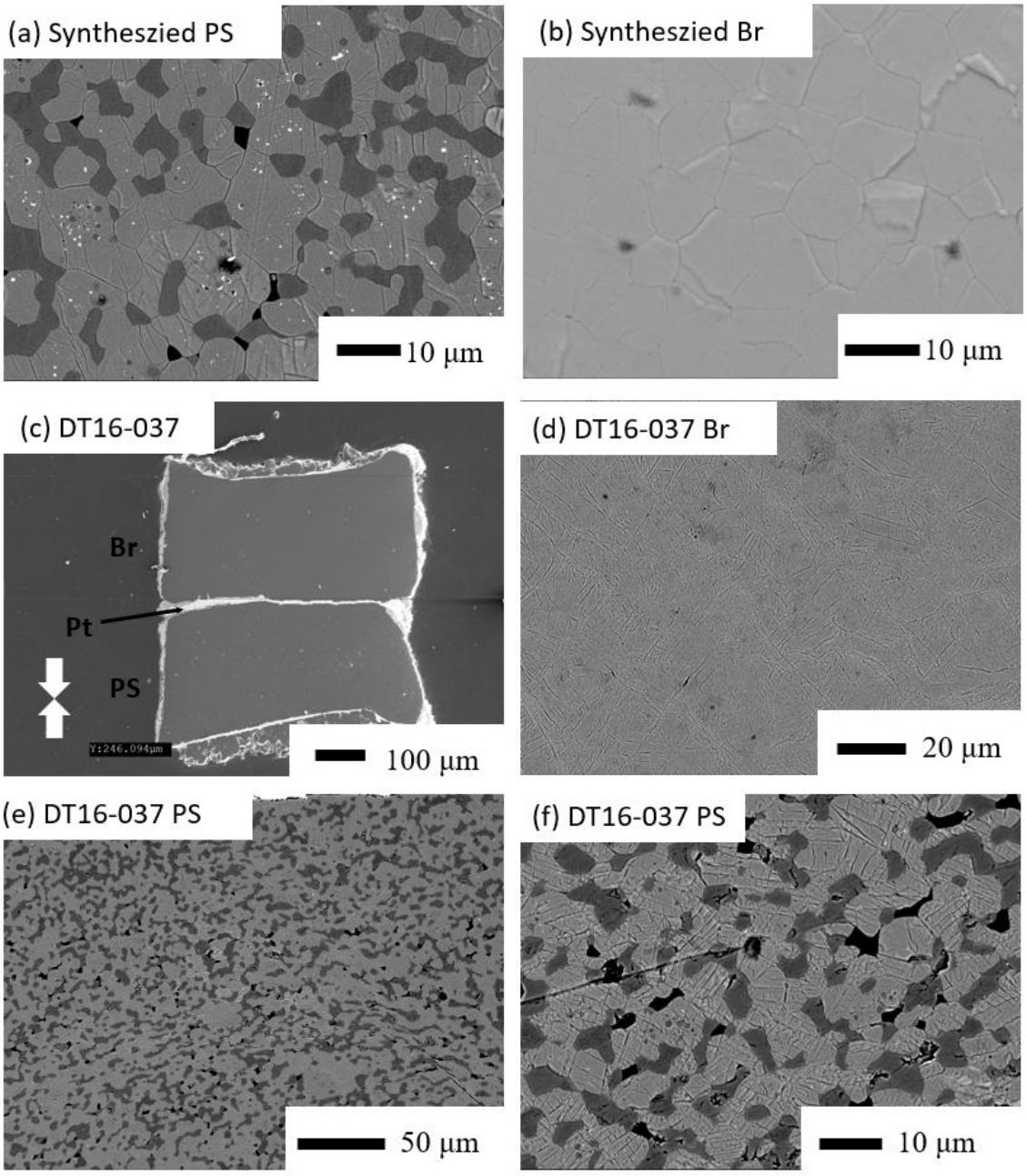

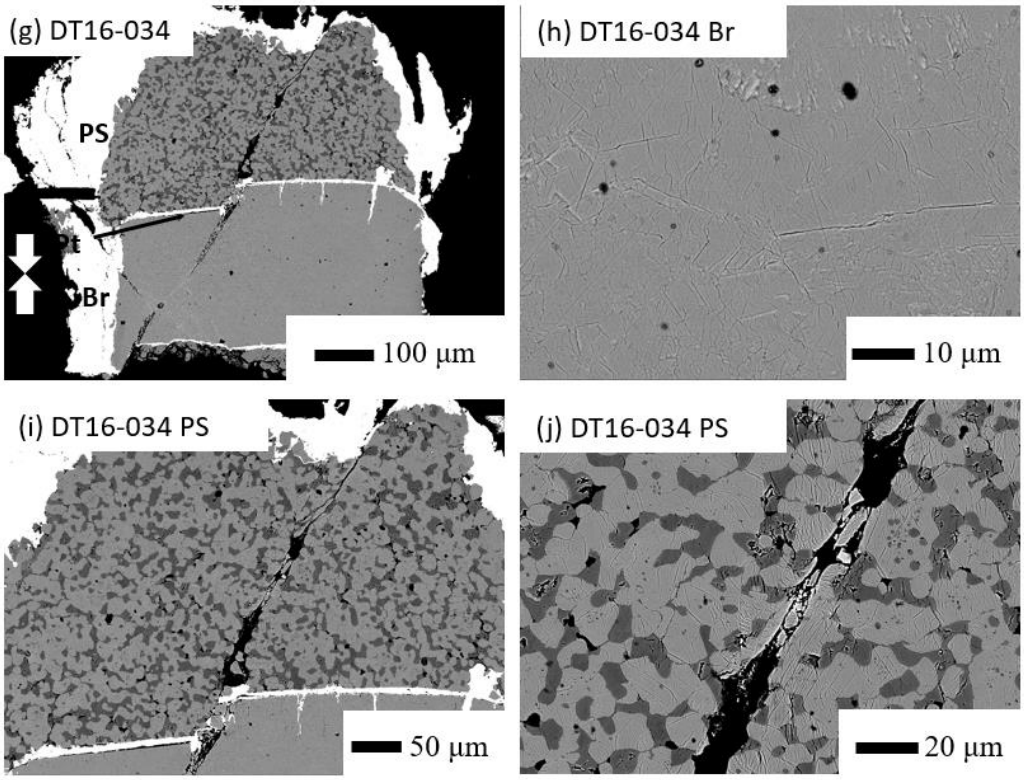

Fig. 4.14. Representative secondary electron images of starting materials (a and b) recovered samples (c-j). The dark grains in (a, e, f, i and j) are grains of periclase in post-spinel composite. The arrows in (c) and (g) represent the direction of uniaxial compression direction.

μm, and that of ferropericlase about 5 μm. After deformation, the bridgmanite grains shows amorphous surface due to the polishing (Fig. 4.14d, h). The recovered samples show cracks which may developed during compression or decompression.

The mircostructure of post-spinel racovered from two deformation experiments show different geometry of ferropericlase. In deformation experiment with strain ~0.2 (DT16-037), ferropericlcase grains show evidence of substatial strain with preferred horizontally elongated shape although obvious interconnection was not observed. On the other hand, post-

spinel deformed to smaller strain (ε~0.1, DT16-034) show homogeneous distribution. This may be due to the smaller strain and/or strain rate in deformation, which shows a converse effect with rouding of grains at high temperature.

The LPOs of starting material and deformed samples were calculated from 2D diffraction patterns (i.e., simulated LPOs) are shown in Fig. 4.15 and 4.16. Fig. 4.15 illustrate pole figures of synthesized bridgmanite and deformed bridgmanite measured with different geometry. The starting material shows little concentration of crystallographic orientation as shown in Fig. 4.15a. With uniaxial compression deformation, (100) plane tends to concentrate on the compressional plane (Fig. 4.15b). It indicated that the dominate slip plane is (100) plane, which is consistent with Tsujino et al. (2016). The pole figures rotate coherently with the rotation of sample direction relative to the beam direction (Fig. 4.15b, c and d). It proves the reliability of the analysis method, and the simulated LPO patterns are not originated from artifact. When the beam line along the uniaxial direction (Fig. 4.15d), the concentration of [100] direction is weaker compared with the orthogonal directions (Fig. 4.15b and c). This maybe result from following two causes: (i) quality loss of the 2D diffraction pattern due to the diffraction of Pt strain marker, thermocouple and remaining Al_2O_3 pistons along the sample column direction, and (ii) difficulty of the evaluation of the LPO developed along the direction of the X-ray incident as the case of the [100] axes.

The pole figures of deformed post-spinel and bridgmanite samples are shown in Fig. 4.16 (a and b for DT16-037), c and d for DT16-034). All the samples shown similar [100]

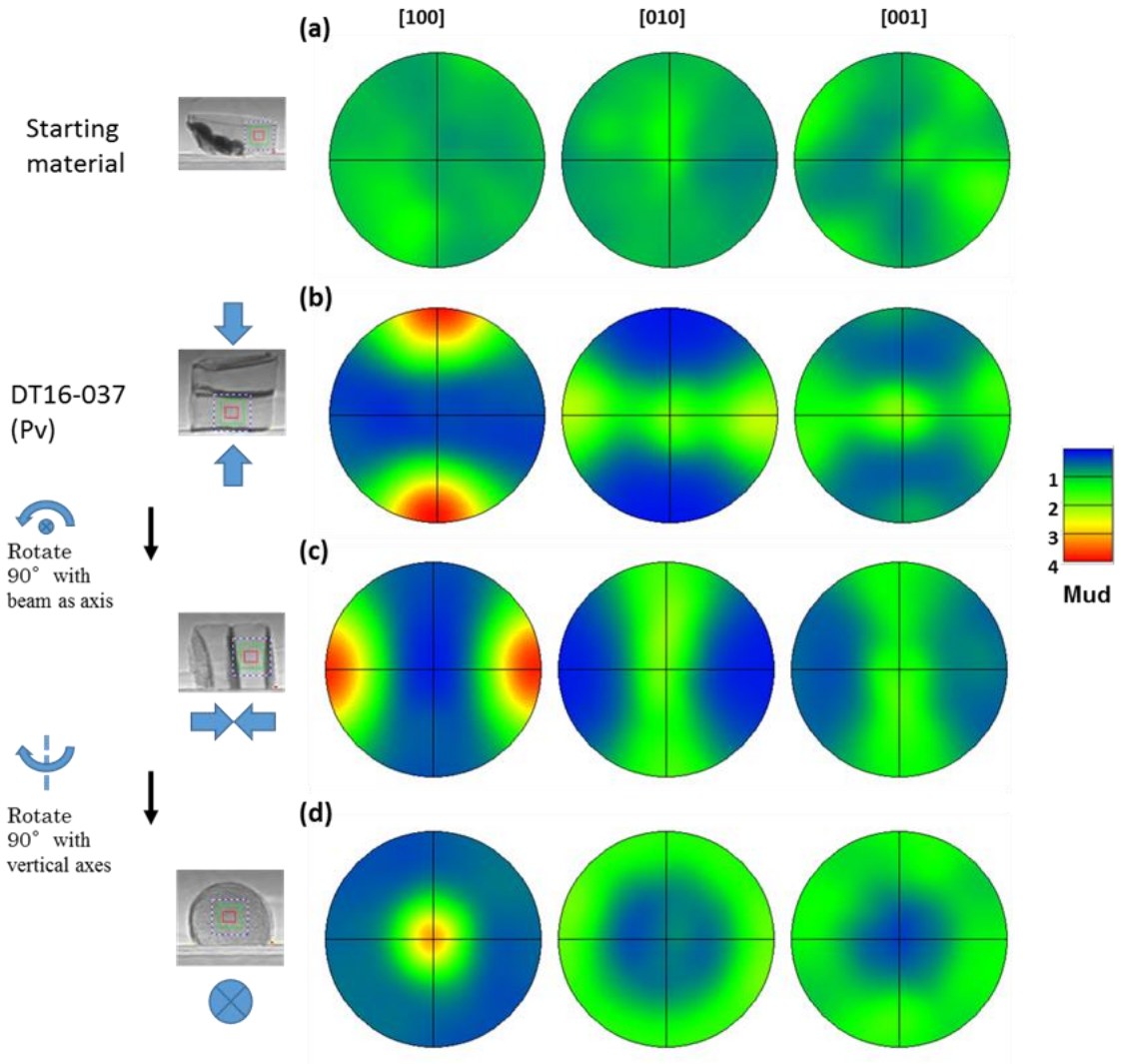

Fig. 4.15. Pole figures showing the simulated LPO of starting material (a) and deformed bridgmanite measured along different directions (b, c and d). The sample image collected with X-ray indicate the direction of sample setting against the uniaxial compression direction. The LPOs were calculated from 2D X-ray diffraction patterns, using the software package "ReciPro" (Seto, 2012; Seto et al., 2010). About 0.5 million grains, which were randomly selected from the LPO data, are plotted in each pole figure. The color coding refers to the density of data points, corresponds to the multiples of uniform distribution as shown in legend. The shear direction is shown by arrows. A half-width of 20° and cluster size of 10° was used for plotting and contouring.

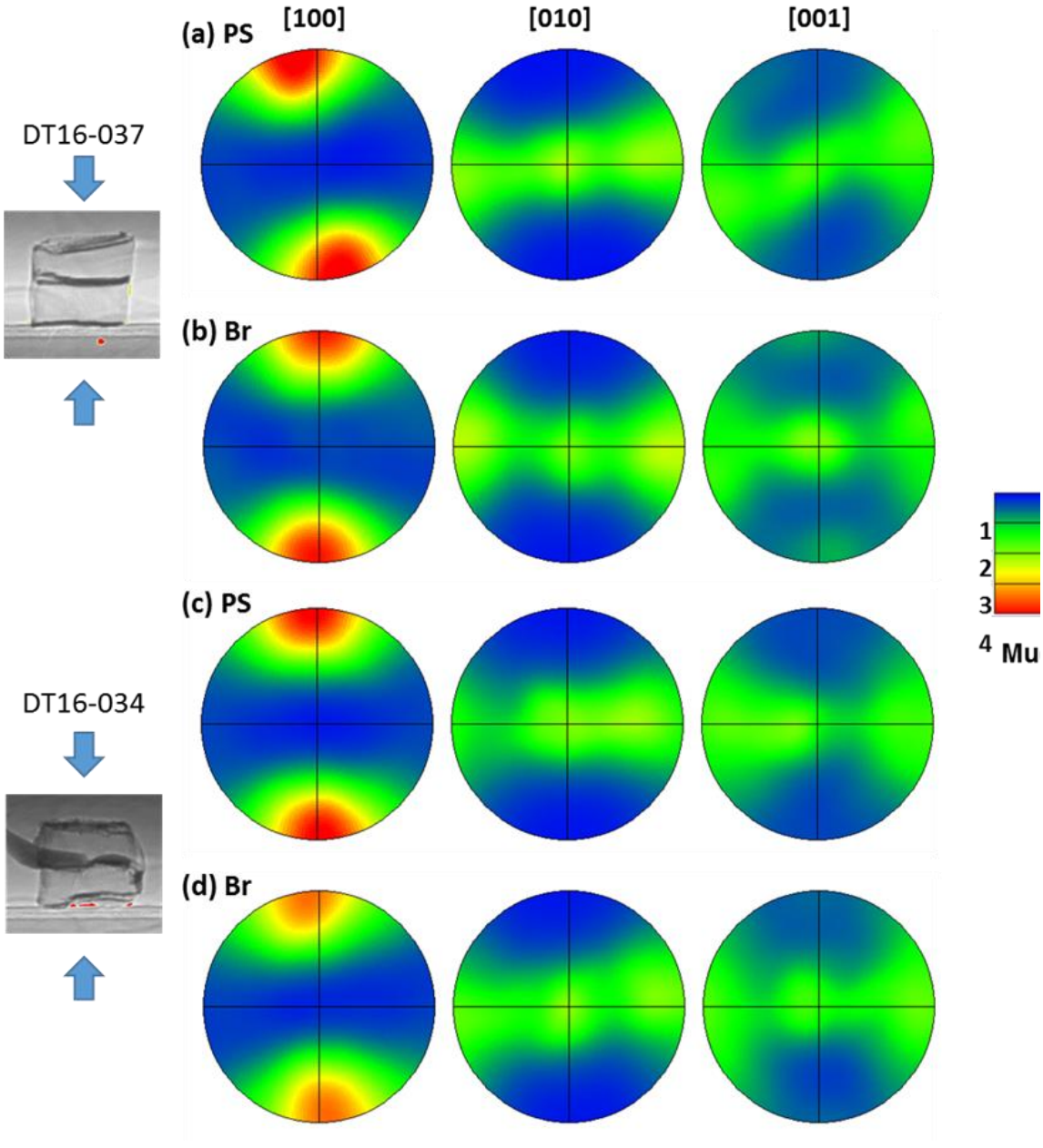

Fig. 4.16. Pole figures showing the simulated LPO of deformed post-spinel and bridgmanite samples. The sample image collected with X-ray indicate the direction of sample setting against the uniaxial compression direction.

direction subparallel to the uniaxial compression direction. Although deformed to different strains, samples from DT16-037 and DT16-034 show comparable concentration of [100] direction, this may indicate the steady state fabric strength was achieved at shear strain $0<\gamma<0.1$ at 1500 ℃ and strain rate of $1.4 \times 10^{-5} < \dot{\gamma} < 2.8 \times 10^{-5}$. To quantitative evaluate the fabric strength, M-index was calculated based on the simulated LPO result (Skemer et al., 2005). M-index gives the difference between the observed distribution of uncorrelated misorientation angles and the distribution of uncorrelated misorientation angles for a random fabric. So the M-index is 0 for random fabric and 1 for a single crystal. Due to the large

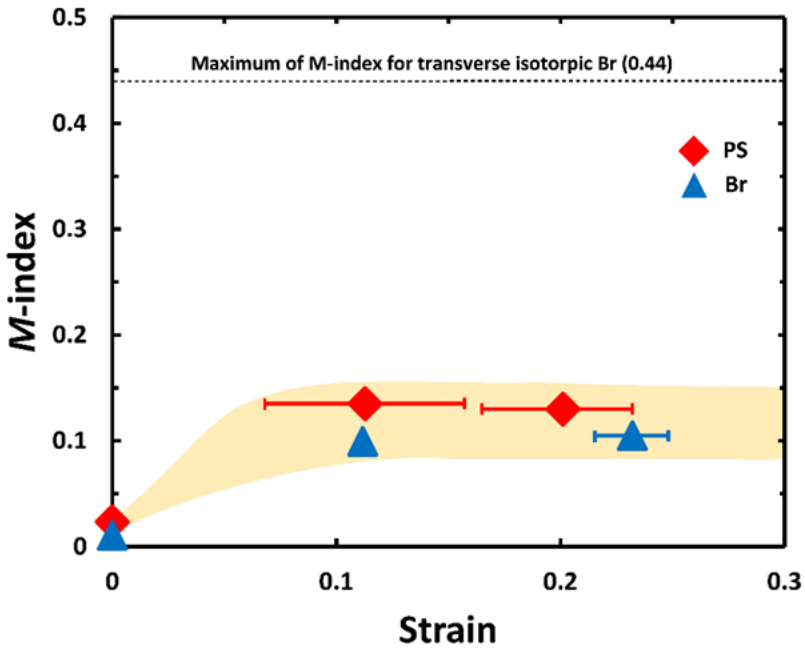

Fig. 4.17. Calculated *M*-index of bridgmanite for starting material and deformed post-spinel and pure bridgmanite samples. Error derived from the determination of sample length from SEM image (Fig. 4.14) after deformation.

number of misorientation angles, *M*-index including few numerical artifact compared with other parameters like *J*-index (Bunge, 1982). Using randomly selected 1.0 million misorientation data, we obtained M-index for starting material and deformed samples and illustrated in Fig. 4.17. The comparable value of *M*-index indicates similar fabric intensity with strain of 0.1 and 0.2, which suggests the steady state fabric was achieved. Although steady state deformation was reported at high strain in olivine (e.g. Ohuchi et al., 2015), deformation of ringwoodite demonstrated steady state deformation at relatively small strain (~ 0.04) at high pressure and high temperature (~ 18 GPa and 1700 K) (Kawazoe et al., 2016).

Rheology of aggregate of bridgmanite with isolated ferropericlase were studied with DT-Cup apparatus under lower mantle condition. Two-layer sample of post-spinel and bridgmanite were deformed simultaneously to identify the effect of ferropericlase to the bulk viscosity. The recovered sample with strain up to 0.2 show similar strain between post-spinel and bridgmanite samples. This indicates the bulk strength is still controlled by the LBF formed by bridgmanite. This indicates harzburgite unable to be responsible for the viscosity jump in the lower mantle, or because the strain is not large enough to induce the interconnectivity of ferropericlase.

The discordance between this study and Girard et al. (2016), who reported a marked softening of post-spinel aggregate with shear strain up to 1.0, highlights the possible importance of shear strain in controlling the geometry of two phases, resulted in different controlling phase of the bulk viscosity. Although uniaxial deformation was applied in deformation experiments reported by Kaercher et al. (2016), their observation of IWL

structure may partially attributed to the interconnected ferropericlase phase layer in their starting aggregate. To identify this, uniaxial deformation with larger strain and shear deformation experiments are planned.

Reference

Bunge, H.J., 1982. Texture analysis in materials science: mathematical methods. Butterworth.

Cordier, P., Ungár, T., Zsoldos, L. and Tichy, G., 2004. Dislocation creep in $MgSiO_3$ perovskite at conditions of the Earth's uppermost lower mantle. Nature, 428, pp. 837-840.

Dobson, D.P., Hunt, S. A., Muller, H.J., 2012. Slotted carbide anvils: improved X-ray access for synchrotron-based multi-anvil experiments, High Pressure Res., 32, pp. 532-536.

Fukao, Y. and Obayashi, M., 2013. Subducted slabs stagnant above, penetrating through, and trapped below the 660 km discontinuity. J. Geophy. Res., 118, pp. 5920-5938.

Girard, J., Amulele, G., Farla, R., Mohiuddin, A. and Karato, S.I., 2016. Shear deformation of bridgmanite and magnesiowüstite aggregates at lower mantle conditions. Science, 351, pp.144-147.

Handy, 1994. Flow laws for rocks containing two non-linear viscous phases: a phenomenological approach. J. Struct. Geol., 16, pp. 287-301.

Hunt, S.A., Weidner, D.J., McCormack, R.J., Whitaker, M.L., Bailey, E., Li, L., Vaughan, M.T., Dobson, D.P., 2014. Deformation T-Cup: A new multi-anvil apparatus for controlled strain-rate deformation experiments at pressures above 18 GPa. Rev. Sci. Inst.,

85, pp. 085-103.

Irifune T, Adachi Y, Fujino K, et al., 1992. A performance test for WC anvils for multianvil apparatus and phase transformation in some aluminous minerals up to 28 GPa. High pressure Res., pp. 43-50.

Irifune, T. and Ringwood, A.E., 1987. Phase transformations in a harzburgite composition to 26 GPa: implications for dynamical behaviour of the subducting slab. Earth Planet. Sci. Lett., 86, pp. 365-376.

Kawazoe T, Ohuchi T, Nishihara Y, Nishiyama N, Fujino K, Irifune T., 2013. Seismic anisotropy in the mantle transition zone induced by shear deformation of wadsleyite. Phys. Earth Planet. Int., 31, pp. 91-98.

Kawazoe, T., Nishihara, Y., Ohuchi, T., Miyajima, N., Maruyama, G., Higo, Y., Funakoshi, K.I. and Irifune, T., 2016. Creep strength of ringwoodite measured at pressure–temperature conditions of the lower part of the mantle transition zone using a deformation–DIA apparatus. Earth Planet. Sci. Lett., 454, pp.10-19.

Kaercher, P., Miyagi, L., and Dawson, K., Kanitpanyacharoen, W., Zepeda-Alarcon, E., Wang, Y., Parkinson, D., Lebensohn, R.A., De Carlo, F., Wenk, H.R., 2016, Two-phase deformation of lower mantle mineral analogs. Earth Planet. Sci. Lett., 456, pp. 134-145.

Kunimoto, T., Irifune, T., Tange, Y., Wada, K., 2016. Pressure generation to 50 GPa in Kawai-type multianvil apparatus using newly developed tungsten carbide anvils. High pressure Res., 36, pp. 97-104.

Li, C., van der Hilst, R.D., Engdahl, E.R. and Burdick, S., 2008. A new global model for P

wave speed variations in Earth's mantle. Geochem. Geophy. Geosyst., 9.

Li, L., Addad, A., Weidner, D., Long, H., Chen, J., 2007. High pressure deformation in two-phase aggregates. Tectonophysics, 439, pp. 107-117.

Mao, H.K., Shu, J., Shen, G., Hemley, R.J., Li, B. and Singh, A.K., 1998. Elasticity and rheology of iron above 220 GPa and the nature of the Earth's inner core. Nature, 396, pp. 741-743.

McNamara, A.K., van Keken, P.E., Karato, S.I., 2002. Development of anisotropic structure in the Earth's lower mantle by solid-state convection. Nature, 415, pp. 310-314.

Merkel, S., Wenk, H.R., Badro, J., Montagnac, G., Gillet, P., Mao, H.K. and Hemley, R.J., 2003. Deformation of ($Mg_{0.9}$, $Fe_{0.1}$) SiO_3 perovskite aggregates up to 32 GPa. Earth Planet. Sci. Lett., 209, pp. 351-360.

Murakami, M., Ohishi, Y., Hirao, N. and Hirose, K., 2012. A perovskitic lower mantle inferred from high-pressure, high-temperature sound velocity data. Nature, 485, pp. 90-94.

Nishiyama, N., Wang, Y., Sanehira, T., Irifune, T., Rivers, M.L., 2008. Development of the multi-anvil assembly 6-6 for DIA and D-DIA type high-pressure apparatuses. High Pressure Res., 28, pp. 307-314.

Ohuchi, T., Nishihara, Y., Seto, Y., Kawazoe, T., Nishi, M., Maruyama, G., Hashimoto, M., Higo, Y., Funakoshi, K.I., Suzuki, A., Kikegawa, T., 2015. In situ observation of crystallographic preferred orientation of deforming olivine at high pressure and high temperature. Phys. Earth Planet. Int., 243, pp. 1-21.

Rudolph, M.L., Lekić, V. and Lithgow-Bertelloni, C., 2015. Viscosity jump in Earth's mid-

mantle. Science, 350, pp. 1349-1352.

Seto, Y., 2012. Whole pattern fitting for two-dimensional diffraction patterns from polycrystalline materials. Rev. High Press. Sci. Technol. 22, pp. 144-152.

Singh, A.K., Balasingh, C., Mao, H.K., Hemley, R.J. and Shu, J., 1998. Analysis of lattice strains measured under nonhydrostatic pressure. J. Applied Phy., 83, pp. 7567-7575.

Tsujino, N., 2012. Experimental Study on Rheology of the Earth's Lower Mantle. PhD thesis, Tokyo Institute of Technology.

Tsujino, N., Nishihara, Y., Yamazaki, D., Seto, Y., Higo, Y., Takahashi, E., 2016. Mantle dynamics inferred from the crystallographic preferred orientation of bridgmanite. Nature, 539, pp.81-84.

Wang, Y., Durham, W.B., Getting, I.C. and Weidner, D.J., 2003. The deformation-DIA: A new apparatus for high temperature triaxial deformation to pressures up to 15 GPa. Rev. Sci. Instr., 74, pp. 3002-3011.

Yamazaki, D. and Karato, S.I., 2001a. High-pressure rotational deformation apparatus to 15 GPa. Rev. Sci. Instru., 72, pp. 4207-4211.

Yamazaki, D., Karato, S.I., 2001b. Some mineral physics constraints on the rheology and geothermal structure of Earth’s lower mantle. Am. Mineral. 86, pp. 385-391.

Acknowledgements

First of all, I sincerely thank D. Yamazaki for supervising during my Ph.D. course. I highly appreciate N. Tsujino for helpful comments and guidance for research. I am also grateful to E. Ito, A. Yoneda and T. Yoshino for their support and valuable comments during my study. I would like to express my thanks to W. Sun, H. Fei, A. Shimojuku, S. Shan, B. Zhang, X. Guo for their tutoring of experiments and apparatus.

Then, I want to express my thanks to E. Takahashi for conducting deformation experiments with KATD apparatus at Tokyo Institute of Technology in Chapter 2. I want to thank N. Sakamoto and N. Yurimoto at Hokkaido University for helping doing SIMS measurement and S. Yamashita for FTIR measurement in Chapter 3. Thank Y. Higo and Y. Tange for helping me conducting deformation experiments and using monochromatic 2D diffracting device at SPring-8 BL04B1 in Chapter 2 and 4. I also thank Y. Nishihara for using of D-DIA installed at SPring-8 BL04B1. Thank K. Ohara for making $MgSiO_3$ glass at SPring-8 BL04B2 and T. Hiraga for providing forsterite aggregate in Chapter 4. Thank S. Hunt and D. Dobson for conducting deformation experiment with DT-Cup at University College London (UCL), UK.

I acknowledge the support of Budding Researchers Program of SPring-8. Some of the experiments in Chapter 4 were conducted at SPring-8 BL04B1 (Proposal Nos., 2014B1778, 2015B1761 and 2016A1629). I am supported by MEXT Kakenhi “Core-Mantle Coevolution” to conduct deformation experiments at UCL, UK.